Three-dimensional Mathematical Model of a High Temperature Polymer Electrolyte Membrane Fuel Cell

Thesis Submitted To

University of Cape Town

in fulfilment of the requirements for the degree

Doctor of Philosophy

by

Victor George Hess

Department of Mathematics and Applied Mathematics
University of Cape Town
2016

To

Gabriel and Alexander

May this be an inspiration to you, and to

Lucy and Monique

Thanks for enduring my absent days.

Acknowledgements

This thesis work forms part of a broader polymer electrolyte fuel cells and stacks research project developed by Hydrogen South Africa (HySA). This initiative started under the directorship of Professor Øysten Ulleberg. Other participating spokes of this project include, in the Western Cape, the Chemical Engineering Department of the University of Cape Town whose research focuses on the development of suitable catalysts and membranes and the Mechanical Engineering Department of the University of Stellenbosch whose research focus is the development of solid materials for bipolar plates and other stack interconnects.

A prime purpose of this mathematical model is to assist the research initiative in the areas of design and optimisation.
I would like therefore to express my gratitude to:

- **Professor Øysten Ulleberg**, who was the Director of Hydrogen South Africa, at the time, for his unwavering commitment to the project, his support in organizing workshop, his assistance in our feedback sessions

- **Hydrogen South Africa**, for your financial support that made this work possible.

- **Dr. Henri Laurie**, my supervisor for his guidance and encouragement, especially during the latter part of the thesis work.

Abstract

Polymer electrolyte fuel cells are regarded as one of the most promising alternatives to the depleting and high pollutant fossil fuel energy sources. High temperature Polymer electrolyte fuel cells are especially suitable for stationary power applications. However, the length scale of a PEM fuel cells main components range from the micro over the meso to the macro level, and the time scales of various transport processes range from milliseconds up to a few hours. This combination of various spatial and temporal scales makes it extremely challenging to conduct in-situ measurements or other observations through experimental means. Thus, numerical simulation becomes a very important tool to help understand the underlying electrochemical dynamics and transient transport phenomena within PEM fuel cells.

In this thesis research a comprehensive, three- dimensional mathematical model is developed which accounts for the convective and diffusive gas flow in the gas channel, multi-component diffusion in the porous backing layer, electrochemical reactions in the catalyst layers, as well as flow of charge and heat through the solid media.

The governing equations which mathematically describe these transport processes, are discretized and solved using the finite-volume based software, Ansys FLUENT, with its in-built CFD-solvers. To handle the significant non-linearity stemming from these transport phenomena, a set of numerical under-relaxation schemes are developed using the programming language C++. Good convergence is achieved with these schemes, though the model is based on a serpentine single-channel flow approach.

The model results are validated against experimental results and good agreement is achieved. The result shows that the activation overpotential is the greatest cause of voltage loss in a high temperature PEM fuel cell. The degree of oxygen depletion in the catalyst layer, under the ribs, is identified and quantified for a given set of input parameters. This factor is followed by membrane resistance to protonic migration. The model can thus be suitable applied as a tool to predict cell performance. The results also show that performance is influenced by not just one, but a combination of inter-related factors, thus temperature increases, and flow rate changes will only be effective if simultaneously, the concentration of inlet oxygen, and the mobility of proton-ions in the membrane is increased. Not only does the model results verify these phenomena, but provide a quantitative output for any given set of input parameters. It can therefore be suitably applied as an optimisation tool in high temperature PEM fuel cell design.

Contents

List of Tables

List of Figures

List Of Symbols

Table 1

Symbol	Unit	Description
a	m^2 /m^3	water activity; density of active area in the catalyst layer
A	m^2	area
A_v	m^2 /m^3	reaction surface area density
K_0	m^2	Porous-medium permeability-coefficient
c	kmol m^{-3}	Molar density of the mixture
c_i	kmol m^{-3}	Molar density of species i
c_p	$m^2.s^{-2}.K^{-1}$	Specific heat at constant pressure of the fluid
c_{pi}	$m^2.s^{-2}.K^{-1}$	Specific heat at constant pressure of species i
d	m	Distance between the centroids of two neighbour cells
$\mathcal{D}_{ij}$	$m^2.s^{-1}$	Ordinary diffusion coefficient of species i in species j
$\mathcal{D}_{im}$	$m^2.s^{-1}$	Ordinary diffusion coefficient of species i in a multicomponent mixture
E_{act}	kg $m^2.s^{-2}$.kmol^{-1}	Activation energy
E	V	Electric potential difference
E_0	V	Standard electric-potential difference
F	A.s.kmol^{-1}	Faradays constant
h	$m^2.s^{-2}$	Sensible enthalpy of the fluid
h	$m^2.s^{-2}$	Sensible enthalpy of species i
H_r	kg.$m^2.s^{-3}$	Enthalpy of reaction
i	A.m^2	Current density magnitude
$\vec{i}$	A.m^{-2}	Current density
$\vec{i}$	A.m^{-2}	Exchange current exchange density
I	A	Current
$\vec{j_i}$	kg.$m^2.s^{-1}$	Mass diffusion-flux of species i relative to the mass-average velocity
$\vec{J_i}$	kmol.$m^{-2}.s^{-1}$	Molar diffusion flux of species i
l_e	m	Electrolyte thickness normal to the electrode-electrolyte interface
m	m	Current iteration
n		Number of species in the gas mixture
n		Number of electrons required to convert a single i-species molecule

Continued on next page

Table 1

Symbol	Unit	Description
p	$\mathrm{kg.m^{-1}.s^{-2}}$	Pressure
p_i	$\mathrm{kg.m^{-1}.s^{-2}}$	Partial pressure of species i
P	$\mathrm{kg.m^{2}.s^{-3}}$	Power
q	$\mathrm{kg.s^{-3}}$	Energy flux
Q	$\mathrm{kg.m^{-1}.s^{-3}}$	Volumetric heat sources/sinks, Joule heat
r	m	Vector from the i th to the j th surface elements
R	$\mathrm{kg.m^{2}.s^{-2}.kmol^{-1}.K^{-1}}$	Ideal gas constant
R	Equation units	Equation residual
s	Equation units	Equation-system source
S_c	$\mathrm{m^2}$	Surface bounding the control volume
S_f	$\mathrm{m^2}$	Face surface
S_m	$\mathrm{kg.m^{3}.s^{-1}}$	Global mass source or sink
S_{mi}	$\mathrm{kg.m^{3}.s^{-1}}$	Mass source or sink of species i
$S_{o,\lambda i}$	K	Sutherland-law parameter for species i
$S_{o,\mu i}$	K	Sutherland-law parameter for species i
t	s	Time
T	K	Temperature
$T_{o,\lambda i}$	K	Sutherland-law parameter for species i
$T_{o,\mu i}$	K	Sutherland-law parameter for species i
$\vec{u}$	$\mathrm{m.s^{-1}}$	Fluid mass-averaged velocity
$\vec{u}_f$	$\mathrm{m.s^{-1}}$	Mean velocity of the fluid through the void space of a porous medium
$\langle\vec{u}\rangle$	$\mathrm{m.s^{-1}}$	Superficial permeation velocity
V	V	Voltage
V_c	$\mathrm{m^3}$	Control volume
V_r	$\mathrm{m^3}$	Volume
w		Linear-interpolation weight factor
w_{ref}	$\mathrm{kg.m^{2}.s^{-2}.kmol^{-1}}$	Specific reversible work
W	$\mathrm{kg.kmol^{-1}}$	Molecular weight of the fluid
W_i	$\mathrm{kg.kmol^{-1}}$	Molecular weight of species i
x	m	Spatial coordinate
$vecx$		Unit base vector
x_i		Molar fraction of species i
$\vec{y}$		Unit base vector
y_i		Mass fraction of species i
$\vec{z}$		Unit base vector
Greek letters		
α_b		Backward transfer coeficient
α_f		Forward transfer coeficient
γ	$\mathrm{A.m^{-2}}$	Pre-exponential coefficient
Γ_i	$\mathrm{m^2.s^{-1}}$	Dusty-gas model parameter
ΔG_r	$\mathrm{kg.m^{2}.s^{-2}.kmol^{-1}}$	Specific Gibbs free energy of reaction
ΔG_r^0	$\mathrm{kg.m^{2}.s^{-2}.kmol^{-1}}$	Specific standard Gibbs free energy of reaction
ΔH_r	$\mathrm{kg.m^{2}.s^{-2}.kmol^{-1}}$	Specific enthalpy of reaction

Continued on next page

Table 1

Symbol	Unit	Description
ΔS_r	$\mathrm{kg.m^2.s^{-2}.kmol^{-1}}$	Specific entropy of reaction
ϵ	variable units	Iteration error
ε		Porosity of the porous medium
ε_i	$\mathrm{kg.m^2.s^{-2}}$	Characteristic energy of species i
η_{act}	V	Activation overpotential
η_{conc}	V	Concentration overpotential
η_{ohm}	V	Ohmic overpotential
λ	$\mathrm{kg.m.s^{-3}.K^{-1}}$	Thermal conductivity of the fluid
λ_i	$\mathrm{kg.m.s^{-3}.K^{-1}}$	Thermal conductivity of species i
λ_{0i}	$\mathrm{kg.m.s^{-3}.K^{-1}}$	Sutherland-law parameter for species i
μ	$\mathrm{kg.m^{-1}.s^{-1}}$	Fluid viscosity
μ_i	$\mathrm{kg.m^{-1}.s^{-1}}$	Viscosity of species i
μ_{0i}	$\mathrm{kg.m^{-1}.s^{-1}}$	Sutherland-law parameter for species i
ρ	$\mathrm{kg.m^{-3}}$	Mass density of the fluid
$\tilde{\rho}$	$\mathrm{C.m^{-3}}$	Charge density
$\tilde{\sigma}$	$\mathrm{A.V^{-1}.m^{-1}}$	Ionic conductivity
σ_{sb}	$\mathrm{kg.s^{-3}.K^{-4}}$	Stefan-Boltzmann constant
τ		Tortuosity factor of the porous medium
$\vec{\tau}$	$\mathrm{kg.m^{-1}.s^{-2}}$	Stress tensor
ϕ	V	Electric potential
ϕ_a	V	Electric potential of the electric-conducting phase of the anode
ϕ_c	V	Electric potential of the electric-conducting phase of the cathode
ϕ_e	V	Electric potential of the ion-conducting phase of the electrolyte
ϕ_v	$\mathrm{kg.m^{-1}.s^{-3}}$	Viscous dissipation
ϕ_{ij}		Semi-empirical correlation parameter
φ		Generic dependent variable
ω	$\mathrm{kg.m^{-1}.s^{-3}}$	Heat of reaction
Ω		Collision integral
Subscripts		
a		Anode
b		Bulk, feeding mixture concentration
c		Cathode
ce		Channel-electrode interface
e		Electrolyte
ec		Electrode-channel interface
eq		Equilibrium
f		Fluid
fc		Face center
$fuel$		Fuel
ia		Interconnect-anode interface
ic		Interconnect-cathode interface

Continued on next page

Table 1

Symbol	Unit	Description
in		Channel inlet
$\mathcal{N}$		Cell index
oc		Open circuit
out		Channel outlet
$\mathcal{P}$		Cell index
r		electrode-electrolyte interface
ra		anode-electrolyte interface
rc		cathode-electrolyte interface
ref		Reference value
rev		Reversible
s		Solid
Superscripts		
eff		Effective value in the porous media
n		Iteration number

Chapter 1

Introduction

1.1 Background

The development of fuel cell technology is one of a number of new energy generation technologies, such as wind power, solar power and ocean-wave power that are being utilized and developed in an attempt to move away from the existing use of fossil fuels as energy-generating sources. The rapid decline in fossil fuel reserves is but one factor in the expansion of alternative-energy technologies. Two other major factors are critical drivers for this process. The first factor is the vast growth in global populations, especially in the so-called Third World countries of Asia and Africa. It is projected that the world population will grow from an estimated 6.6 billion people in 2007 to 8.2 billion in 2030, or on average one percent increase per year. The fastest rate of growth will be in Africa, projected at around two percent per annum, followed by the Middle East at 1.6 percent per annum. China will grow slower at around 0.4 percent, but will remain the world's most populous country at around 1.46 billion people in 2030 [2].

The vast growth in populations in these regions impact hugely on development and economic growth, and thus on the demand for energy both in size and pattern.

A characterization of this development is the rise in industrialization and living standards spearheaded by the so-called BRIC countries (Brazil, Russia, India and China), and followed strongly by Africa, whose vast reserves of the world's natural mineral resources are leading its path to industrialisation. An increasing demand on the world's energy resources is consequently placed to service this economic growth. Primary energy demand is projected to increase by 1.5 percent per annum from 2007 to 2030, which is an overall increase of 40 percent [1]. This demand for energy is currently predominantly met by the utilisation of fossil fuels with oil as our prime source of energy, followed by coal. One of the problems with the existing fossil fuel technology is that it is based on combustion technology which makes the resources non-renewable. A second problem is the skew distribution between producers and the consumers of fossil fuels. In figures 1.1 and 1.2, we show the distribution of estimated (as of January 2011) reserves, production and consumption of oil and natural gas around the world.

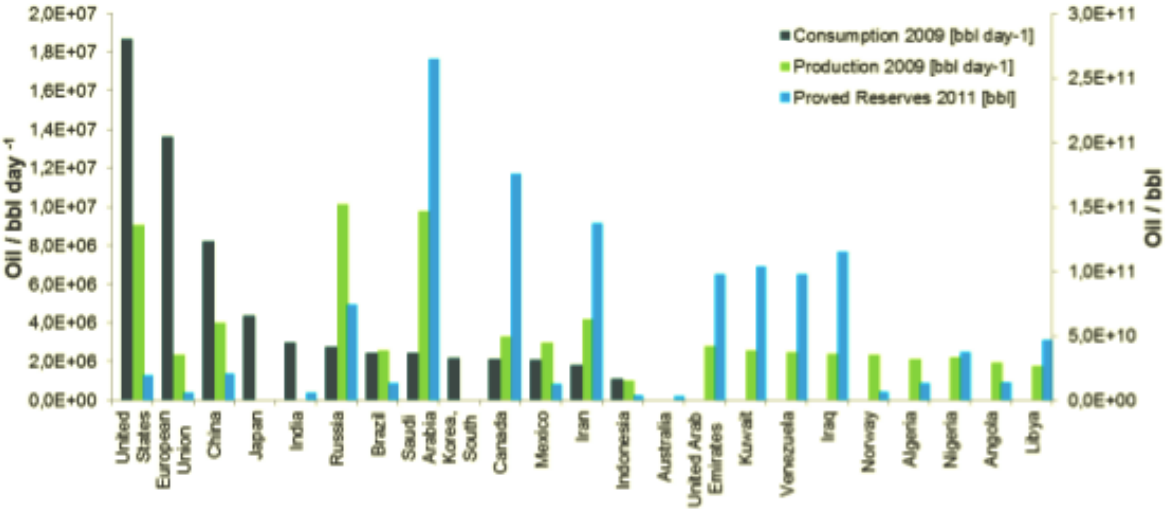

Figure 1.1: Distribution of World Oil consumption, production and reserves [3]

The figures show that oil reserves are mostly located in the Middle East, Russia and Canada, and natural gas are mostly located in Russia and Iran. However, the major consumers are the United States and European Union, with fast developing countries such as China, India and Brazil showing growing yearly consumption in-

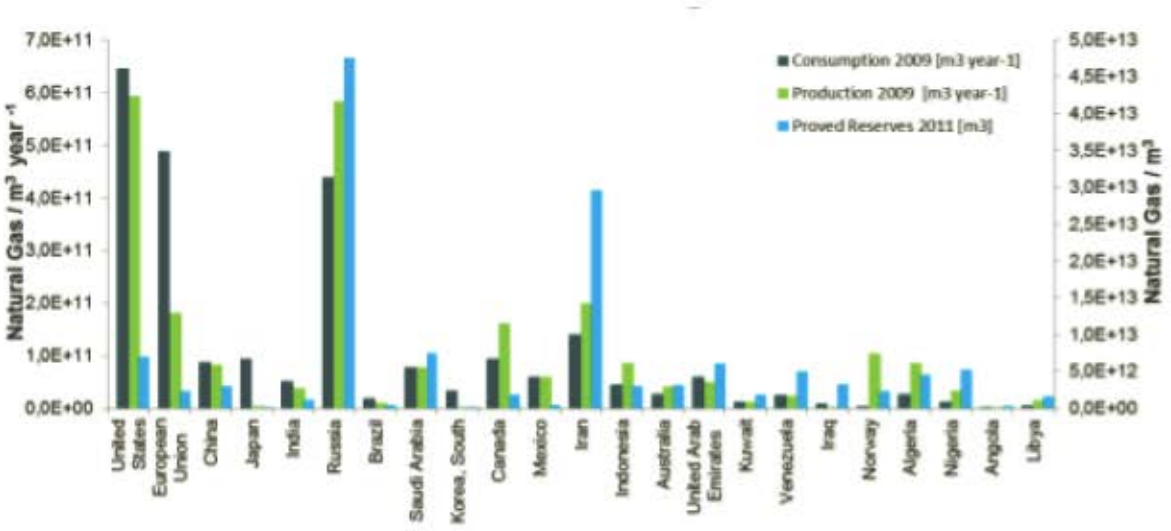

Figure 1.2: Distribution of World Natural Gas consumption, production and reserves [3]

creases. These consumers rely heavily on the importation of fossil fuels from the Middle East, Russia and Canada. Any political upheaval in the producer countries will thus have a major global economic impact.

A second major factor that spurred the development of alternative energy technologies is the environmental impact of combustion technologies of fossil fuel usage. One of the byproducts of fossil fuel combustion is carbon dioxide and carbon monoxide gases. Millions of tons of these gases are emitted into the atmosphere by industries and motorised transport. Environmentalist, atmospheric and earth scientists have identified these gases as major cause of the greenhouse effect, regional acidification and climate change.

There is therefore a need for efficient use of available energy resources and a search for alternative energy conversion technologies that are driving research into cleaner and more efficient ways of producing energy. The features which are required from alternative energy conversion technologies include high energy conversion efficiency, environmental friendliness, compatibility with renewable energy sources and sustainability. One such energy conversion technology which possesses the above char-

acteristics is a device called fuel cell. Fuel cell is an electrochemical device which converts the chemical energy of the reactants directly into electrical energy and heat without an intermediate combustion step. It is considered to be the most important anti-pollution technology in our history [1]. Unlike conventional batteries, a fuel cell does not run down or require recharging, but it operates as long as both fuel and oxidant are supplied. Therefore, the main attractive features of fuel cells systems are:

a) Energy efficiency: fuel cells are amongst the most efficient energy conversion devices. Moreover, they can be exploited in a wide range of applications due to their flexible operation, and can be applied for stationary, transport and portable applications.

b) Environment: fuel cells can help significantly reduce greenhouse gas emissions and urban pollution, and improve air quality. In combination with clean hydrogen (i.e. that produced from water and renewable energy), fuel cells provide emission free mobility. They are very quiet in operation, thus being very useful in areas where noise pollution is undesirable.

c) Energy security: fuel cells and hydrogen can support the development of decentralised structures building upon regionally available energy sources. This in return will reduce oil or gas imports, and at the same time it will meet the citizens needs in terms of power stability and predictability.

The different types of fuel cells are characterised by the electrolyte used. The Proton Exchange Membrane Fuel Cell (PEMFC), is characterised by the use of a polymer electrolyte membrane. The typical membrane used in low temperature PEMFCs is the DuPont‘s Nafion membrane. However, this membrane require sufficient water content for effective proton conduction, and are thus limited to operations below the boiling point of water. These membrane-based fuel cells therefore suffer from

several issues raised by low temperature operations such as complicated water management and high external humidification for both anode and cathode gases.

In recent years, high temperature proton exchange membrane fuel cells (HT-PEMFC) based on phosphoric acid-doped polybenzimidazole (PBI) membranes, which is the focus of this thesis, are experiencing increasing importance for residential and industrial application as combined power and heat units.

In particular, the development of high temperature fuels cells experience increasing importance in this field, since higher operating temperatures are beneficial to fuel cell performance [10, 11, 26, 13, 14, 15]. It increases reaction rate and higher mass transfer rate, but usually lowers cell ohmic resistance arising from higher ionic conductivity of the electrolyte membrane. In addition, at high temperature, CO poisoning can be alleviated by reducing chemisorptions of CO [8, 9, 10]. The development of temperature resistant PBI membranes allows fuel cells to work at temperatures up to 473 K [5, 6]. An additional advantage of these membranes is that PBI-based systems do not require humidification of the membrane [19, 20]. However, HT fuel cells have problematic aspects such as material problems related to corrosion, electrode degradation, electro-catalyst sintering and re-crystallisation and electrolyte loss.

The experimentally difficult environment of fuel cell systems motivated the development of mathematical models that can simulate and predict the performance of HT PEM fuel cells and stacks. A number of PEM fuel cell models for the general operating temperature cases have appeared in the literatures [63, 64, 65, 81, 70, 71, 72]. However, there still exist strong needs for studies on PEM fuel cells operating at high temperature, where water is in the vapour phase and the membrane has a water electro-osmosis drag force near zero. Under this condition, the performance of the membrane would be relatively independent of humidity, and water manage-

ment becomes unnecessary [24, 25]. PEM Fuel Cells exhibit a wide range of flow domains for the movement of mass, current and heat within the cells. Included in these domain ranges are convective flow in the gas channels and solid regions such as the metal matrix, diffusive flow in the porous gas diffusion layers, and even a hopping flow mechanism in the catalyst layers [17]. Often, exterior measurement of the fluxes only indicates the laminar flow property of a flux within a specific region. Though this is essentially true, the important flow properties at the interface between regions, e.g. the boundary movement between the gas channels and gas diffusion layers and between the gas diffusion layers and the semi- permeable membrane is generally neglected, or cannot be detected by such external means. It is in this environment that mathematical modelling will play a critical role in the detection, explanation and understanding of the complete functioning of PEM fuel cells, and in particular high temperature PEM fuel cells. It has the possibility to fulfil a vital function in supplying the energy needs in especially stationary power systems, but optimising its design and understanding the type of materials needed to operate effectively is to a great extend dependent on the type of research and modelling being done. It is hoped that this thesis will provide a valuable contribution to this effect.

1.2 Fuel Cell Operating Principles

A single fuel cell, as shown in Figure 1.3, illustrates the operational principle of a PEM fuel cell. Hydrogen gas in a pure or reformed form enters the anode channel and diffuses through the porous anode electrode towards the anode catalyst layer (ACL), where hydrogen molecules are stripped of their electrons with the help of a platinum catalyst and become positively charged hydrogen ions (protons), based on the hydrogen oxidation reaction (HOR):

$$2H_2 \rightarrow 4H^+ + 4e^- \tag{1.1}$$

Protons migrate through the ion-selective membrane and the electrons travel through the external circuit, thereby creating electric current. On the cathode side, an air stream enters the cathode channel and diffuses towards the cathode-side catalyst layer (CCL). At the platinum catalyst surface, protons recombine with electrons and oxygen molecules to produce water and heat, following the oxygen reduction reaction (ORR):

$$O_2 + 4H^+ + 4e^- \rightarrow 2H_2O \tag{1.2}$$

Reaction (1.1) is slightly endothermic and reaction (1.2) is strongly exothermic, so that overall heat is generated. By combining the reactions (1.1) and (1.2), the overall reaction in the PEM fuel cell can be summarised as

$$2H_2 + O_2 \rightarrow 2H_2O + heat + energy \tag{1.3}$$

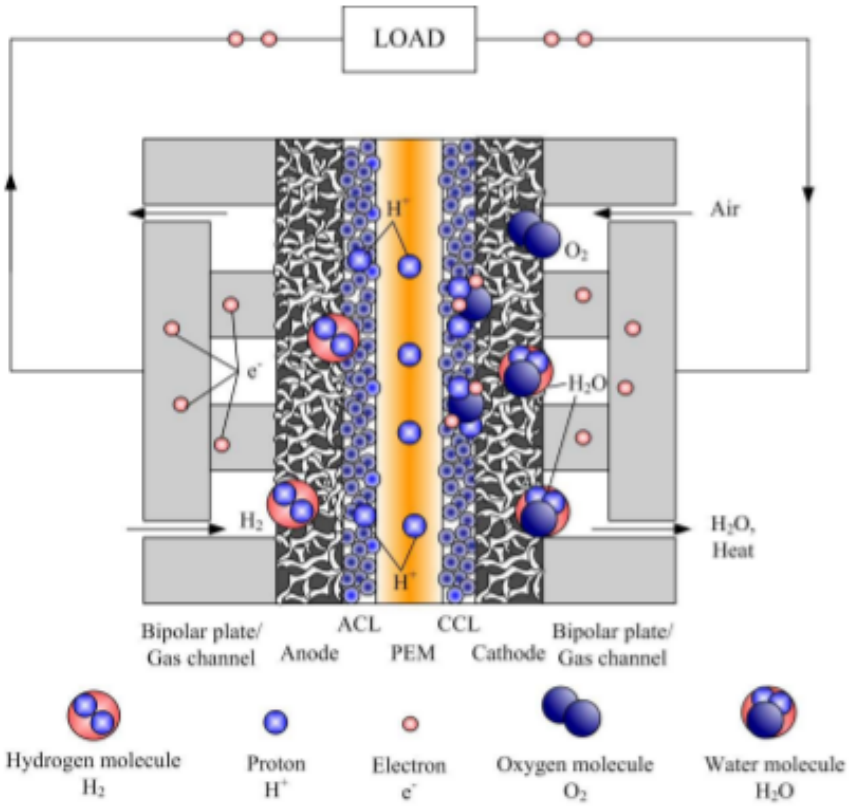

Figure 1.3: Schematic and Operation Principle of a PEM Fuel Cell [1]

The voltage of a single PEM fuel cell is typically in the range of 0.4 to 0.8 V and the cell current density is usually less than 1 A/cm^2 . In practice, the fuel cell shown in Figure 1.3 would be combined in series with other cells to produce a fuel cell stack. This fuel cell stack would then be part of a fuel cell system which would include fuel pumps, fuel processors, heat exchangers, and other equipment. The power of such PEM fuel cell systems can vary from a few watts which is suitable for portable applications, up to million watts such as in the stationary applications in power plant. A more detailed discussion on the PEM fuel cell and its applications, can be found in [4, 24].

1.3 PEMFC Components

A PEMFC consists of four main components: the proton exchange membrane, two catalyst layers (CLs), two gas diffusion layers (GDLs) and the bipolar plate, which contain the current collectors and gas channels. The system formed by the two GDLs, the two CLs and the membrane is known as the membrane electrode assembly (MEA). A short description is given of the composition and the physical phenomena taking place in each component.

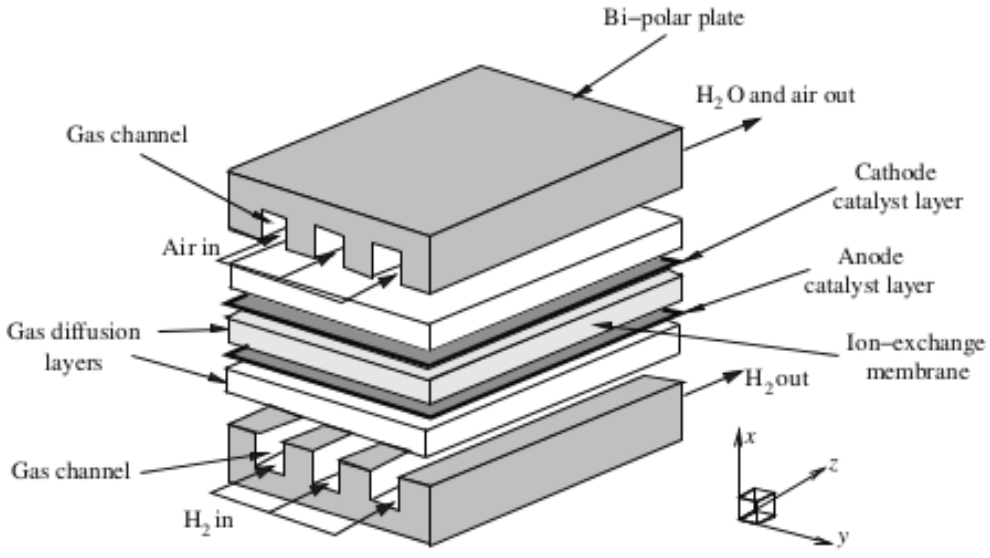

Figure 1.4: Fuel Cell Structure [4]

- **Polymer Electrolyte Membrane** : Consists of phosphoric acid-based membrane that conducts protons and repels electrons, forcing it to move through the outer circuit. The membrane is normally constructed with uniform thickness to minimise ohmic losses. A desirable membrane in a PEM fuel cell should possess the characteristics of high proton conductivity, good insulation regarding electronic current, low fuel crossover properties, and it must also be robust enough to be assembled into a fuel cell stack and have high chemical and thermal stability.

- **Catalyst layer** : Its prime function is to increase the rate of the electrochemical reactions. The catalyst layer usually consists of microscale carbon particles, each of which can support nanoscale platinum (Pt) catalyst particles, loosely embedded in a matrix of ionomer. The ionomer microstructure and ionomer- catalyst layer interface are important factors for the performance of a fuel cell; they determine the ion exchange across the membrane that allows the fuel cell reaction to occur. The optimum thickness of the catalyst layer is found to be around 10 μm since almost all of the reactions occur within a 10 μm thick layer. On the other hand, the electrochemical reaction is not evenly distributed over the catalyst layer; therefore, the Pt particles must be properly distributed in the catalyst layer to maximise the reaction efficiency and minimise the cost. The platinum catalyst has strong affinity for CO. Therefore, a common problem of the fuel cell is anode catalyst CO poisoning if the hydrogen is derived from an alcohol or hydrocarbon fuel. Developers are currently exploring platinum/ruthenium catalysts that are more insensitive to CO [21]. This problem does not exist if pure hydrogen is supplied.

- **Gas Diffusion Electrodes** : Consist of carbon fiber and they serve to transport the reactant gases towards the catalyst layer through its hydrophobic pore structure. They also provide an interface when ionisation takes place

and transfer electrons through the solid matrix. It also serve to provide structural support of the catalyst layer. A GDL also plays an important role in heat removal from the reacting site.

- **Bipolar Plates** :

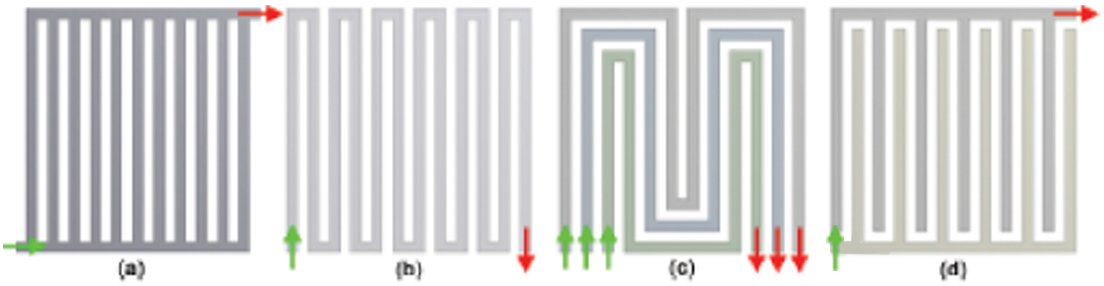

Figure 1.5: Common flow fields: (a) straight-parallel (b) single-serpentine (c) multiple-serpentine (d) interdigitated: green arrow- inlet; red arrow- outlet
[5]

The important role of the bipolar plate is to feed the reactant gases towards the GDL, and to assemble individual cells into a cell stack. The gas flow channels are carved into the bipolar plates, thus they feed reactant gases to the gas-diffusion electrodes. There need to exist a good electrical connection between the bipolar plates and the gas-diffusion layers in order to minimise contact resistance and hence ohmic losses. The channel area should be as large as possible to supply enough reactant gases and to reduce the cell weight and volume requirements; on the other hand, the greater the land area, the better the electrical connection between the bipolar plates and the GDL, and the lower the contact resistance and ohmic losses. A sensible compromise between the above two factors should be sought to achieve the best possible cell performance.

Research into the optimum configuration of the bipolar plate flow-field is ongoing [5], and there exist in industry variations in flow-field configurations such as the straight-parallel, single-serpentine, multi-serpentine, interdigitated, or

the combination of more than one designs as shown in Figure 1.4. Each configuration has its own advantages and draw-backs and are widely reported in the literature. The most commonly used material in bipolar plate fabrication is graphite; it has favourable properties such as high electrical conductivity, high thermal conductivity, low corrosion rate, and light weight. However, it is expensive to machine the flow pathways into graphite. Apart from graphite, metal alloy and carbon composites are also materials widely used for manufacturing bipolar plates.

1.4 PEMFC Thermodynamics

The performance of a fuel cell in an ideal environment can be described by the fundamental laws of thermodynamics. From the first and second laws, we may deduce that the specific reversible work of the fuel cell (W_{rev}) is equal to the Gibbs free energy of the reaction, ΔG_r, [57]:

$$W_{rev} = \Delta G_r \tag{1.4}$$

The reversible efficiency (η_{rev}) of the fuel cell is defined as the ratio of the Gibbs free energy of the reaction to the reaction enthalpy (ΔH_r):

$$\eta_{rev} = \frac{\Delta G_r}{\Delta H_r} = 1 - \frac{T\Delta S_r}{\Delta H_r} \tag{1.5}$$

The reversible power of the fuel cell can be written as the product of the specific reversible work and the molar flow of the reactant:

$$P_{rev} = \dot{n} W_{rev} \tag{1.6}$$

This power equation can be compared to the power in an electrical device:

$$P_{rev} = V_{rev} I \tag{1.7}$$

where V_{rev} is the reversible voltage and I the current. This in turn is related to the molar flow of the reactant, according to Faraday's Law:

$$I = -nF\dot{n} \tag{1.8}$$

where F is Faraday's constant and n the number of electrons that are released during the ionisation process per fuel molecule. Combining equations (1.4) to (1.8) we have:

$$\eta_{rev} = \frac{-\Delta G_r}{nF} \tag{1.9}$$

which is the fundamental equation that describes the electromotive force of an ideal fuel cell. The Gibbs free energy for the most common reactions under standard conditions (G_r^0) is tabulated, and we can use the Nernst equation to express V_{rev} in terms of these tabulated values:

$$V_{rev} = \frac{-\Delta G_r}{nF} - \frac{RT}{nF} \ln \frac{\prod(x_{pt}^{st})}{\prod x_{rt}^{st}} \tag{1.10}$$

where x_{pt} and x_{rt} represents the concentration of the reactants and products at the reaction sites, and the suffix st stands for stoichiometric coefficient. In practice V_{rev} represents the theoretical open circuit voltage of the cell, and we can substitute V_{rev} with V_{oc}.

The voltage of a real cell hardly ever meets this theoretical value due to irreversibilities arising in the operation. This is shown in figure 1.4.

The cell voltage of an irreversible fuel cell is given as:

$$V = V_{oc} - (\eta_{act} + \eta_{conc})_a - (\eta_{act} + \eta_{conc})_c - \eta_{ohm} - \eta_{cross} \tag{1.11}$$

where the voltage drop ($V - V_{oc}$) is represented by the following irreversibilities [57]:

Activation losses which are caused by the slowness of the reactions taking place

on the surface of the electrodes. Part of the voltage generated is lost in driving the chemical reaction that transfers the electrons to and from the electrode. This overpotential is described by the Tafel equation [24]:

$$\eta_{act} = b \ln \frac{i}{i_0} \tag{1.12}$$

where i is the observed current density and b is the Tafel-slope, which depends on the electrochemistry of the particular reaction, and i_0 is the exchange current density of the anodic reaction.

Ohmic losses result from the resistance of the electrolyte and due to the electrical resistance of the electrodes. It is given by [12]:

$$\eta_{ohm} = ir_i \tag{1.13}$$

where r_i is the internal resistance. Ohmic loss is the most common cause of potential loss in a fuel cell. Reducing the thickness of the electrolyte layer between the anode and cathode is thought to be a way of eliminating ohmic overpotential, but this may cause the problem of crossover or intermixing of anodic and cathodic reactants.

Concentration (mass transport) losses results from the change in concentration of the reactants at the surface of the electrodes as the reactants are being consumed [23]. At a sufficiently high current density, the rate of the reaction consumption becomes equal to the amount of reactants supplied by diffusion, called the limiting current density. The voltage drop for a current density i due to the concentration overpotential is equal to [81]

$$\eta_{conc} = \frac{RT}{2F} \ln(1 - \frac{i}{i_l}) \tag{1.14}$$

where i_l is the limiting current density and R the universal gas constant.

When examining the polarisation curves given in figure 1.6, it is helpful to divide

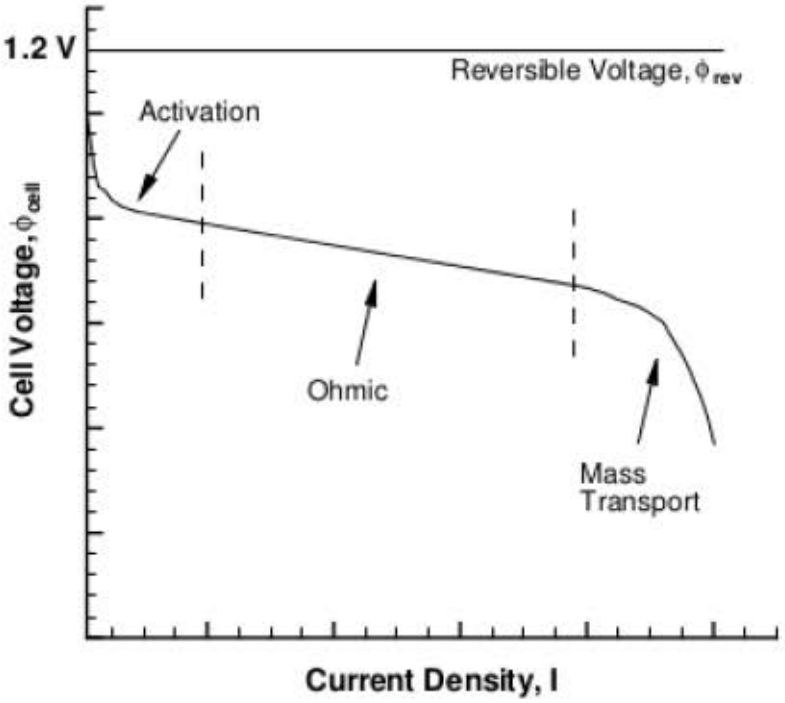

Figure 1.6: Schematic Polarisation Curve showing the three overpotential regions [57]

the curve into three regions. A different mode of irreversible loss dominates each of these regions, although they coexist simultaneously in each region. Thus, the shape of the polarisation curve can provide the viewer with some information regarding the internal dynamics of the fuel cell.

- The first region is called the activation polarisation region. It is associated with a steep slope and low current densities. This region occurs due to a sluggishness of electro-catalysis at low voltage drops across the cell. In order to provide the electro-catalysis, an activation energy is required to drive the reaction, thus providing the name for this region. In this region, cell voltages (and hence efficiencies) are high, but current density (and hence power density) is very low. Thus, this is not a very useful region in which to operate a practical fuel cell.

- The second region is called the ohmic polarisation region. It is associated with a gradual slope that traverses most of the polarisation curve. The losses associated with the activation polarisation are relatively constant in this region, hence the slope is principally due to ohmic losses across the membrane and electrode layers.

- The third region is called the concentration polarisation region. It is associated with a steep slope and high current densities. In this region, the transport processes of this electro-chemical device begin to limit performance. Mass diffusion rates limit the transport of the reactants, thus preventing an increase in reaction rate. Decreasing the cell potential in this region results in a negligible increase in current density, thus simply reducing the power density. The maximum current is reached at zero cell potential.

The relationship between overpotential, current density and power density in a fuel cell is illustrated in figure 1.7 below [123]:

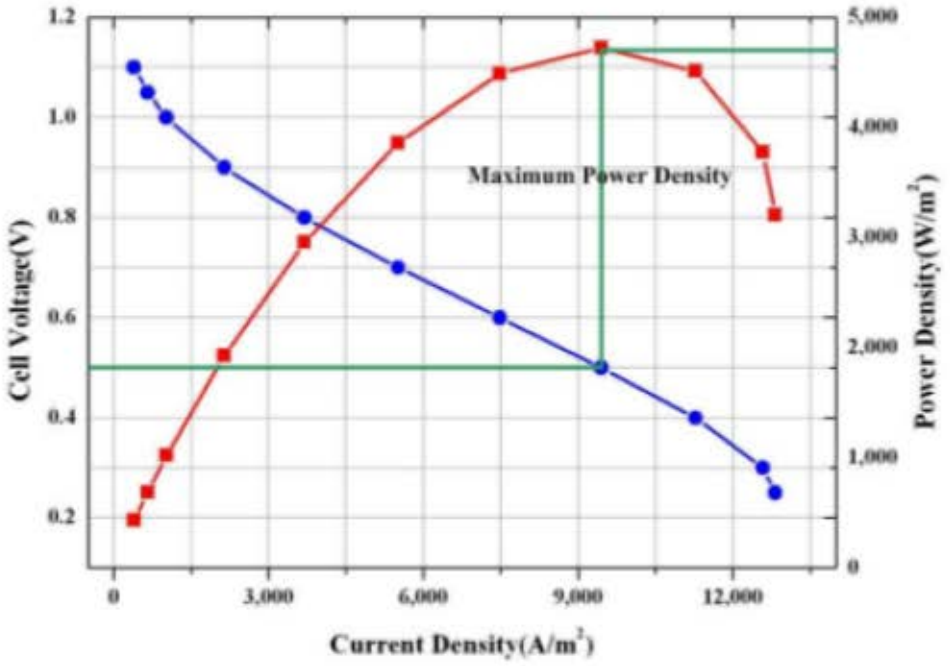

Figure 1.7: Schematic of Fuel Cell Potential, Current Density and Power Density Relationship [123].The plot in blue is a repetition of the Polarisation Curve presented in figure 1.6 above, but it is accompanied by the generated Power density plot in in red. The graph illustrates the maximum power density reached by the fuel cell and the corresponding cell potential and current density at which this occur, as indicated by the green lines.

1.5 PEMFC Literature Review

Proton exchange membrane fuel cell technology has been recognised now for a few decades as a leading source for zero or low emission power source that can be utilised for transportation or combined heat and power (CHP) systems. Still, its commercialisation is hindered by several hurdles. The numerous advantages of fuel cells, as an energy generating source, such as high efficiency, low emissions and silent operations, are often cancelled by hurdles such as high cost and low durability compared to conventional internal combustion engines [57]. Improving performance and achieving cost reduction can be achieved by broadening the understanding of the complex processes within the fuel cell. Many of these internal processes are impossible to measure in-situ, though some elaborate and expensive laboratory measurements were made. Increasingly, mathematical modelling is being used as

a tool to understand the complex processes, and to assist in the ability to predict failures, conduct troubleshooting operations, and to optimise the design and operating conditions of fuel cells [64, 65].

Modelling of fuel cells involves the integration of the inherent fuel cell physics to a geometrical model. Detailed fuel cell models normally consist of many highly coupled nonlinear partial differential equations that govern the conservation of numerous physical species in different modelling domains, which in turn results in the numerical analysis being computationally intensive. Depending on the degree of complexity, fuel cells can be modelled into zero-dimensional, one-dimensional, two-dimensional or three-dimensional models. Bernandi and Verbrugge [81] and Springer et al.[70] were among the first to develop one-dimensional models of PEM fuel cells, which analysed the flow across the membrane. The research, however, focused mainly on the investigation of processes in the anode to cathode direction, across the membrane, without considering the effects of concentration gradients in other directions, affecting the predictive capability of the one-dimensional model.

More realistic models led to the development of two-dimensional models [71, 72, 74, 75]. These models were more accurate, and also more computationally intensive than the one-dimensional models. The two-dimensional models still had limited effectiveness, since mass transport limitations in the third direction was absent [77]. More efforts were consequently directed towards three-dimensional fuel cell models. Hu et al. [78] developed an isothermal, two-phase three-dimensional model for a PEM fuel cell that accounted for the transport of liquid water within the porous electrodes and water that is dissolved in the ion-conducting polymer. The development was further advanced by Ubong et al. [79] who analysed the influence of various operating conditions, like stoichiometry and pressure on performance. Also, species distribution within the polybenzimidazole (PBI) membrane for high temperature PEM fuel cells. Berning et al. [81], explored fuel cell performance

under various operating conditions, using a single phase, non-isothermal, three-dimensional model. It was observed that the region under the collector plate land area exercised considerable influence on the current density. This phenomena is not observable with the use of one-dimensional or two-dimensional models. Wang and Wang [80], used a three-dimensional, single phase, isothermal model to explore large density and velocity variations in PEM fuel cells. Their results indicate deceleration of anode gas flow under low stoichiometry, with no significant change in hydrogen concentration. Ferng and Su [83], did both numerical and experimental analysis on PEM fuel cells. They developed an isothermal, three-dimensional model to analyse the effects of different flow channel designs on the performance of the fuel cell. The flow channels included parallel and serpentine flow channels, single and multi-path channels, also uniform depth and step-wise depth flow channels. The study concluded that parallel flow channels effectively improve fuel cell performance.

Other critical hurdles in fuel cell performance, which emerged over the last decade, is carbon monoxide (CO) poisoning and water management of the electrolyte membrane, either as a flooding or drying problem. The carbon monoxide problem stems from the use of carbon reformates as a source of hydrogen. At temperatures below 100^0C the platinum electrodes shows as much affinity to the CO-molecules than to the H_2-molecules, resulting in CO taking the place of H_2 on the reacting sites. This is especially true if more than 2 ppm of CO (per volume) in the supplied hydrogen is present. This CO-poisoning can be prevented if pure hydrogen is used. However, a lack of hydrogen refuelling infrastructure and on-board hydrogen storage problems results in pure hydrogen fuel being unattractive for practical applications. Reformation of a liquid hydrocarbon, such as methanol normally will solve the infrastructure and on-board problems. Another solution is to increase the operation temperature which will enhance CO-tolerance, but also this will increase the electrochemical kinetics, and solve the other problem of liquid water flooding that blocks the spaces through ion migration takes place. Thus, in the past decade high temperature fuel

cells attracted growing interest.

Though it is recognised that HT PEMFC has many attractive features, only a few studies on HT PEMFC have been published until 2010, [58, 44, 43, 61, 62]. Many of the modelling efforts over the last 20 years focused on low temperature PEMFC with Nafion membranes [31, 32, 38, 39, 40]. However, research on HT PEMFC with a PBI membrane began around six years ago and there remains a lack of modelling work. Only a few steady-state models for the HT PEMFC have been reported [22, 43, 44, 45, 46, 47]. Cheddie and Munroe were the first authors to develop a model of the HT PEMFC [41, 42, 44]. They developed one-, two and three dimensional models. Their 3-D model compared the results of the previous 2-D model. They found that the 2 -D model overestimated performance by neglecting rib effects. The oxygen depletion occurred mainly in the catalyst layer under the ribs, and it was more predominant at lower flow rates. They also analysed the temperature profile inside the cell, the hottest point was observed in the membrane under the land and a temperature variation in the cell of 19 K was observed at a power density of 1000 $W.m^{-2}$. These results was also reported in a review by Ubong et al. [79]. However, they ignored the current distribution in the electrocatalyst layers, and assumed high field (Tafel) approximation to describe electrode kinetics.

In the same year Peng and Lee [22] developed a three-dimensional non-isothermal numerical model which used as computational domain a single straight channel. Like Cheddie and Munroe [44] they also found that maximum current density occurs under the land areas. With the analysis of the temperature profile they found that the higher temperature was located in the cathode catalyst layer and the temperature variations across the cell increased with increasing current density. In 2008 Peng et al. [88] used the same computational domain of the previous work [22] to develop a three-dimensional dynamic model. Its main feature was the introduction of an accumulation term in the model, and they observed the charge double layer

effect. The double layer occurs in a thin layer adjacent to the reaction interface. Electrons accumulate on the surface of the electrode and protons on the surface of the electrolyte and therefore the interface stores electrical charge and acts as an electric capacitor and upon a load change it will take some time to dissipate [114, 86, 121, 88]

Scott et al. [45] developed a steady-state, isothermal one-dimensional model which included the potential and current distributions in the catalyst layers. The model considered the effect of mass transport through the electrolyte film covering the catalyst layers.

One of the most important challenges for HT PEMFCs is to improve lifetime. At 150^0C, Li [26] reported a lifetime of 5000 hours by continuous operation with pure oxygen at 0.5 V. He also found that above 180^0C the fuel cell started to fail much earlier, probably due to polymer oxidative degradation. Schmidt and Baurmeister [35] reported a degradation rate of 5-6 μ V h^{-1} which corresponds to a lifetime of over 20 000 hours, with an operating temperature of 160^0C and air used in the cathode.
The reasons behind failure after a certain period of operation can be numerous, but three mechanisms are the most common [58, 59, 77, 61]:

- Degradation of the polymer membranes due to the attack of H_2O_2 and its radicals.

- Leaching of the doping acid from the membrane and catalyst layers.

- Loss of catalyst activity due to the catalyst sintering, catalyst dissolution and carbon support corrosion.

Fuel cells are characterised by the steady-state response, but recent research [121, 88], attempt to get more detailed information from transient response measurements such as electrochemical impedance spectroscopy experiments. This technique determines the fuel cell impedance along the frequency domain characterising phenomena at different time scales [89]. The spectra can be modelled using electrical equivalent circuits, and the corresponding parameters can be obtained by fitting to the experimental results [90, 91]. Jaouen et al. [89] considered a spherical agglomerate model where gases are fully transported by diffusion and convection before dissolving in the electrolyte phase and reaching the catalyst particles. However, this analysis gives a simplified picture of the fuel cell presentation and it becomes difficult to assign physical meaning to the EIS spectra parameters.

1.5.1 Summary

It is evident from the preceding literature review that researchers, particularly the fuel cell modelling community, responded to the demands and challenges of making fuel cells commercially viable. Two key factors are the main drivers: fuel cell performance and durability.

Investigations on transport phenomena; electrochemistry under different catalyst loads; current distributions and cell potentials under different parametric conditions, are all examples of mathematical research models designed to understand the problem of fuel cell performance.

Similarly, the review also shows investigations into CO contamination, catalyst degradation, hydration and dehydration effects on the membrane under different temperature conditions etc. All of this research models are designed in order to understand more fully the problem of fuel cell performance.

It is however hard, if not impossible to divorce the physical processes occurring in one component from those in the other components, despite the various components possessing quite distinct and disparate characteristics. This fact compromises many of the mathematical models in the open literature, where a fuel cell component is modelled, but the processes in many of the other components are over-simplified.

There is a distinct shortage in high temperature fuel cell research with mathematical modelling output, and most of those that exist either has single phenomena characteristic or are empirically designed to fit existing experimental results.

It is hence, one of the main objectives of this thesis to present a fully comprehensive, three-dimensional model of a high temperature fuel cell, so that the mutual interaction between physical phenomena in the various cell components can be better understood and meaningful contributions can be made to both the design and optimisation of high temperature polymer electrolyte fuel cells.

1.6 Thesis Objectives and Scope

The main objectives of this thesis are:

- To develop a comprehensive and rigorous three-dimensional mathematical model for the numerical simulation of a hydrogen-fed high temperature proton exchange membrane fuel cell in the steady state. This objective is obtained via the following goals:

    1. Describe the performance of a HT PEMFC through the development of a mathematical model through which mass transport, momentum transport and species transport are described, using the conservation equations.

2. Describe the transport of charges, heat and energy by the development of an electrolyte component for the mathematical model and using the conservation of energy equations.

3. Describe the reaction kinetics by the development of an electrochemistry component for the mathematical model.

- Develop a Numerical Algorithm to solve the mathematical model, and implement the algorithm in Ansys FLUENT, a commercial software.

- Prove the validity of the numerical tool, and hence the mathematical model by comparing numerical results with experimental data from the literature and other established fuel cell research laboratories.

1.7 Thesis Outline

The thesis is constructed through the follow chapter:

- **Chapter 1** : **Introduction**, the context and background of this Thesis are described, and an introduction to fuel cells and, in particular, to proton exchange membrane fuel cell is provided.

- **Chapter 2** : **Mathematical Model**, the derivation and justification of the mathematical equations used in the model are explained in detail.

- **Chapter 3** : **Numerical Formulation**, the finite-volume-based numerical algorithm to solve the mathematical model described in Chapter 2 is presented.

- **Chapter 4** : **Results and Validation**, the validity of the resulting numerical tool is assessed by comparing the numerical predictions for the performance of a given high temperature proton exchange membrane fuel cell with its experimental characteristic performance curve, taken from the literature.

- **Chapter 5** : **Summary and Conclusions**, the main conclusions are drawn.

Chapter 2

Mathematical Formulation

In this chapter a comprehensive three-dimensional model is developed to describe the numerical simulation of the multi-physics operation of a high temperature polymer electrolyte membrane fuel cell. The operating principle of a high temperature proton exchange membrane fuel cell, involves a complex network of inter-connected physical phenomena, which take place simultaneously within several components of a HT PEMFC . The governing equations that describe a given physical phenomenon may be dependent on the HT PEMFC component considered; this is due to the different nature of the HT PEMFC components (porous media, gas ducts, impervious solids). Though a single modelling domain is used in this thesis research, the phenomenon in each component in a HT PEMFC is considered with the appropriate equations. These separate components include fuel cell current collectors, the gas flow channels, the gas diffusion electrodes, catalyst layers and the electrode membrane.

The mathematical model that describes the physical phenomena and the state or constitutive equations that are accounted for in each component of the fuel cell are presented in the sections that follow. In section 2.1 we introduce a certain level of simplification used in the model. The assumptions that are necessary for the simplification of the model are provided. In section 2.2 the transport of gas species

through the different components of the fuel cell is described, and the appropriate conservation equations that describe these phenomena are explained. In section 2.3 the sequence of electrochemical reactions at the anode and cathode catalyst layers are explained. In section 2.4, the formation and transport of heat and energy are described. A description of the transport of electric charge is provided in section 2.4. In sections 2.5 and 2.6, the model's boundary conditions and the input parameters used are described.

2.1 Assumptions

- gravity effects are ignored;
- the gas reactants are ideal gases;
- the gas flow in the channel is laminar flow;
- the cell is operated with pure hydrogen, thus no contamination effects are considered;

Furthermore, there are a few other assumptions that pertain to certain transport phenomena. They will be illustrated in the context of specific transport processes.

2.2 Transport of Gas Species

In this section, the mathematical model that describes the flow of reactants and products along a HT PEMFC channel, either in the fuel channel or in the air channel, is described. The HT PEMFC channels are pipes along which the gaseous reactants mixtures are driven from the HT PEMFC inlet to the electrodes. The byproducts of the electrochemical reactions (also in gaseous state, if any) exit the

electrode and join the unconverted reactants in the channel, where they are evacuated to the HT PEMFC outlet. In the channel the flux of gaseous mixtures are both convective and diffusive, especially during the flux of species from the gas channels into the porous electrodes. The channel model accounts for the principles of conservation of mass, both in terms of total mass and species mass, as well as for the second law of Newton, considered by means of the (linear) momentum-conservation equation [34]. These phenomena are described below.

2.2.1 Conservation of Mass (Continuity Equation)

The differential form of the continuity equation is:

$$\frac{\partial(\rho_g)}{\partial t} + \nabla \cdot (\rho_g \vec{u_g}) = S_m \tag{2.1}$$

where ρ_g, $\vec{u_g}$ are the superficial values of the density and velocity of the fluid. The velocity vector $\vec{u} = (u, v, w)$ in three dimensional space. S_m is the mass source term, which represents an increase or decrease in mass and is dependent on the cell region. In the case of the air and fuel channels where the gases experience no chemical reactions that will result in the formation or depletion of species, $S_m = 0$. The first term in the equation represents the transient rate of mass flow per unit volume and the second term the convective flow of mass per unit volume in the gas channels.

Due to the high operating temperatures, the fluids present in a high temperature PEM fuel-cell are in a gaseous state. The ideal gas law is thus used as the equation of state for the fluid density:

$$\rho \frac{pM}{RT} \tag{2.2}$$

2.2.2 Conservation of Species

Several gas species are transported through the gas channel regions of the fuel cell. This transport is governed by a general convection-diffusion equation of the form:

$$\frac{\partial C_i}{\partial t} + \nabla \cdot (\vec{u_g} C_i) = \nabla \cdot (D_{i,m}^{\text{eff}}) \nabla C_i + S_i \tag{2.3}$$

where C_i is the concentration of the ith species; S_i is the gain/loss of the ith species; $D_{i,m}^{eff}$ represents the effective mass diffusion coefficient for species i in the mixture.

One extra relation is required to close the equation set for the gas phase transport:

$$\sum_{i=1}^{N} X_i = 1 \tag{2.4}$$

where N denotes the number of species in the fuel cell, and X_i denotes the species molar fraction which is evaluated as

$$X_i = \frac{C_i}{\sum_{i=1}^{N} C_i} \tag{2.5}$$

with the assumption that the cell is fed with pure hydrogen at the anode side and air at the cathode side, there are mainly four species to be considered in this study, namely hydrogen, oxygen, water vapor, and nitrogen. Only the first three of the four species need to be numerically resolved, leaving the fourth one to be determined through Equation (2.3). Furthermore, the continuity equation and the species transport equation are correlated through the following relations

$$S_m = \sum_{i=1}^{N} S_i \tag{2.6}$$

$$\rho_g = \sum_{i=1}^{N} M_i C_i \tag{2.7}$$

where M_i denotes the molecular weight of the ith species.

It should be noted that the thermal (Soret) and pressure diffusion effects are ne-

glected in the diffusion flux, which is the first term on the right hand side of Equation (2.2), since their gradients are relatively insignificant compared to the concentration gradient in PEM fuel cells. Finally, the diffusion flux is approximated using Ficks law. It can serve as an acceptable approximation for a multi-component system as well, provided that a corrected diffusivity $D_{i,m}^{\text{eff}}$ is used [53]

$$D_{i,m}^{\text{eff}} = \frac{1 - X_i}{\sum_{j,j\neq i} \frac{X_j}{\mathcal{D}_{ij}^{\text{eff}}}} \tag{2.8}$$

where $\mathcal{D}_{ij}^{\text{eff}}$ is the effective binary mass diffusion coefficient of component i in component j. It is determined by

$$\mathcal{D}_{ij}^{\text{eff}} = \mathcal{D}_{ij} \frac{T}{T^{\text{ref}}} \frac{P^{\text{ref}}}{P} \frac{\varepsilon}{\tau} \tag{2.9}$$

where $\mathcal{D}_{ij}$ is the bulk binary diffusivity at the reference temperature ($T^{\text{ref}} = 20^0 C$), and pressure ($P^{\text{ref}} = 1$ atm); ε the porosity and τ the tortuosity of the porous material.

2.2.3 Conservation of Momentum

The momentum conservation equation accounts for the mass-average velocity of gas masses in the gas channels. In differential form the momentum conservation equation is:

$$\frac{\partial(\rho_g \vec{u_g})}{\partial t} + \nabla \cdot (\rho_g \vec{u_g} \vec{u_g}) - \nabla \cdot \vec{\tau_g} = S_u \tag{2.10}$$

where S_u is the momentum source or sink term, dependent on the cell region, and in the case of the gas channels, $S_u = 0$ for low flow velocity, as is the case for high temperature PEM fuel cells; and τ_g is the molecular stress tensor. In high temperature PEMFC all gas fluids are regarded as Newtonian fluids. According to the constitutive relation for a Newtonian fluid, the stress tensor may then be

written as:

$$\tau = \mu \left[\nabla \vec{u_g} + (\nabla \vec{u_g})^T\right] - \left[p + (\mu_V - \frac{2}{3}\mu)\nabla \cdot \vec{u_g}\right] \tag{2.11}$$

where μ_V is the coefficient of bulk viscosity, and μ is the dynamic viscosity of the fluid. Also, under the operating condition of high temperature PEMFC, such as low flow velocity, the bulk viscosity, μ_V can be regarded as zero. Thus, the momentum conservation equation for the channel may be expressed as:

$$\begin{aligned}\frac{\partial(\rho_g \vec{u_g})}{\partial t} + \nabla \cdot (\rho_g \vec{u_g} \vec{u_g}) - \nabla \cdot (\nabla \vec{u_g}) = -\nabla \left(p + \frac{2}{3}\mu_g \nabla \cdot \vec{u_g}\right) + \\ \nabla \cdot \left[\mu_g (\nabla \vec{u_g})^T\right] + S_u\end{aligned} \tag{2.12}$$

2.2.4 Transport of Water

One of the major advantages of phosphoric acid doped PBI membranes is that the reactant gases do not need to be humidified. Therefore, most of the research on PBI-H_3PO_4 membranes is done with dry reactants. However, in real world applications it is almost impossible to supply dry reactants. Furthermore, working with pure hydrogen in order to reduce fuel consumption requires periodical purges due to dilution of the hydrogen on the anode side. Dilution is caused by the permeation of nitrogen and water molecules from the cathode. With nitrogen permeation through the membrane reportedly being very low [36], water build-up on the anode could be the main reason behind the necessity of a purge. It is therefore important to investigate the effects of water vapor on the cells performance.

Proton conduction mechanism in the PBI-H_3PO_4 membranes is not water assisted. It is primarily structure diffusion where proton migration occurs between hydrogen

bonds (Grotthuss mechanism) [2]. However, water still plays an important role in the reaction mechanisms. The presence of water ionizes phosphoric acid and increases proton activity that in turn enhances the oxygen reduction reaction [37]. Furthermore, solubility of oxygen in water is much higher than in H_3PO_4. Therefore, with higher water content in the electrolyte the oxygen concentration in the catalyst layer increases and at the same time oxygen diffusion is improved due to decreased viscosity of the electrolyte [37]. It is clear that the water, which is always going to be present, influences the way the HTPEM fuel cell works and it is the opinion of this research that investigating water transport in the membrane electrode assembly (MEA) is of relevant interest. Data on the water transport within PBI-H_3PO_4 membranes and MEAs is very scarce in the literature and to the best of my knowledge there is only one group of authors that has so far quantified this phenomenon [28].

The electro-osmotic drag is reported to be virtually zero for PBI-H_3PO_4 membranes [20, 26], and could be one of the main reasons why no known water management model exist for PBI-H_3PO_4 membranes. In this research the only mechanism assumed here to drive water vapor molecules across the MEA is the water vapor partial pressure gradient across the MEA. We consider in this thesis work aspects of the water transport model developed for a low temperature Nafion membrane electrode assembly to ascertain whether it could suitably be used for PBI-H_3PO_4 membranes.

In a HT PEMFC water appears in two phases, the “vapor” phase and the “dissolved” phase. Water vapor molecules enter the gas channels with the inflow gases. The molecules diffuse to the polymer electrolyte and are localized and less connected in the small pores of the electrolyte. It is therefore assumed to be in a “dissolved” phase in the electrolyte layer.

The transport of water vapor is governed by the same convection-diffusion equation as the transport of hydrogen and oxygen:

$$\frac{\partial \varepsilon_m C_v}{\partial t} + \nabla \cdot (-D_v \nabla C_v) + \nabla \cdot (\vec{u_g} C_v) = S_v \tag{2.13}$$

where C_v is the water vapor concentration, D_v is the water vapor diffusivity and S_v is the water vapor source term. The source term remains zero in the gas channels, but in the polymer electrolyte and the catalyst layers some water vapor is changed to dissolved water, then $S_v = -S_{vd}$, so that both phases, water vapor and dissolved water exist.

In the cathode catalyst, water is produced by the oxygen reduction reaction, so that

$$S_v = -S_{vd} + \frac{\mathcal{R}}{2\mathcal{F}} \tag{2.14}$$

At the cathode catalyst layer, water is generated at the solid catalyst surface for both PBI and Nafion membrane electrode assemblies. Together with the water vapor from the air gas channel that diffuses towards the cathode catalyst surface, a significant water vapor partial pressure gradient will exist between the anode and cathode sides of the membrane. This results in water vapor movement from from the cathode to the anode side. However, for a Nafion MEA we have at the anode catalyst layer, water molecules tend to move with the protons towards the cathode catalyst layer by means of electro-osmotic drag. At the cathode catalyst layer, water is generated at the solid catalyst surface and the enhanced local water concentration tends to counteract the water movement from the anode side. If the concentration gradient is large enough, water will diffuse back to the anode side. Following the diffusive approach proposed by [70]. This proses is described by:

$$\frac{\partial \varepsilon_m C_d}{\partial t} + \nabla \cdot (-D_d \nabla C_d) + \nabla \cdot (\frac{n_d}{F} \vec{J}_m) = S_{vd} \tag{2.15}$$

where C_d is the dissolved membrane water concentration, ε_m is the volume fraction

of the polymer membrane, D_d is the dissolved water diffusivity in the electrolyte, n_d is the electro-osmotic drag coefficient. $\vec{J}_m$ is the membrane phase current density, s_{vd} is the source term of the dissolved phase.

Note that the third term in equation (2.13) disappears for PBI membranes.
D_d in the electrolyte is usually determined based on a curve fit formula of experimental data. In this thesis we use the one proposed by Kulikosoly [51]:

$$D_d = \varepsilon_m .41 \times 10^{-10} \left(\frac{\lambda}{25}^{0} .15\right) \left[1 + \tanh\left(\frac{\lambda - 2.5}{1.4}\right)\right] \tag{2.16}$$

where λ is the number of water molecules per sulphonic acid group within the polymer electrolyte. It relates to the dissolved water concentration as:

$$\lambda = \frac{EW}{\rho_m} C_d \tag{2.17}$$

where EW is the equivalent molecular weight of the dry membrane. n_d is also an empirical formula that is experimentally determined. In this study, the linear function developed by [70] is employed:

$$n_d = \frac{2.5}{22}\lambda \tag{2.18}$$

The source term, S_{vd}, for the conversion of water vapor to dissolved water in the membrane are determined by:

$$S_{vd} = \gamma_a \frac{\rho_m}{EW} (\lambda_e - \lambda) \tag{2.19}$$

where γ_a is determined by the empirical formula, developed by Ge [54]:

$$\frac{1.14 \times 10^{-5} f_V}{\delta_{Cl}} \exp\left[2416\left(\frac{1}{303} - \frac{1}{T}\right)\right] \tag{2.20}$$

where, δ_{Cl} is the thickness of the catalyst layer, F_V, the volume fraction of the water in the electrolyte membrane, given by

$$f_V = \frac{\lambda V_W}{V_m + \lambda V_W} \tag{2.21}$$

where, V_W and V_m are the molar volume of the water and the dry membrane.

In PBI membranes the dissolved water content, represented by S_{vd} is determined differently, and is only a function of the concentration differences between water vapor in the cathode catalyst layer and the anode catalyst layer [68]:

$$S_{vd} = D_v \frac{C_{H_2O,CCl} - C_{H_2O,ACl}}{\delta_{mem}} M_{H_2O} \tag{2.22}$$

where D_v is the water vapor diffusivity, $C_{H_2O,CCl}$ and $C_{H_2O,ACl}$ are the water vapor concentrations in the cathode catalyst layer and anode catalyst layer, respectively, δ_{mem} is the thickness of the membrane and M_{H_2O} the molecular weight of water.

2.2.5 Reaction Kinetics

The species source term (S_i) on the right hand side (RHS) of Equation (2.2) accounts for the consumption or production of species due to electrochemical reactions or phase changes. The catalyst layers are located at the interfaces between the polymer electrolyte membrane and the gas diffusion electrodes, and are the sites where electrochemical reactions occur with gas species that diffused through the porous electrodes. The main reaction in the anode catalyst layer is the electro-oxidation of hydrogen (HOR), while the main reaction at cathode catalyst layer is the oxygen reduction reaction (ORR). Other reactions that occur include carbon monoxide adsorption and desorption in the anode catalyst layer. Only the main reactions are considered in this thesis. Mainly because the influence that reactions with carbon monoxide have in low temperature PEM fuel cells is significantly reduced for high temperature PEM fuel cells. Thus, the objective for this section is to establish the relation between the rate of hydrogen and oxygen consumption, and the electrochemical reaction kinetics.

Anode Reaction Kinetics

The gas present at the anode catalyst layer is hydrogen. The cross-over effect of oxygen is ignored, since the membrane is assumed to be impermeable to gases in this study. The reaction therefore considered is the adsorption, desorption and electro-oxidation of hydrogen. The adsorption and electro-oxidation of hydrogen in an acidic environment has been extensively studied. The electro-chemical oxidation of hydrogen over platinum, in an acidic medium, involve the slow dissociation of adsorbed hydrogen molecules to hydrogen atoms, known as the Tafel reaction, followed by the fast electrochemical oxidation of adsorbed hydrogen atoms, known as the Volmer reaction [106].

$$H_2 + 2Pt \rightleftharpoons 2(H - Pt) \tag{2.23}$$

$$2(H - Pt) \rightleftharpoons 2Pt + 2H^+ + 2e^- \tag{2.24}$$

However, in the polymer electrolyte membrane, the hydrogen ions exist as hydronium (H_3O+) ions [67], thus the hydrogen electro-oxidation reaction can be expressed as:

$$H_2 + 2Pt \rightleftharpoons 2(H - Pt) \tag{2.25}$$

$$2(H - Pt) + H_2O \rightleftharpoons 2Pt + 2H_3O^+ + 2e^- \tag{2.26}$$

The H^+ ions have been replaced by H_3O^+ ions, and water is now required on the left hand side of the Volmer step. This representation of the electro-oxidation of hydrogen in a PEM fuel cell explicitly shows the need for proper humidification. Without water proton transport would be impossible and the electron transfer step

could not proceed.

The adsorption and desorption of hydrogen are assumed to follow the Langmuir kinetics [111]. Electro-oxidation of hydrogen are assumed to follow the Volmer/Erdey-Gruz kinetics, with the anodic and cathodic transfer coefficients being equal [111]. As a result, the reaction rates of the anode catalyst reactions, in mole/(m^2.s), are:

$$q_H^{a,\text{ads}} = k_H^{\text{ads}} c_{H_2} (\theta_M)^2 - b_H^{\text{ads}} k_H^{\text{ads}} (\theta_H)^2 \tag{2.27}$$

$$q_H^{a,\text{ox}} = 2k_H^{\text{ox}} \theta_H \text{sinh}\left(\frac{2\alpha_0 \mathcal{F}}{RT}\right) \eta_{\text{ox}} \tag{2.28}$$

where k_i and b_i denotes the reaction rate constants of species i (H). θ_i is the fraction of the platinum reaction sites in the solid phase covered by species i and $\theta_M = 1 - \theta_H$ represents the fraction of free reaction sites. $q_H^{a,\text{ads}}$ and $q_H^{a,\text{ox}}$ represent the adsorption and electro-oxidation rates per mole of hydrogen atoms. α_a is the anodic transfer coefficient, $\mathcal{F}$ is Faraday's constant, R the universal gas constant, $T(K)$ is temperature and η_{act} is the activation overpotential, defined by:

$$\eta_{\text{act}} = \phi_{\text{ele}} - \phi_{\text{pro}} \tag{2.29}$$

where ϕ_{ele} and ϕ_{pro} are the electronic and ionic potentials respectively. The activation overpotential η_{act} is the voltage loss in order to activate the electrochemical reaction. If the same amount of current is drawn, then a higher activation loss indicates that the electrochemical reaction is more sluggish. The constants k_i and b_i are temperature dependent and are represented by the Arrhenius equations:

$$k_i = k_i^o \text{exp}\left(-\frac{E_i^k}{RT}\right) \tag{2.30}$$

$$b_i = b_i^o \text{exp}\left(-\frac{E_i^b}{RT}\right) \tag{2.31}$$

where k_i^o and b_i^o are pre-exponential factors of species i, and E_i^k and E_i^b are the activation energies.

Cathode Reaction Kinetics

The major reaction at the cathode catalyst layer is the reduction of oxygen:

$$O_2 + 4H^+ + 4e^- \rightleftharpoons 2H_2O \tag{2.32}$$

The reaction mechanism of the oxygen reduction reaction at the cathode catalyst layer follows a complex route. In this research the route is simplified so that the chemical reaction and reaction rate is presented in a similar manner as in the anode catalyst layer:

$$O_2 + 2Pt \rightleftharpoons 2(O - Pt) \tag{2.33}$$

$$2(O - Pt) + 4H^+ + 4e^- \rightleftharpoons 2H_2O + 2Pt \tag{2.34}$$

and the reaction rate is:

$$q_O^{c,\text{ads}} = k_O^{\text{ads}} c_{O_2} (\theta_M)^2 - b_O^{\text{ads}} k_O^{\text{ads}} (\theta_O)^2 \tag{2.35}$$

The electron transfer activity at the equilibrium potential, ϕ_r, are also referred to as the exchange current density, J_0, and can be expressed in terms of concentration of reactants [56]:

$$J_O = J_O^{\text{ref}} \left(\frac{C_i}{C_i^{\text{ref}}} \right)^{\gamma_i} \tag{2.36}$$

where γ is the reaction order with respect to reactant i, C_i is the concentration of reactant i, and C^{ref} is the reference concentration, usually the saturation concentration at 1 atmosphere.

The local current density, J, is given by the Butler-Volmer equation as [81]:

$$J = J_0 \left[\exp\left(\frac{\alpha n F \eta}{RT}\right) - \exp\left(-\frac{(1-\alpha)\, nF\eta}{RT}\right)\right] \tag{2.37}$$

The volumetric current density, $\mathcal{R}_i$, can be expressed as:

$$\begin{aligned} \mathcal{R}_i &= A_v i & (2.38)\\ &= A_v i_O^{\text{ref}} \left(\frac{C_i}{C_i^{\text{ref}}}\right)^{\gamma_i} \left[exp\left(\frac{\alpha n F \eta}{RT}\right) - \exp\left(-\frac{(1-\alpha)\, nF\eta}{RT}\right)\right] & (2.39) \end{aligned}$$

where A_v is the reactive surface density, defined as the ratio of the total active catalyst surface to the total catalyst region volume; α is a transfer coefficient; F is Faraday's constant; R is the universal gas constant; T the temperature and η is the activation potential.

Thus, for both the anode and cathode catalyst layers, we can express the volumetric current densities as:

$$\begin{aligned} \mathcal{R}_a &= A_v i_{O,a}^{\text{ref}} \left(\frac{C_{H_2}}{C_{O,H_2}^{\text{ref}}}\right)^{\gamma_{H_2}} \left[\exp\left(\frac{\alpha n F \eta_a}{RT}\right) - \exp\left(-\frac{(1-\alpha)\, nF\eta_a}{RT}\right)\right] & (2.40)\\ \mathcal{R}_c &= A_v i_{O,c}^{\text{ref}} \left(\frac{C_{O_2}}{C_{O,O_2}^{\text{ref}}}\right)^{\gamma_{O_2}} \left[\exp\left(\frac{\alpha n F \eta_c}{RT}\right) - \exp\left(-\frac{(1-\alpha)\, nF\eta_c}{RT}\right)\right] & (2.41) \end{aligned}$$

From the reactions (equations 1.1 to 1.3), it is known that for each mole of electron draw from the electrochemical reaction, 1/2 mole of hydrogen and 1/4 mole of oxygen are consumed. Therefore, once the volumetric current flow is known, the reaction rate of hydrogen and oxygen can be easily determined as

$$S_{H_2} = -\frac{1}{2\mathcal{F}} \mathcal{R}_a \tag{2.42}$$

$$S_{O_2} = -\frac{1}{4\mathcal{F}}\mathcal{R}_c \tag{2.43}$$

Equations 2.39 and 2.40 are valid in the catalyst layers since the electrochemical reaction occurs in the catalyst layer only. In all other regions, the source/sink of the hydrogen and oxygen are simply zero.

2.3 Transport of Energy

There are normally not very large temperature variations in PEM fuel cells. Therefore, heat transfer processes are usually simplified to some extend to reduce the model complexity. Based on the analysis of [66], it is assumed that the gas phase and solid phase are always in a thermal equilibrium state.
As such, the energy equation that accounts for the effect of multi-species flow in the porous medium can be stated as [34].

$$\nabla \cdot (\sum_{k=g,s} \rho E)_k + \nabla \cdot \vec{u}_g(\rho_g E_g + P_g) = \nabla \cdot [k^{\text{eff}} \nabla T - (\sum_i h_i \vec{N_i}) + (\tau \cdot \vec{u}_g)] + S_T \tag{2.44}$$

where k^{eff} is the effective conductivity, and N_i is the diffusion flux of species i. The first three terms on the right hand side of Equation (2.41) represent energy transfer due to conduction, species diffusion, and viscous dissipation, respectively. S_T includes the heat of chemical reaction, and any other volumetric heat sources.

In Equation (2.41), E denotes the total energy in the respective phase and it is calculated as

$$E = h - \frac{P}{\rho} + \frac{\vec{u}_g^2}{2} \tag{2.45}$$

where the sensible enthalpy h is defined for ideal gases as

$$h = \sum_i Y_i h_i \tag{2.46}$$

with Y_i the mass fraction of species i

$$Y_i = X_i \left(\frac{M_i}{\sum_i X_i M_i} \right) \tag{2.47}$$

and

$$h_i = \int_{T^{\text{ref}}}^{T} c_{p,i} dT \tag{2.48}$$

where T^{ref} is 298,15 K and $c_{p,i}$ is the specific heat of the ith species.

Similarly, the sensible enthalpy for the solid phase is determined by

$$h = \int_{T^{ref}}^{T} c_p dT \tag{2.49}$$

where c_p is the specific heat of the solid material. The effective thermal conductivity, k^{eff}, is evaluated based on the volume fraction of each phase as

$$k^{eff} = \varepsilon k_g (1 - \varepsilon) k_s \tag{2.50}$$

The thermal conductivity of the solid phase can be specified directly, while the thermal conductivity of the gas mixture is calculated based on kinetic theory

$$k_g = \sum_i \frac{X_i k_i}{\sum_j X_j \phi_{ij}} \tag{2.51}$$

where

$$\phi_{ij} = \frac{[1 + (\frac{\mu_i}{\mu_j})^{\frac{1}{2}} (\frac{M_j}{M_i})^{\frac{1}{4}}]^2}{[8(1 + (\frac{M_i}{M_j})]^{\frac{1}{2}}} \tag{2.52}$$

Moreover, the diffusion flux of species in Equation (2.41) is estimated using Ficks law as mentioned earlier in Section 2.2

$$\vec{N}_i = -D_{i,m}^{\text{eff}} \nabla C_i \tag{2.53}$$

The last term in Equation (2.41) represents the heat source. Four kinds of heat sources were considered in the current model. They are the reversible heat release during the electrochemical reaction, irreversible (activation) heat generation, ohmic heating, and the latent heat during membrane water sorption/desorption, respectively. Thus,

$$S_T = S_{T,\text{rev}} + S_{T,\text{act}} + S_{T,\text{ohm}} + S_{T,\text{sor/des}} \tag{2.54}$$

In the cathode catalyst layer, all four types of heat generation are present and the heat source has the form

$$S_T = \left| \frac{\mathcal{R}_\lrcorner}{4\mathcal{F}} \right| (T\Delta S) + \left| \eta_c \mathcal{R}_\lrcorner \right| + \frac{J_s^2}{\sigma_s} + \frac{J_m^2}{\sigma_m} + M_w S_{vd}(h_{m,fg} - h_{fg}) \tag{2.55}$$

where S represents the entropy change of the oxidation reduction reaction, and $h_{m,fg}$ represents the latent heat of water vapor sorption. Similarly, the heat source in the anode catalyst layer is

$$S_T = |\eta_a \mathcal{R}_\dashv| + \frac{J_s^2}{\sigma_s} + \frac{J_m^2}{\sigma_m} + M_w S_{vd} h_{m,fg} \tag{2.56}$$

The reaction heat during the hydrogen oxidation reaction is very small and has been neglected from the above equation. Furthermore, water sorption from water vapor to dissolved water in the anode catalyst layer, and desorption from dissolved water to water vapor in the cathode catalyst layer, have been assumed here.

Water vapor sorption into a membrane is a process similar to a vapor condensation process and involves a release of heat (exothermic). Similarly, water molecules leaving a membrane as vapor is similar to a liquid evaporation process and requires heat (endothermic).

In the gas diffusion layer, only ohmic heating is present. Therefore, the heat source is

$$S_T = \frac{J_s^2}{\sigma_s} \tag{2.57}$$

In the membrane layer, the heat source only includes the ohmic heating caused by protonic current flow

$$S_T = \frac{J_m^2}{\sigma_m} \tag{2.58}$$

In the gas flow channels, the heat sources are simply zero.

2.4 Transport of Electric Charge

The electrolyte consists of the ion-selective membrane and the transport of charge is considered in this section. Also, included in this model are the cell potentials which are determined at the electrode-electrolyte boundaries.

As illustrated in Section 1.2, hydrogen molecules are stripped of their electrons and become positively charged hydrogen ions (protons) during the hydrogen oxidation reaction. Protons migrate through the ion-selective membrane directly and reach the cathode side catalyst layer, while electrons are expelled by the membrane and have to travel through the solid part of the backing layer and external circuit to reach the cathode catalyst, where they recombine with protons to form water following the oxygen reduction reaction.

2.4.1 Conservation of Electronic Charge

The governing equation for electronic transport can be written as:

$$\nabla \cdot (\vec{J_s}) = S_\phi \tag{2.59}$$

where S_ϕ is the source term denoting the generation or consumption of electrons, and $\vec{J}_s$ is the electronic charge density through the solid. The current density is a vector quantity, and only the transverse component (normal to the gas diffusion layer surface) is useful and contributes to the power output of the cell; the lateral component only decreases the cell output. Therefore, the lateral component should be minimized through appropriate designs. Electronic charge density is related to electric potential in terms of Ohm's Law:

$$\vec{J}_s = -\sigma_s \nabla \phi_s \tag{2.60}$$

where ϕ_s is the electric potential in the solid phase; σ_s is the electric conductivity of the solid material. Thus:

$$\nabla \cdot (-\sigma_s \nabla \phi_s) = S_\phi \tag{2.61}$$

In the anode catalyst layer, electrons are generated, thus

$$S_\phi = \mathcal{R}_a \tag{2.62}$$

and in the cathode catalyst layer electrons are consumed, so

$$S_\phi = -\mathcal{R}_c \tag{2.63}$$

In other regions, no electrochemical reaction occurs and hence

$$S_\phi = 0 \tag{2.64}$$

2.4.2 Conservation of Protonic Charge

The transport of protons (H^+) through the ion-selective membrane is governed by:

$$\nabla \cdot (\vec{J}_m) = S_\phi \tag{2.65}$$

where $\vec{J}_m$ is the protonic charge density which lies within the electrolyte membrane only, and according to Ohm's Law:

$$\vec{J}_m = \sigma_m \nabla \phi_m \tag{2.66}$$

where ϕ_m is the electric potential in the electrolyte membrane, and σ_m the electric conductivity of the membrane which is affected by the local membrane water content through an empirical correlation [70]

$$\sigma_m = \varepsilon_m (0.005139\lambda - 0.00326) \exp\left[1268\left(\frac{1}{303} - \frac{1}{T}\right)\right] \tag{2.67}$$

Consequently, Equation (2.63) is converted to

$$\nabla \cdot (\sigma_m \nabla \phi_m) = S_\phi \tag{2.68}$$

Corresponding to the electron transport, the amount of proton gain or loss must equal that of the electron. Therefore, in the anode catalyst layer, the source term for proton transport is

$$S_\phi = \mathcal{R}_a \tag{2.69}$$

and in the cathode catalyst layer electrons are consumed, so

$$S_\phi = \mathcal{R}_c \tag{2.70}$$

In other regions, no electrochemical reaction occurs and hence

$$S_\phi = 0 \tag{2.71}$$

2.5 Boundary Conditions

In order to complete the model formulation, boundary conditions at different locations of the cell domain are required. A single computational domain approach is employed in this study, thus boundary conditions are only needed to be specified on the outer surfaces of the domain.

The boundary conditions represent the real operating conditions of a high temperature PEM fuel cell. When testing a high temperature PEM fuel cell, several operating conditions can be varied, such as:

- the flow rate of the reactants;
- the purity (concentration) of the reactants;
- the relative humidity of the reactants flow;
- the operating temperature;
- the operating pressure and
- the electrical load.

The boundary conditions present in the single channel serpentine PEMFC are the flow inlets represented by B_{in}, the pressure outlets, represented by B_{out}, wall, represented by B_w and zero flux, represented by B_f, boundary conditions respectively.

At the gas flow channel inlets (B^a_{in} and B^c_{in}), the gas composition, mass flux (denoted by $\dot{m}''$), and temperature of the incoming gas flow are specified and the fluxes of all other variables (denoted by Θ) are set to zero.

$$\dot{m}'' \cdot \vec{n} = \text{Specified} \tag{2.72}$$

$$C_i = \text{Specified} \tag{2.73}$$

$$T = \text{Specified} \tag{2.74}$$

$$\frac{\partial \Theta}{\partial \vec{n}} = 0 \tag{2.75}$$

The mass fluxes of gas species are given by their respective stoichiometric ratios, ξ_a and ξ_c and reference current density, $J^{\text{ref}} = 1$ A/cm^2 , as

$$\dot{m}_a'' = \frac{\rho_g \xi_a J^{\text{ref}} A}{2\mathcal{F} C_{H_2}} \tag{2.76}$$

$$\dot{m}_c'' = \frac{\rho_g \xi_c J^{\text{ref}} A}{4\mathcal{F} C_{H_2}} \tag{2.77}$$

$$\tag{2.78}$$

where A is the active reaction surface.

The inlet concentrations of hydrogen, C_{H_2} , and oxygen, C_{O_2} , can be obtained through the following relations

$$C_{H_2} = \frac{(P_a - RH_a P^{\text{sat}})}{RT_0} \tag{2.79}$$

$$C_{O_2} = 0.21 \frac{(P_c - RH_c P^{\text{sat}})}{RT_0} \tag{2.80}$$

$$\tag{2.81}$$

where T_0 is the inlet gas temperature, P_a and P_c are the inlet gas pressure at anode and cathode, respectively, RH_a and RH_c are the inlet relative humidities of anode and cathode, respectively. The coefficient 0.21 represents the molar fraction of O_2 in air.

At the gas flow channel outlets (B_a and B_c), the flow is assumed to be fully developed. Thus, the fluxes of all variables do not vary in the normal direction. Moreover, the gas pressure is specified.

$$P = \text{Specified} \tag{2.82}$$

$$\frac{\partial \Theta}{\partial \vec{n}} = 0 \tag{2.83}$$

At the channel walls ($B^a_{w,ch}$ and $B^c_{w,ch}$), a constant operating temperature is prescribed. In addition, no-slip boundary conditions apply, along with zero flux conditions for other variables.

$$\vec{u}_g = 0 \tag{2.84}$$

$$T = \text{Specified} \tag{2.85}$$

$$\frac{\partial \Theta}{\partial \vec{n}} = 0 \tag{2.86}$$

Similarly, the operating temperature and electronic potential are directly defined at the GDL surfaces that are exposed to the bipolar plate ($B^a_{w,gdl}$ and $B^c_{w,gdl}$).

The specification of the boundary conditions for the electronic potential at the surfaces of the anode and cathode that are exposed to the bipolar plate are as follow:

- the electronic potential at the upper surface of the anode is set at $\phi_{s,a} = 0$ for convenience,

- then the electronic potential at the cathode bottom surface equals the cell output voltage, i.e. $\phi_{s,c} = \phi_{\text{cell}}$.

- The overpotential in the anode catalyst layer is the difference between the solid phase and membrane phase potentials, $\eta_a = \phi_s \phi_m$,

- while the over-potential at the Cathode catalyst layer is calculated as $\eta_c = \phi_s \phi_m \phi_{\text{rev}}$, where ϕ_{rev} is the theoretical reversible cell potential.

- It is calculated from the modified form of the Nernst equation by assuming that the overall cell reaction is at thermodynamic equilibrium [137]

$$\phi_{\text{rev}} = \frac{\Delta G^{\text{ref}}}{2\mathcal{F}} - \frac{\Delta S^{\text{ref}}}{2\mathcal{F}}(T - T^{\text{ref}}) - \frac{RT}{2\mathcal{F}} \ell \text{n} \left[\left(\frac{P_{H_2}}{P^{\text{ref}}} \right) \left(\frac{P_{O_2}}{P^{\text{ref}}} \right)^{\frac{1}{2}} \right] \tag{2.87}$$

Here, G^{ref} is the Gibbs free energy change and S^{ref} the entropy change for the overall reaction at reference temperature, T^{ref} , and pressure P^{ref} . P_{H_2} and P_{O_2} are the partial pressure of hydrogen and oxygen, respectively.

Thus, the set of boundary conditions for the wall between the anode and cathode solid and the gas diffusion layers are:

$$\vec{u}_g = 0 \tag{2.88}$$

$$T = \text{Specified} \tag{2.89}$$

$$\phi_s = \text{Specified} \tag{2.90}$$

$$\frac{\partial \Theta}{\partial \vec{n}} = 0 \tag{2.91}$$

For the remaining boundaries, a no-flux condition or symmetry condition applies

$$\frac{\partial \Theta}{\partial \vec{n}} = 0 \tag{2.92}$$

2.6 Model Input Parameters

In addition to boundary conditions, the mathematical model is also constrained by various parameters. The input parameters of the current model can be roughly grouped into four kinds: the structural parameters, the electrochemical kinetic parameters, the physical and thermal parameters, and the operating parameters.

The structural parameters of the current model are listed in Table 2.1. The anode and cathode layers are identical; hence, the same parameters apply to the gas flow channels, GDL and catalyst layers on the anode and cathode sides. The geometric parameters of the gas channel are design parameters and, thus, they represent the real experimental conditions, while the parameters in the porous region are highly dependent on the chosen types of porous material (e.g., carbon paper, carbon cloth), the fabrication processes (loading of PTFE, Nafion, Pt, etc.),and the assembling processes (e.g, compression pressure). It is extremely hard, if not impossible, to measure the material properties in an assembled fuel cell. Therefore, these parameters are usually estimated, based on empirical expressions. Structural parameters are thus not dependent on fuel cell operating conditions and are applied equally for low temperature fuel cell research and high temperature fuel cell research. The dependence of the cell performance on these estimated parameters can be evaluated through parametric studies.

The electrochemical kinetic parameters are experimentally determined at reference conditions. In this study, the values measured by Springer et al. [70] and Bernardi et al. [81] are used. The applicability of some low temperature kinetic parameters in the study of high temperature fuel cells was successfully researched and published by researchers such as Cheddie and Munroe [44, 43] and [79]. However, for the specific fluid properties of oxygen, hydrogen and water which can vary with temperature and pressure variations the parameters listed in the reference books of [4] and [102], applicable for temperatures higher that 400 K, are used. They are

listed in Table 2.2.

In Table 2.3, the physical and thermal properties that are encountered in the mathematical model are summarized. These parameters can be easily found in common thermodynamic books and/or come with the commercialized materials in the specification sheets.

Again, these properties are applicable to both low and high temperature fuel cell materials and reacting species.

In addition, there are some variable parameters that are relevant to the cell operating condition, such as the operating pressure, temperature, gas flow rate, and relative humidity, etc. They are pertaining to a specific case study and, hence, will be provided in Chapter 4 along with the modeling results.

2.6.1 Structural Parameters

Parameter	Symbol	Value
Structural [116], [117], [119]		
Gas channel width, (mm)		1.0
Gas channel height, (mm)		1.0
Gas channel length, (mm)		50.0
Land width between adjacent channels, (mm)		1.0
Thickness of Cl, (μm)	δ_{Cl}	10
Thickness of gdl, (μm)	δ_{gdl}	200
Thickness of membrane, (μm)	δ_{mem}	50
Porosity of Cl	ε_{Cl}	0.3
Porosity of gdl	ε_{gdl}	0.6
Volume fraction of membrane in Cl	ε_m	30 ٪
Pore surface area per unit volume, (μm)	$\bar{d}$	30
Contact area of porous material, (^{0}), [120]	θ_c	110

Table 2.1: Structural Parameters

2.6.2 Electrochemical Kinetic Parameters

Parameter	Symbol	Value
Electrochemical [81], [70]		
Reference anode exchange current density, (A.m^{-3}), [4],	$aj_{0,a}^{\text{ref}}$	5×10^8
Reference cathode exchange current density, (A.m^{-3}), [4],	$aj_{0,c}^{\text{ref}}$	1.2×10^2
Reference hydrogen concentration, (mol.m^{-3}), [102],	C_{0,H_2}	56.4
Reference oxygen concentration, (mol.m^{-3}), [102],	C_{0,O_2}	3.39
Anodic transfer coefficient	α_a	0.5
Cathodic transfer coefficient	α_c	0.5
Anodic reaction order	β_a	0.5
Cathodic reaction order	β_c	1.0
Electrode (graphite) [28]		

Table 2.2: Electrochemical Kinetic Parameters

2.6.3 Physical and Thermal Parameters

Parameter	**Symbol**	**Value**
Physical and Thermal [81], [118], [114]		
Hydrogen diffusivity in water vapor, ($m^2.s^{-1}$)	$\mathcal{D}_{H_2-H_2O(g)}$	9.15×10^{-5}
Oxygen diffusivity in water vapor, ($m^2.s^{-1}$)	$\mathcal{D}_{O_2-H_2O(g)}$	2.82×10^{-5}
Oxygen diffusivity in nitrogen, ($m^2.s^{-1}$)	$\mathcal{D}_{O_2-N_2}$	2.2×10^{-5}
Water vapor diffusivity in nitrogen, ($m^2.s^{-1}$)	$\mathcal{D}_{H_2)-N_2}$	2.5×10^{-5}
Electrode conductivity, ($S.m^{-1}$),	σ_s	7.5×10^2
Density of electrode, (kg. m^{-3})	$\rho_{gdl;Cl}$	2.2×10^3
Density of membrane (Nafion), (kg. m^{-3})	ρ_m	1.98×10^3
Density of hydrogen, (kg. m^{-3})	ρ_{H_2}	6.9×10^{-2}
Density of air, (kg. m^{-3})	ρ_{air}	0.995
Density of water vapor, (kg. m^{-3})	ρ_v	0.632
Specific heat of electrode, ($J.kg^{-1}.K$)	$c_{p,gdl}$	1.05×10^3
Specific heat of hydrogen, ($J.kg^{-1}.K$)	c_{p,H_2}	1.44×10^4
Specific heat of air, ($J.kg^{-1}.K$)	$c_{p,air}$	1.01×10^3
Specific heat of water vapor, ($J.kg^{-1}.K$)	$c_{p,v}$	1.96×10^3
Thermal conductivity of GDL, ($W.m^{-1}.K$)	k_{gdl}	$k_x = k_z = 10; k_y = 1.3$
Thermal conductivity of Cl, ($W.m^{-1}.K$)	k_{Cl}	0.8725
Thermal conductivity of membrane, ($W.m^{-1}.K$)	k_m	0.445
Thermal conductivity of air, ($W.m^{-1}.K$)	k_{air}	0.03
Thermal conductivity of water vapor, ($W.m^{-1}.K$)	k_v	0.023
Thermal conductivity of hydrogen, ($W.m^{-1}.K$)	k_v	0.204
Condensation/evaporation latent heat, ($J.kg^{-1}$)	h_{fg}	2.308×10^6
Standard Entropy change, ($J.mol^{-1}$), [19]	ΔS^{ref}	-44.42
Entropy change at working conditions, ($J.mol^{-1}$), [19]	S	-43.207
Standard Gibbs free energy change, ($J.mol^{-1}$), [19]	ΔG^{ref}	2.29×10^5

Table 2.3: Physical and Thermal Parameters

2.6.4 Summary of Source Terms

There are five source terms S_m, S_u, S_i, S_ϕ and S_T, which represents various volumetric sources or sinks arising from each sub-region of a fuel cell. It shows either the generation or consumption of gas species i.

SourceTerms	$\mathbf{S_m}$	$\mathbf{S_u}$	$\mathbf{S_i}$	$\mathbf{S}_\phi$	$\mathbf{S_T}$
Channel	0	0	0	0	0
Electrode	0	$-\frac{\mu_g}{\kappa_{gdl}}\vec{u}_g$	0	0	$\frac{J^2}{\sigma_s}$
AnodeCl	S_{H_2}	$-\frac{\mu_g}{\kappa_{Cl}}$	$S_{H_2} = -\frac{\mathcal{R}_a}{2F} - S_{vd}$	$\mathcal{R}_a$	$\lvert\eta_a \mathcal{R}_\dashv\rvert + \frac{J_s^2}{\sigma_s} + \frac{J_m^2}{\sigma_m} + M_w S_{vd} h_{m,fg}$
CathodeCl	S_{O_2}	$-\frac{\mu_g}{\kappa_{Cl}}$	$S_{O_2} = -\frac{\mathcal{R}_c}{4F}$ $S_{H_2O} = \frac{\mathcal{R}_c}{2F}$	$\mathcal{R}_c$	$\left\lvert\frac{\mathcal{R}_\mathcal{C}}{4\mathcal{F}}\right\rvert (T\Delta S) + \lvert\eta_c \mathcal{R}_\mathcal{C}\rvert + \frac{J_s^2}{\sigma_s} + \frac{J_m^2}{\sigma_m} + M_w S_{vd}(h_{m,fg} - h_{fg})$
Membrane	0	0	0	0	$\frac{J_m^2}{\sigma_m}$

Chapter 3

Numerical Formulation

In this Chapter the numerical procedure and code for the simulation of the mathematical model described in Chapter 2 is presented. All numerical simulations are performed using the pressure based solver of FLUENT. The equation variables for each individual governing equation are solved sequentially. Each governing equation, while being solved is decoupled or segregated from the other equations. It is based on the finite-volume numerics on any 3-dimensional mesh of polyhedral cells.

A short overview of the mathematical problem and the numerical approach is provided in section 1. In section 2 the discretization procedure used to decompose the solution domain is presented. In section 3 the procedure to decompose the set of partial differential equations that describe the mathematical model into a set of algebraic expressions is described. In sections 4, the numerical algorithms to solve the mathematical model in each space sub-domain, and the exchange of information between adjacent sub-domains are presented.

3.1 Overview of Numerical Solution Procedure

The mathematical model developed in Chapter 2 consists of differential equations for the mass, momentum, species and energy conservation for the various flow do-

mains in the high temperature polymer electrode fuel cell. A number of constitutive equations were added to describe the thermo-physical and transport coefficients of the different species. The direct analytical solution to the entire equation set is presently impossible due to the highly non-linear and coupled nature of the system. Thus, a computer-based numerical solution is used.

The finite volume based commercial software, Ansys FLUENT 15.0, is employed to do the numerical simulation of the model. The pre-processing component of FLUENT, Ansys ICEM CFD, is used to construct a structured, non-uniform, cartesian grid scheme, which is imported into the simulation component of FLUENT where the complete governing equation set (2.1, 2.2, 2.9, 2.12, 2.13, 2.41) is discretized and solved. In addition, FLUENT has built-in modules for the non-standard governing equations for charge, electronic potential, protonic potential and dissolved water concentration. Moreover, various source terms, model parameters, empirical correlations are imported as defined scalar equations. In addition some controlling strategies and under-relaxation schemes are constructed for the model.
The pressure-based segregated solver of FLUENT was chosen for this research because of its convergency and computational speed. By using the segregated solver the individual governing equations are solved for the given variables (e.g. u, v, w, p, C_{H_2}, C_{O_2}, C_{H_2O}, ϕ_s, ϕ_m,T etc) sequentially.

The numerical solution procedure in this research is described in three sections. In Section 3.2 the discretization of the solution domain is discussed. This involves subdividing the three-dimensional solution domain into a number of polyhedral cells or control volumes over which each of the governing equations is integrated. Also, the discretization of the governing equations into a set of linear algebraic equations that are then solved with an appropriate solver, is discussed in section 3.3. The algorithm that describes the numerical solution is discussed in Section 3.4. It is structured to maintain the coupling between equations and impose continuity and

boundedness constraints on the system as a whole.

The governing equations are nonlinear and coupled to one another, thus the solution loop must be carried out iteratively in order to obtain a converged numerical solution. The loop that solves the governing equations is usually referred to as the outer loop. The solution of the individual equations also involves iterations and is usually referred to as the inner loop.

3.2 Discretization of the Solution Domain

Discretization of the space (solution) domain requires the subdivision of the domain into a number of cells, or control volumes. The resultant domain with its subdivided structure is called the numerical mesh of the domain. In FLUENT this subdivision is done by a pre-processing tool called ICEM [34]. For the numerical mesh to be compatible with FLUENT, the following requirements are needed:

(a) each control volume is a polyhedron bounded by a set of flat faces, f. In this study, for example, the control volumes are cubes, bounded by six flat faces, as in figure 3.1. (b) the control volumes are contiguous i.e. they do not overlap with one another, and form the computational domain. (c) the control volumes either connect two cells, or belong to the boundary. (d) the coordinate system is the right-handed Cartesian system.

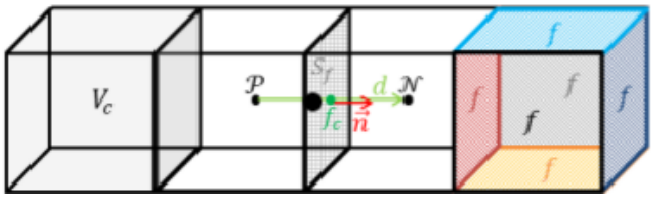

Figure 3.1: Two Adjacent Control Volumes after Space Discretization, from M. Camprubi [23]

The cartesian grid method of Ansys ICEM CFD was used to mesh the solution domain. This method provides the freedom to specify the number of nodes (grid

points) for each of the x, y and z directions i.e. $N_x; N_y$ and N_z can be specified. The solution domain is then divided into hexahedral cells or control volumes and the governing equations are applied to each. At the centroid of each control volume lies a node at which the variable values are calculated. Interpolation is used to express variable values at the control volume surface in terms of nodal values.
Theoretically, an exact solution is obtained when the grid size is infinitely small. In practice, it is desirable to limit the number of grid points to as few as possible to reduce computational expense. To achieve a feasible balance a grid study is performed to try an attain the minimum number of grid points that will produce a solution that will stay constant even if the the mesh size increases.

In the numerical tests conducted in this study, the first coarse mesh had $N_x = 20$; $N_z = 50$ fixed, and $N_y = 45$. This correspond to mesh elements with a size equal to the width of the flow channels in the x-direction and the length between the ends of the bipolar plate solids and the channels in the z-direction. In the y-direction each cell component i.e. bipolar plates, gas diffusion layer, catalyst layer and membrane was apportioned 5 mesh cell layers each. The total number of computational cells, N_{total} , are calculated as

$$N_{total} = N_x N_y N_z \tag{3.1}$$

Testing was done in three steps. During each step the number of grid points in two directions (x and z) was kept constant, while the number of points in the y-direction was varied. An example of the step 1 trial is

Case:	1	2	3	4	5	6	7	8
$\mathbf{N_y}$:	18	27	36	45	54	63	72	80

Table 3.1: Grid independent study in the y-direction
with $N_x = 20$ and $N_z = 50$

It was found that the grid scheme starts to converge for the x and z direction

pair at $x = 40$ and $z = 100$, while the through-plane direction (y-direction), the solution variables change significantly, since the length scales in that direction are much smaller than the other two directions for most of the cell regions. Also, it is found that the model quickly diverges when N_y is below or equal to 27 (i.e three cell layers per cell component) since the discretization error becomes too large and the solution is very likely oscillating and diverging. On the other hand, it also fails to achieve a converged solution when beyond 45. This is probably due to the increasingly high grid aspect ratio which tends to impair the stability of the system. therefore, $N_y = 45$ has been referred to as the exact solution and the relative errors induced in other cases are defined accordingly as

$$\mathrm{Err}_y = \left| \frac{\Phi_{45} = \Phi_y}{\Phi_{45}} \right| \times 100 \tag{3.2}$$

where Φ represents the variable to be compared.

In the second and third steps, the values of N_x and N_z for a grid independent solution are determined in a similar manner as in the first step, thus the procedures are not repeated here. Generally speaking, the model is much less sensitive to the grid numbers in the x and z directions and relatively coarse uniform grid schemes with $N_x = 40$ and $N_z = 100$ are found to be sufficient in these directions. The solution error in the y-direction is found to be 1.88. The corresponding solution errors in the x and z directions are $\mathrm{Err}_x = 0.49$ and $\mathrm{Err}_z = 0.009$, respectively

$$\mathrm{Err} \leq \sqrt{|\mathrm{Err}_x|^2 + |\mathrm{Err}_y|^2 + |\mathrm{Err}_z|^2} = 1.94 \tag{3.3}$$

Now, the total number of control volumes for a single channel geometry can be calculated

$$N_{\mathrm{total}} = 40 \times 45 \times 100 = 180000 \tag{3.4}$$

The final mesh for the single serpentine channel PEM fuel cell appears in the figure below:

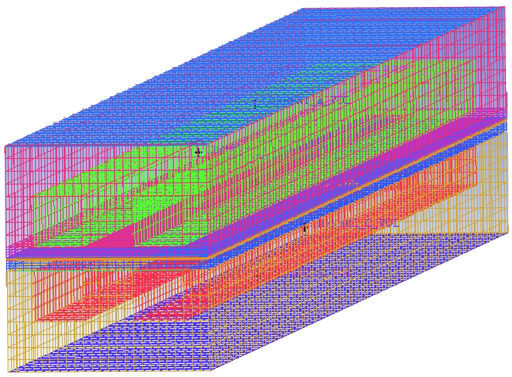

Figure 3.2: Single serpentine channel fuel cell mesh

The mesh for the different components of the fuel cell is given in figures 3.3 to 3.7 below:

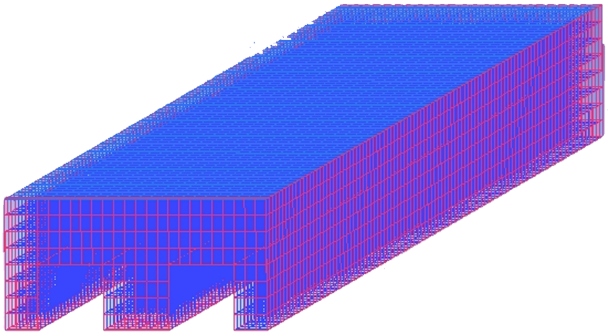

Figure 3.3: Anode Current Collector Mesh

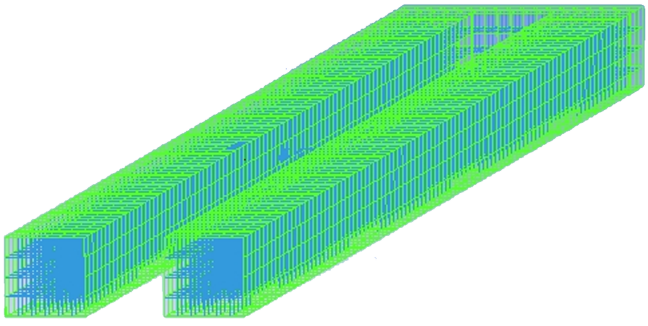

Figure 3.4: Anode Gas Channel Mesh

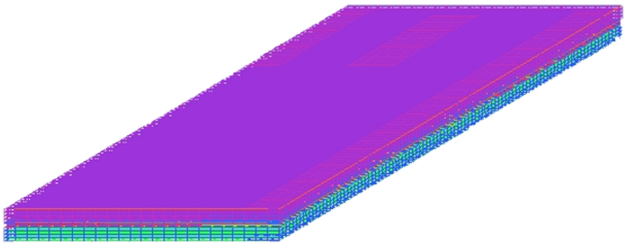

Figure 3.5: MEA Mesh

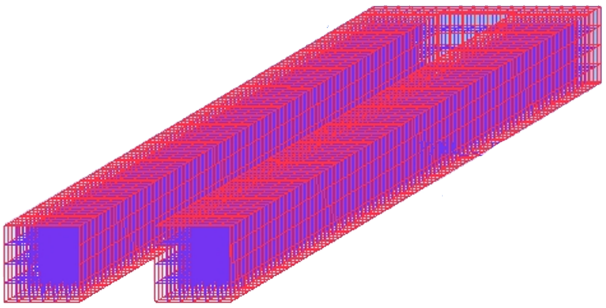

Figure 3.6: Cathode Gas Channel Mesh

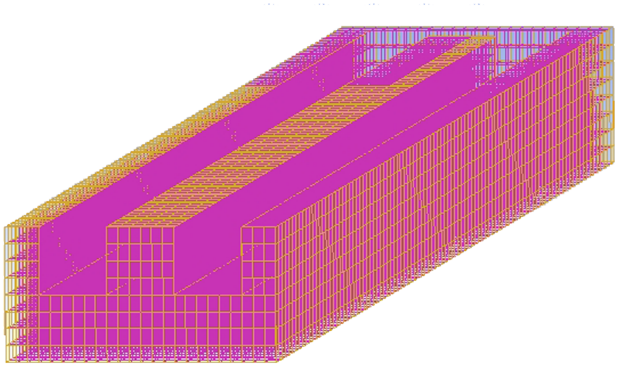

Figure 3.7: Anode Current Collector Mesh

3.3 Discretization of the Governing Differential Equations

Once the solution domain has been defined, the governing equations are discretized by integrating them over each cell applying Gauss' theorem, which translates the volume integral into a surface integral. The values of the primitive variables on the

cell faces are then re-written in terms of neighboring cell centre values, yielding an algebraic equation for that cell. The result is a set of algebraic equations, one for each discretized equation, written in terms of the mesh cell centre values.

This procedure is well defined and its application to the equations comprising the present fuel cell model is straight forward. To aid the process, the equations are first written in a generic form by grouping the individual terms into convective, diffusion and source terms. The discretization for each group of terms is the same for all equations.

For the system under consideration, the generic form of the steady-state partial differential equation, for any scalar or vector quantity, ϕ is written as:

$$\nabla \cdot (\rho \vec{u} \phi) - \nabla \cdot (\Gamma \nabla \phi) = S_\phi \tag{3.5}$$

where $\nabla \cdot (\rho \vec{u} \phi)$ is the convection term; $\nabla \cdot (\Gamma_\phi \nabla \phi)$ the diffusion term, and S_ϕ represents the source terms which may include additional fluxes or stress components. Also, ρ is the phase density, $\vec{u}$ the phase velocity, Γ_ϕ is the diffusion coefficient. Integrating equation 3.5 over each control volume, V_c, yields:

$$\int_{V_c} \nabla \cdot (\rho \vec{u} \phi) dV_c + \int_{V_c} \nabla \cdot (\Gamma_\phi \nabla_\phi \phi) dV_c = \int_{V_c} S_\phi dV_c \tag{3.6}$$

Applying, Gauss's Theorem to equation 3.6, the semi-discrete form of the conservation equations for the average solution value for each control volume are obtained:

$$\int_{S_c} (\rho \vec{u} \phi) \cdot \vec{n} dS_c + \int_{S_c} (\Gamma_\phi \nabla_\phi \phi) \cdot \vec{n} dS_c = \int_{V_c} S_\phi dV_c \tag{3.7}$$

where S_c is the surface bounding the control volume V_c and $\vec{n}$ is a unit vector normal to the S_c.

A polyhedral control volume, such as that depicted in figure 3.1, is bounded by flat faces (f) and surface S_f. We can thus express equation 3.5 as:

$$\sum_f \int_{S_f} (\rho \vec{u} \phi) \cdot \vec{n} dS_c + \sum_f \int_{S_f} (\Gamma_\phi \nabla_\phi \phi) \cdot \vec{n} dS_f = \int_{V_c} S_\phi dV_c \tag{3.8}$$

Using Gaussian quadrature integration, the semi-discrete form may be written for a particular control volume as:

$$\sum_f [(\rho_{f_c} \vec{u}_{f_c} \phi) \cdot \vec{n} dS_f] + \sum_f [(\Gamma_{\phi,f_c} (\nabla \phi)_{f_c}) \cdot \vec{n} dS_{f_c}] = \int_{V_c} S_{\phi,c} dV_c \tag{3.9}$$

where f_c indicates the evaluation at the face centre. Variable values are calculated at the control volume centers, thus the integrand at the face centre are determined by interpolation. To preserve the midpoint rule accuracy, interpolation methods of at least second-order accuracy are used (see the interpolation paragraph below). A range of interpolation methods are included in the FLUENT solver directories.

For the discretization of the integrand over the source term, a second-order approximation is used in FLUENT. This is done by replacing the mean value of the integrand with the centre value of the source term of the control volume, i.e:

$$\int_{V_c} S_{\phi,c} dV_c = S_{\phi,c} V_c \tag{3.10}$$

This becomes exact if S_ϕ is constant or varies linearly within control volumes. Thus, the discretized form of the generic equation 3.5 is:

$$\sum_f [(\rho_{f_c} \vec{u}_{f_c})(\phi_{f_c}) \cdot \vec{n} dS_f] + \sum_f [(\Gamma_{\phi,f_c} (\nabla \phi_{f_c} \cdot \vec{n} dS_{f_c})] = S_{\phi,c} V_c \tag{3.11}$$

After discretization, the conservation equation for a general variable, ϕ, at a cell $\mathcal{P}$ can be written in linearised form as:

$$a_\mathcal{P} \phi_\mathcal{P} = \sum_{nb} a_{nb} \phi_{nb} + b \tag{3.12}$$

where, $a_\mathcal{P}$ is the centre coefficient of variable ϕ, a_{nb} is the influencing coefficient for the neighboring cell and b is the contribution of the constant part of the source term.

Linear Interpolation

The values of the solution variables, ϕ_{f_c} and its normal gradients, $(\nabla\phi_{f_c} \cdot \vec{n}dS_{f_c})$, are calculated at the control volume centre, and f_c indicates evaluation at the face centre. What is required is the values of the solutions variables and its normal gradients at the face centers. In order to obtain these values at the face-centre we apply interpolation methods. Among the different approaches, FLUENT uses the midpoint rule, and to preserve accuracy of the midpoint rule, interpolation methods of at least second order accuracy are employed. In this work the central-difference or linear scheme is used.

When linear interpolation is used the numerical solution can exhibit severe oscillations. This behavior depends on the local value of the Peclet number, Pe:

$$Pe = \frac{u\Delta x}{\Gamma} \tag{3.13}$$

where u is the magnitude of the fluid velocity, Δx is the control volume size in the x-direction and Γ is the diffusion coefficient. It can be shown that no oscillations occur if the the local Peclet number fulfils $Pe \leq 2$ at every grid node, which is a sufficient, but not necessary condition for the boundedness of the linear solution [122].

According to the linear interpolation scheme, the value of ϕ at the centre of a face f, connecting cell $\mathcal{P}$ with its neighbour cell $\mathcal{N}$, as shown in figure 3.1, is given by:

$$\rho_{f_c} = w\rho_{\mathcal{P}} + (1 - w)\rho_{\mathcal{N}} \tag{3.14}$$

where w is the linear-interpolation weight factor given by:

$$w = \frac{\mid \vec{r}_{\mathcal{N}} - \vec{r}_f \mid}{\mid \vec{r}_{\mathcal{N}} - \vec{r}_{\mathcal{P}} \mid} \tag{3.15}$$

and, $r_{\mathcal{P}}$, $r_{\mathcal{N}}$ and r_f are the position vectors of the centroids of cell $\mathcal{P}$, cell $\mathcal{N}$ and face f respectively.

However, since orthogonal meshes are used, and assuming a linear profile for ρ between cells $\mathcal{P}$ and $\mathcal{N}$, the magnitude of its gradient at the shared face may be evaluated as:

$$(\nabla\rho)_{f_c} \cdot \vec{n} = \frac{\rho_{\mathcal{N}} - \rho_{\mathcal{P}}}{d} \tag{3.16}$$

where d is the distance between both centers, i.e. $d = \mid \vec{r}_{\mathcal{N}} - \vec{r}_{\mathcal{P}} \mid$; and $\vec{n}$ is the unit vector normal to face f. This is the expression used for the normal gradient in equation (3.5).

3.4 The Numerical Algorithm

The linearised form of the discrete, non-linear governing equations produces a system of equations for the dependent variables in every computational cell. The resultant linear system is then solved to yield an updated flow-field solution. Since the governing equations are coupled to one another, the solution loop must be carried out iteratively in order to obtain a converged numerical solution. This loop is usually referred to as the outer loop. Solution of individual equations also involve iterations and it is usually referred to as the inner loop.

3.4.1 The Inner and Outer Loop

The steps of the outer loop are outlined below:

1. Initialise the flow field.

2. Update fluid properties (e.g, density, diffusivity, conductivity, specific heat), based on the current solution.

3. Solve the momentum equations, one after another, using the recently updated values of pressure and face mass fluxes.

4. Solve the pressure correction equation, using the recently obtained velocity field and the mass-flux.

5. Correct face mass fluxes, pressure, and the velocity field, using the pressure correction obtained from Step 4.

6. Solve the equations for additional scalars, such as energy, species, charge, and dissolved water, using the current values of the solution variables.

7. Update the source terms arising from the interactions among different phases.

8. Check for the convergence of the equations.

In the inner loop, the individual governing equations are discretized and solved. The loops continues until the convergence criteria are met.

The linearised algebraic equations result in a sparse coefficient matrix and it is solved using an implicit Gauss-Seidel linear equation solver in conjunction with an algebraic multi-grid (AMG) method [34]. Solution controls were used for all simulations. A bi-conjugate gradient stabilised method (BCGSTAB) for the species and potential equations are used in order to help ensure convergence. In addition, termination restrictions are set for all iterative equation solutions. The under-relaxation schemes used, are discussed further in the next section. An image with the appropriate controls is shown in figure 3.8.

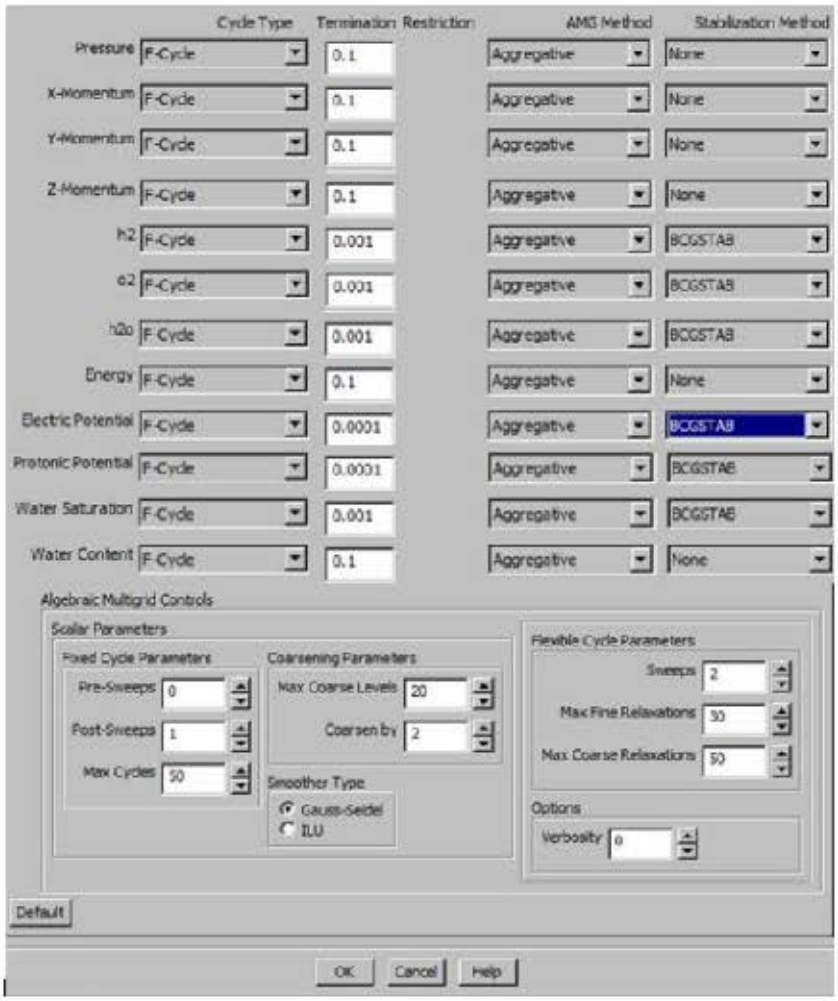

Figure 3.8: FLUENT Solution Controls

3.4.2 Under-relaxation Schemes

The above specifications are still not enough to handle the stiffness of the PEM fuel cell system. It is therefore necessary to control the change of ϕ. This is typically achieved by under-relaxation, which reduces the change in ϕ produced for each iteration, similarly for the evaluation of the source terms. In this thesis research, two kinds of under-relaxation techniques have been developed to tackle such stiffness difficulties. In the first kind of under-relaxation, the source terms and intermediate variables that are evaluated by other equations are under-relaxed in an explicit manner

$$S_{\phi}^{n} = \alpha \left(S_{\phi}^{new} - S_{\phi}^{n-1} \right) \tag{3.17}$$

$$\phi^{n} = \alpha \left(\phi^{new} - \phi^{n-1} \right) \tag{3.18}$$

Here, α is the under-relaxation factor which ranges from 0 to 1, $(S_{\phi}; \phi)^{n-1}$ is the solution from the previous iteration, and $(S_{\phi}; \phi)^{new}$ is the solution from the current iteration. As such, the new solution is stabilised based on a Gauss-Seidel type successive under-relaxation (SUR). This kind of under-relaxation technique has been deployed for the inner loop which solves individual linearised algebraic equations.

The second type of under-relaxation, known as the implicit relaxation of the equation, is performed on the outer loop which couples all equations together, as follows

$$\frac{a_p \phi^n}{\alpha} = \sum_{nb} a_{nb} \phi_{nb}^{n} + b + \frac{1-\alpha}{\alpha} a_p \phi^{n-1} \tag{3.19}$$

This kind of under-relaxation was proposed by Patankar, [121]. The main idea of this technique is to limit the change in each variable from one outer iteration to the next, because a change in one variable changes the coefficients in the other equations, which may slow or prevent convergence. It is found that the second kind of under-relaxation is more crucial for the present model, especially for the use of highly nonlinear equations where an extremely small under-relaxation factor (= 0.0001) has to be used at an early stage of iterations so as to avoid divergence. As the solution reaches a certain level of stabilisation, this factor can then be increased to a more aggressive value to speed up the convergence. The same procedure is repeated many times until a converged solution is achieved. Typically, an increase in the under-relaxation factors entails a slight increase in the residuals, but these increases usually disappear as the solution progresses, as shown in figure 3.9.
In the current work, the under-relaxation factor was increased after iterations 50, 100, 200 and 400 aggressively to speed-up convergence. These interventions are

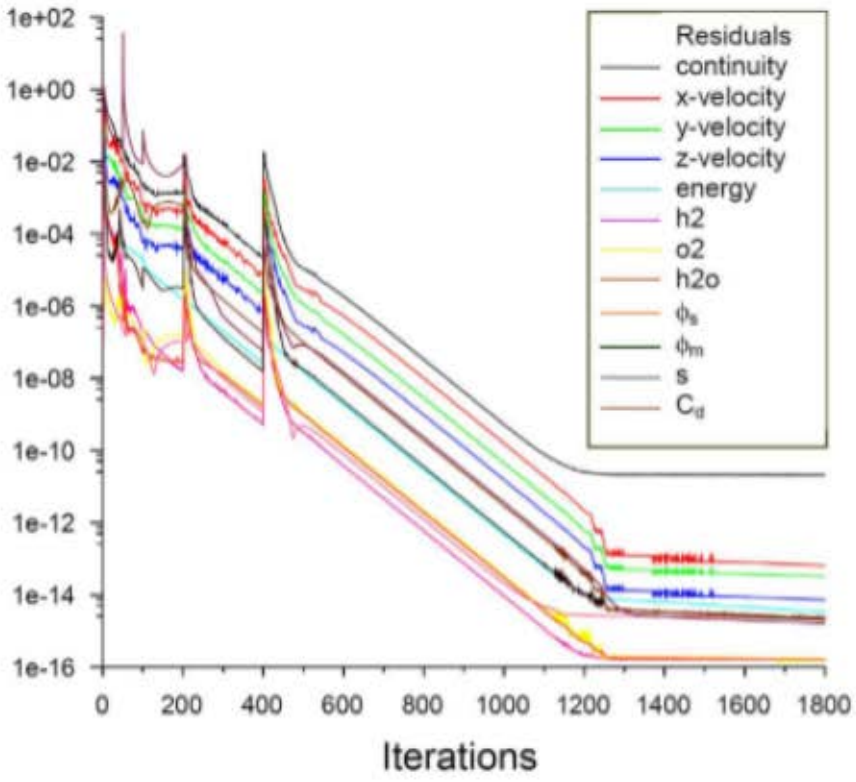

Figure 3.9: Convergence history of a steady state run is shown. For the first 50 iterations an extremely small under-relaxation factor ($\alpha = 0.0001$) is used to avoid divergence. As the solution stabilise the factor is increased aggressively at 50, 200 and 400 iterations to speed-up convergence. As the desired residual value is approached (below 1×10^{-12}) a smaller factor increases result in convergence. Big time scale variations, ranging from a minimum of 1×10^{-4} s to a maximum of 1 s for the transient transport processes will result in sharp peaks forming when the relaxation factor is adjusted aggressively

illustrated by the peaks in the residual values as indicated on the graph. This process continues, but with decreasing minor interventions till convergence below the desired residual value is reached.

3.4.3 Convergence Criteria

At the end of each outer iteration, the residuals for each of the conserved variables are computed and the computation stops when all residuals are below the convergence criteria. For the segregated solver of FLUENT, the residual is defined as

$$R^{\phi} = \sum_{cell} \left| \sum_{nb} a_{nb}\phi_{nb}^{n} + b - a_p\phi_p \right| \tag{3.20}$$

In general, it is difficult to judge convergence by examining residuals defined by equation (3.20), since no scaling is employed. This is especially true for flows such as natural convection where there is no inlet flow rate of ϕ with which to compare the residual. In this thesis we use the 'global scaled' residual which is defined as

$$R^{\phi} = \sum_{cell} \frac{|\sum_{nb} a_{nb}\phi_{nb}^{n} + b - a_p\phi_p|}{\sum_{cell} |a_p\phi_p|} \tag{3.21}$$

It represents the summation of imbalance in Equation (3.12) scaled by a factor representative of the flow rate of ϕ through the domain.

As can be seen, a fully converged solution is achieved after about 1300 iterations with the residuals all dropping below 1×10^{12} . In fact, residuals of 1×10^{8} are sufficiently accurate, including solution errors of all variables are less than 0.1. This has been defined as the convergence criteria in this study.

3.4.4 Solvers and Solutions Schemes

A variety of solvers and numerical schemes are available in FLUENT. Those used in this work include [34]:

The Segregated Solver

- The manner in which governing equations are linearised may take "implicit" or "explicit" form with respect to the dependent variable (or set of variables). By implicit we mean the following: For a given variable, the unknown value in each cell is computed using a relation that includes both existing and unknown values from neighboring cells. Therefore each unknown will appear in more than one equation in the system, and these equations must be solved

simultaneously to give the unknown quantities.

By explicit we mean the following: For a given variable, the unknown value in each cell is computed using a relation that includes only existing values. Therefore each unknown will appear in only one equation in the system and the equations for the unknown value in each cell can be solved one at a time to give the unknown quantities.

- In the segregated solution method each discrete governing equation is linearised implicitly with respect to that equation's dependent variable. This will result in a system of linear equations with one equation for each cell in the domain. Because there is only one equation per cell, this is sometimes called a scalar system of equations.

- A point implicit (Gauss-Seidel) linear equation solver is used in conjunction with an algebraic multi-grid (AMG) method to solve the resultant scalar system of equations for the dependent variable in each cell.

- Thus, the segregated approach solves for a single variable field (e.g. p) by considering all cells at the same time. It then solves for the next variable field by again considering all cells at the same time, and so on. There is no explicit option for the segregated solver.

First-Order Upwind Scheme

- 'Upwinding' means that the face value ϕ_f is derived from quantities in the cell upstream, or upwind, relative to the direction of the normal vector.

- When first-order accuracy is desired, quantities at cell faces are determined by assuming that the cell-centre values of any field variable represent a cell-

average value and hold throughout the entire cell; the face quantities are identical to the cell quantities. Thus when first-order upwinding is selected, the face value ϕ_f is set equal to the cell-centre value of ϕ in the upstream cell.

Second-Order Upwind Scheme

When second-order accuracy is desired, quantities at cell faces are computed using a multidimensional linear reconstruction approach [96]. In this approach, higher-order accuracy is achieved at cell faces through a Taylor series expansion of the cell-centred solution about the cell centroid. Thus when second-order upwinding is selected, the face value ϕ_f is computed using the following expression:

$$\phi_f = \phi + \nabla\phi \cdot \Delta\vec{s} \tag{3.22}$$

where ϕ and $\nabla\phi$ are the cell-centred value and its gradient in the upstream cell, and $\Delta\vec{s}$ is the displacement vector from the upstream cell centroid to the face centroid. This formulation requires the determination of the gradient $\nabla\phi$ in each cell. This gradient is computed using the divergence theorem, which in discrete form is written as

$$\nabla\phi = \frac{1}{V} \sum_{f}^{\text{N cells}} \phi_f \vec{A} \tag{3.23}$$

Here the face values ϕ_f are computed by averaging ϕ from the two cells adjacent to the face. Finally, the gradient $\nabla\phi$ is limited so that no new maxima or minima are introduced.

Chapter 4

Results and Validation

In this chapter the results of the numerical procedure described in Chapter 3, is discussed. The numerical data obtained from the thesis model are visualized as 2-D and 3-D graphics, and the distributions of the internal fields within the high temperature polymer electrode fuel cell are discussed. Included are the distributions of reactants and products in the various cell components, including temperature, pressure and current distributions throughout the cell. The performance of the fuel cell under the parameters and operating conditions of the thesis model is discussed. The chapter concludes with a discussion on the validity of the model's results. Experimental data of a high temperature polymer electrode fuel cell was not available from the laboratory of Hydrogen South Africa (HySA) at the University of Western Cape's campus, since work stations are setup only at stack level. Fortunately, experimental data was obtained from two other groups of researchers, both of whom are conducting world class research in high temperature polymer electrolyte fuel cells.

The first group is from the Hydrogen and Fuel Cell Research Center and the Samsung Advance Institute of Technology in the Republic of Korea, and the second group is from the Julich Institute for Energy Research in Germany.

Both institutes provide a thorough characterization of the components of their in-house cells, including micro-structure characterization and spectroscopy data analysis. Also, a prime factor in the choice of the groups were the compatibility in terms of geometric structure and dimensions with that of the thesis model. This included the parallel, serpentine-channel air and fuel flowplates, as well as compatible physical and operating parameters. Thus, the polarization-curve, cell efficiency and changes in operating condition simulations of the present work is based on the data supplied by the Hydrogen and Fuel Cell Center Research group, and the voltage loss and catalyst loading simulations are based on the data supplied by the Julich Institute of Energy Research Group.

This chapter has the following outline: In section 4.1, the model results which shows the distribution of reactants and products, including charge, potential and temperature in the different components of the HT PEM fuel cell are discussed; in section 4.2, fuel cell performance and the effects that some operating parameter changes such as pressures differences, catalyst porosity and catalyst weight ratios have on fuel cell performance are discussed. In section 4.3, the experimental set-up of both research institutes are described and the experimental results are used to validate the performance of the model fuel cell in respect of overpotential variations, temperature variations, oxygen concentration variations and flow rate variations.

4.1 Model Results

One of the main advantages and rationale of a mathematical model is to visualize the internal field processes taking place within each sub-domain of the fuel cell system. This information is hard to obtain otherwise, since certain variables such as current density and reactant distribution along the reactive region of the cell are difficult, if not impossible to measure without some invasive technique that will

have an influence on the cell performance. In this section the distribution of the various fuel cell fields within the reactive areas are presented from the numerical data of the thesis model.

In the present model, there are several input parameters that can be varied to study different working conditions. These include variations in stoichiometric ratios, inlet gas pressures, cell temperature, and cell output voltage.

The operating conditions used in the base case study are summarized in Table 4.1.

Parameter	**Symbol**	**Value**
Operating Condition		
Cell output voltage, V	ϕ_{cell}	0.65
Operating temperature, K	T	433
Gaseous pressure at the anode flow channel outlet, (atm)	P_a	2.0
Gaseous pressure at the cathode flow channel outlet, (atm)	P_c	2.0
Relative humidity of the anode side incoming gas flow,	RH_a	100
Relative humidity of the cathode side incoming gas flow,	RH_c	100
Stoichiometric ratio of the anode side incoming gas flow,	λ_a	1.4
Stoichiometric ratio of the cathode side incoming gas flow,	λ_c	1.8

Table 4.1: Structural Parameters

4.1.1 Reactants and Products Distribution

Oxygen Concentration Distribution

The visualization of the flow fields of both the reactants and products for the high temperature polymer exchange fuel cell is shown for a voltage of 0.4 V across the MEA (membrane electrode assembly), with corresponding current density of 0.16 A.cm^{-2}, and one with a voltage of 0.8 V across the MEA, and corresponding with

a high current density of 1.1 A.cm^{-2}. Figure 4.1. below shows the molar fraction of oxygen, which is the active gas in the air flow channels and cathode.

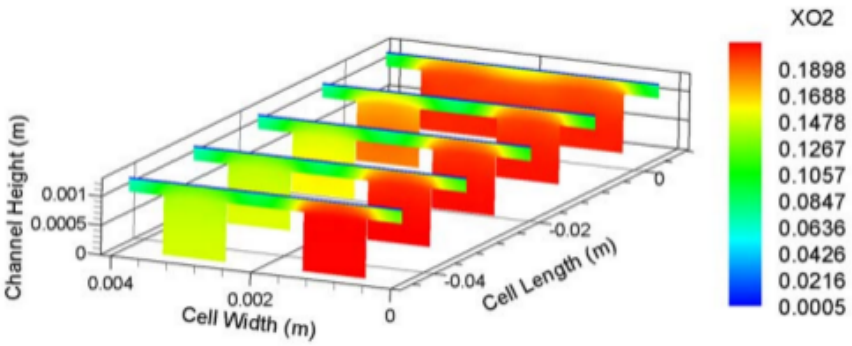

Figure 4.1: Oxygen molar fraction distribution in the cathode side for loading conditions: 0.16 A/cm^2

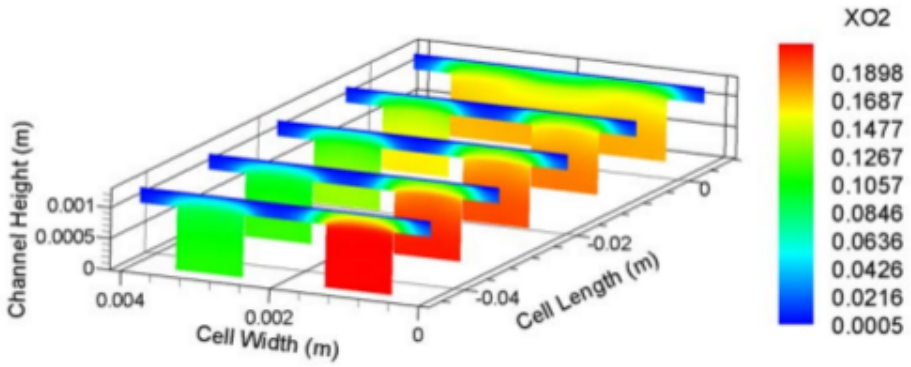

Figure 4.2: Oxygen molar fraction distribution in the cathode side for loading condition 1.1 A/cm^2

Figures 4.1 and 4.2 clearly shows the rapid decrease in the mole fraction and hence concentration of the oxygen gas both in the convective direction along the channels and the diffusive direction towards the active membrane areas. The depletion is more pronounced further from the channel inlets. The oxygen concentration is well distributed in the cathode catalyst layer, but slightly higher at the gas channel/ gas diffusion layer interface. Also, concentration under the channel is higher than under the current collector. Oxygen diffuses from the gas channel into the other parts of the domain mainly due to a concentration gradient. It is noted that

the diffusion coefficient plays a crucial role on the gradient of the gas concentration, which also depends upon the rate of consumption of the reaction at the catalyst layer. This provides an estimate of the limiting current density of the cell, and gives rise to a concentration polarization at the high current density operation.

Hydrogen Concentration Distribution

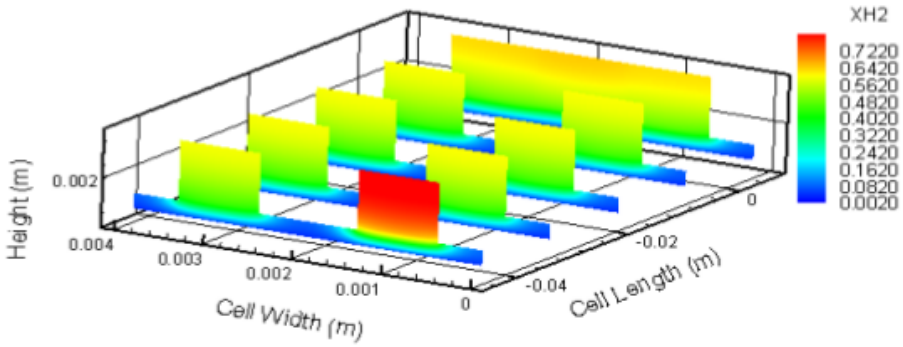

Figure 4.3: Hydrogen molar fraction distribution in the anode side for loading conditions 0.16 A/cm^2

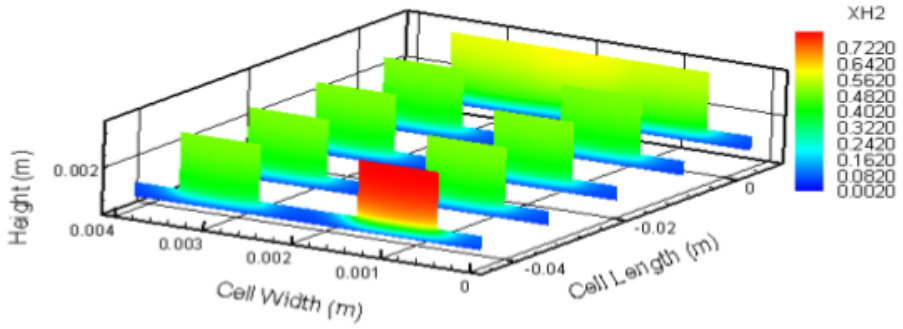

Figure 4.4: Hydrogen molar fraction distribution in the anode side for three loading conditions 1.1 A/cm^2

The hydrogen concentration gradient is less than the oxygen concentration gradient, noticeably, because the amount of hydrogen consumed by the reaction is influenced by the higher diffusion of hydrogen through the gas channels, resulting in a more uniform spread and also the stoichiometric flow rate which influence the amount of hydrogen fed into the flow channel. This relationship is discussed in

section 4.3.5. Inside the catalyst layer the hydrogen mole fraction varies slightly, but is higher in the area under the gas channel, and lower in the area under the current collector. The reason for this can be explained by examining the water vapor mole fraction in the area under the gas channel. In this area, the membrane water content, and hence water vapor mole fraction in the anode mixture is low, since water is transported from the anode to the cathode via electro-osmotic drag. This reduction in water vapor results in an increase in the hydrogen mole fraction. On the other hand, water content in the catalyst is higher under the land area. In this region, water is transported from the cathode to the anode by back-diffusion and the water vapor mole fraction will increase. As a result the hydrogen mole fraction has to decrease. Nonetheless, we notice that the molar concentrations of hydrogen gas in the anode flow channels, shown in figure 4.3 and 4.4., changes by less that 2 percent even at high current density.

Water Concentration Distribution

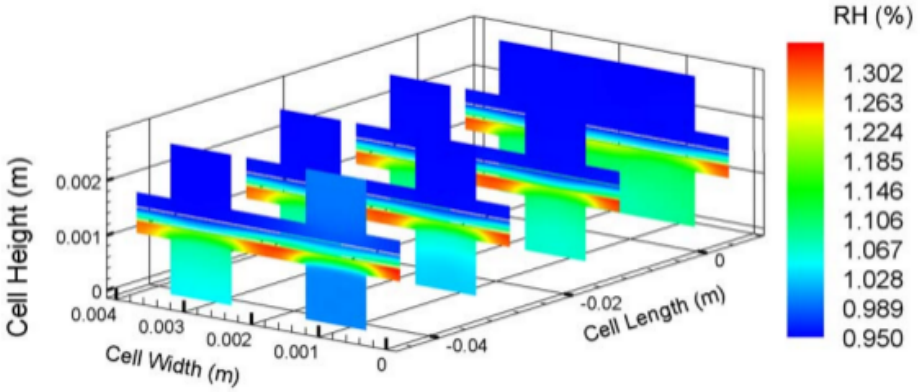

Figure 4.5: Water distribution in the cell for loading conditions 0.16 A/cm^2

The water vapor mole fraction at the anode electrode is initially dependent on the relative humidity of the feed stream at the anode inlet. It decreases to around 50 percent of its initial value when the current density is increased to the higher level of 1.1 A/cm^2. This is attributed to electro-osmotic drag of water to the cathode. Consequently, membrane conductivity in this region decreases. On the

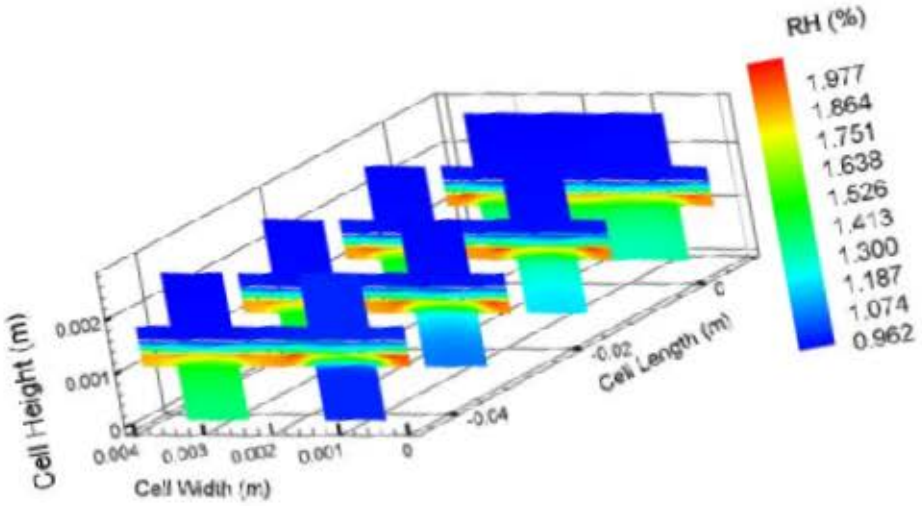

Figure 4.6: Water distribution in the cell for three different loading condition 1.1 A/cm^2

cathode side, the water vapor mole fraction increases due to water production at the cathode catalyst layer and the migration of water molecules from the anode side. This results in higher membrane conductivity and an increase in cell potential. We also notice that the areas under the gas channel has a higher water content than the areas under the current collector on the cathode side. There is practically no difference in anode water content for these two areas, especially at low current density. The production of water in the area under the gas channel also increase with higher current densities. Simultaneously, more water is evacuated from the anode due to a higher drag coefficient, resulting in a lower water content at the anode. At the cathode however, this increased water concentration is balanced by water fluxes to the catalyst/ gas diffusion layer interface so that the water vapor fraction remains similar, ever at higher higher density operations.

4.1.2 Charge Distribution in the MEA

The volumetric current densities at low and high current densities are illustrated in figures 4.7, 4.8 and 4.9 below:

The potential difference imposed on the boundaries drives the reaction in the catalyst layers resulting in corresponding current flow across the electrodes. Volumetric Current density is a function of oxygen concentration and activation overpotential. Thus, the volumetric current density and overpotential in the catalyst layer

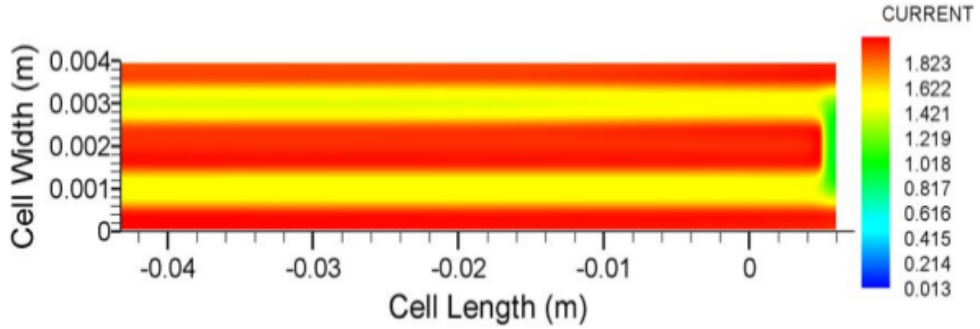

Figure 4.7: Charge distribution for cell voltage drop 0.4 V

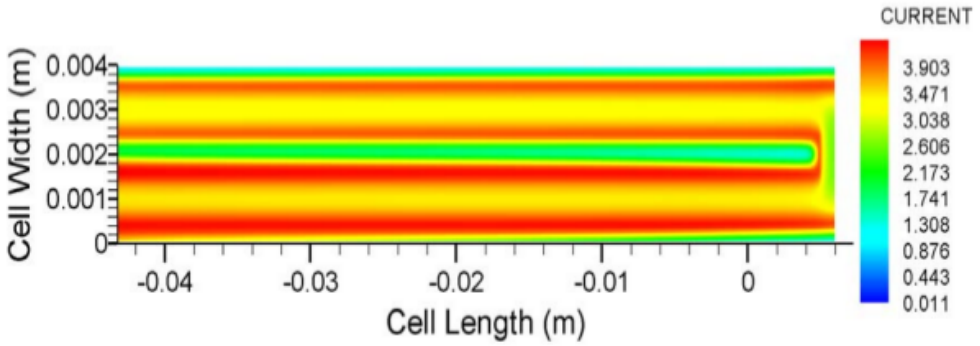

Figure 4.8: Charge distribution for cell voltage drop of 0.8 V

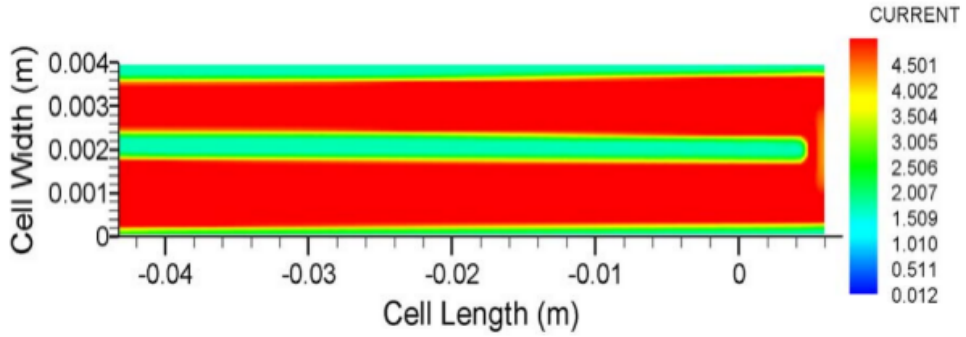

Figure 4.9: Charge distribution for cell voltage drop of 1.0 V

of the anode is almost zero. It increases slightly near the catalyst membrane interface, but even there it is very small due to the extremely fast hydrogen oxidation reaction kinetics. On the other hand, the volumetric current density at the cathode side are more broadly distributed. Figures 4.7 to 4.9 shows the current distribution for three loading conditions. For low load condition, the effect of oxygen transport

is small, i.e. the concentration of oxygen under the land area is still high, therefore the current density is higher under the land area. However, as the loading condition increases, the oxygen transport limitation under the land area become significant which results in the shift of current maxima towards the center of the channel where oxygen concentration is highest. The current density generally decreases from inlet to outlet as the oxygen concentration decreases. Also for high load condition, the current at the outlet is almost entirely located under the channel area.

4.1.3 Overpotential Distribution

Activation Overpotential Distribution in the Cathode Catalyst Layer

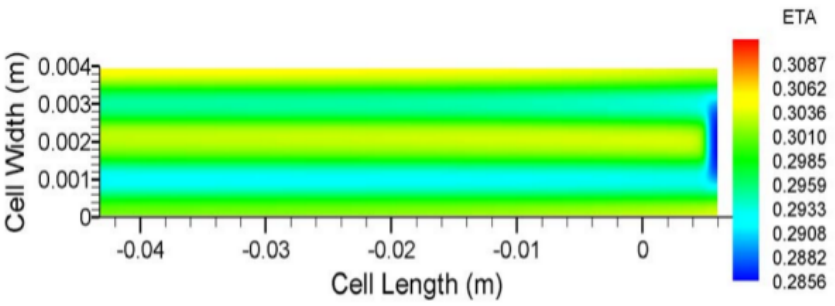

Figure 4.10: Activation Potential for cell voltage drop of 1.0 V

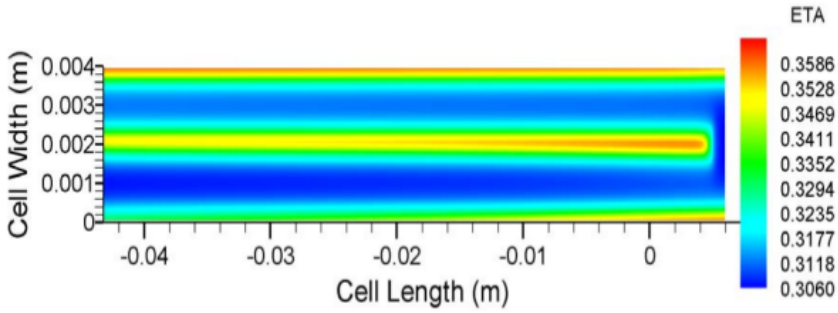

Figure 4.11: Activation Potential for cell voltage drop of 0.8 V

Figures 4.10 to 4.12 show the cathode activation overpotential distribution in the first sub-layer (GDL/catalyst layer interface) of the catalyst layer. In all loading conditions, the distribution patterns of activation overpotentials are similar, with

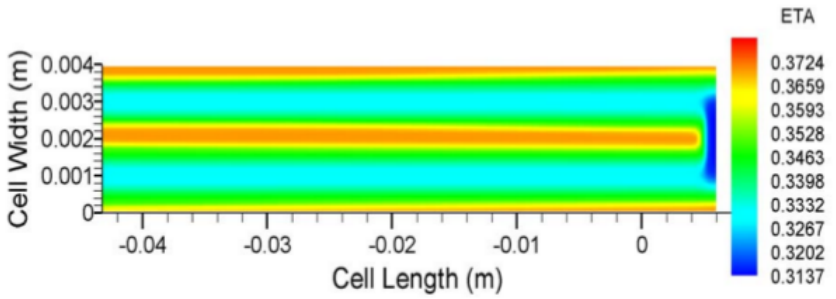

Figure 4.12: Activation Potential for cell voltage drop of 1.0 V

higher activation overpotentials under the land area. This uneven distribution is mainly due to the lower ohmic loss under the land area than under the channel area. Since activation overpotential has an exponential effect on the magnitude of local current, it can be deduced that the potential condition for producing current under the land area is more favorable in the absence of oxygen transport limitation.

Ohmic Overpotential

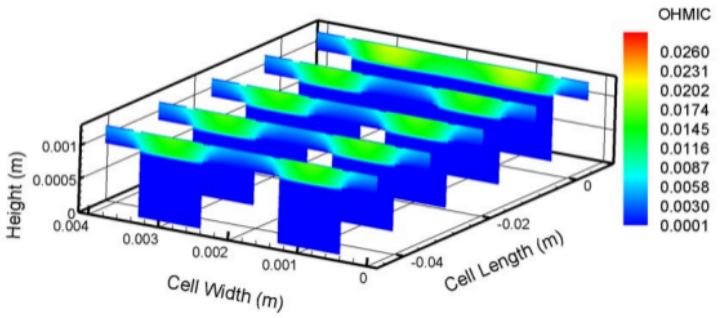

Figure 4.13: Ohmic overpotential in the cathode gas diffusion layer for a voltage drop of 0.4 V

Ohmic overpotential is the voltage loss due to resistance to electron transport in the gas diffusion layers. For a given load, the magnitude of this overpotential is dependent on the path travelled by the electrons. The longer the path, the larger the potential drop. Therefore the ohmic loss under the channel area is higher than the loss under the gas diffusion layer since the electrons have to travel a longer distance to reach the catalyst layer under the channel area. Figures 4.13 and 4.14 show that the ohmic overpotential distribution patterns are similar for all loading

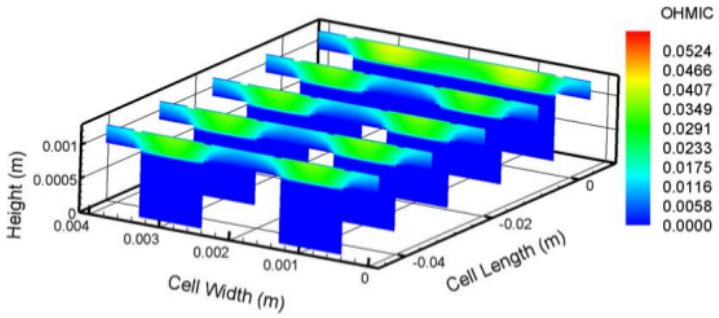

Figure 4.14: Ohmic overpotential in the cathode gas diffusion layer for cell voltage drop of 1.0 V

conditions. However, the magnitude of the potential loss increases with cell loading.

Membrane Overpotential

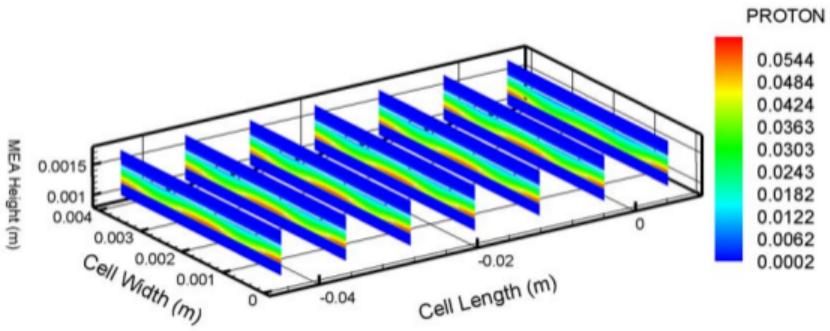

Figure 4.15: Potential Drop across the membrane for a voltage drop of 0.4 V

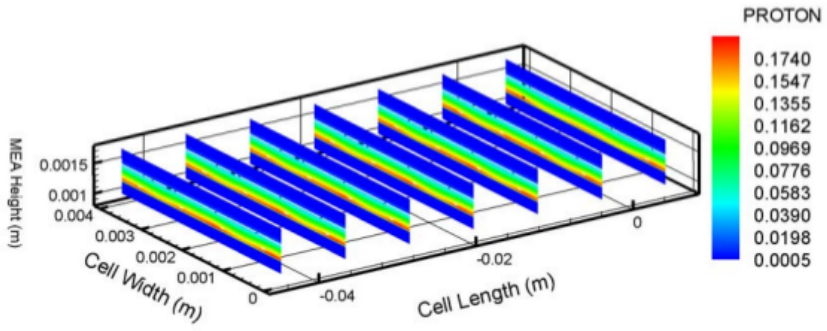

Figure 4.16: Potential Drop across the membrane for a voltage drop of 1.0 V

The potential loss in the membrane is due to resistance to proton transport across the membrane from anode catalyst layer to cathode catalyst layer. The

distribution pattern of the protonic overpotential is also dependent on the path traveled by the protons and the activities in the catalyst layers. Figures 4.15 to 4.16 show the potential loss distribution in the membrane for three loading cases. At low loading condition, the potential drop under the land area is higher because the catalytic activity is higher. However, at high load condition the potential drop is more uniformly distributed across the membrane. It is expected that at high load, more protons are produced under the channel area at the anode catalyst layer because the activity is quite high such that the hydrogen concentration under the land area would be low. Combining this effect with the current density distribution in the cathode catalyst layer where protons are consumed and where the activity is higher under the channel area, results in the more uniform overpotential distribution observed for high load condition.

4.1.4 Analysis of the Turning Region

Some interesting characteristics are observed at the turning region for the chosen geometry. The main cause of the different distribution patterns in the turning region is due to the higher ohmic loss in this region. This higher ohmic loss gives rise to a lower activation overpotentials which lead to lower current densities, figure 4.17. The higher ohmic loss in the turning region is due to the fact the main area of this region is under the channel area and that the ohmic loss under the channel area is higher than under the land area. This characteristic would not be observed if the gas diffusion layer is extended to cover the outside edge of the turning region.

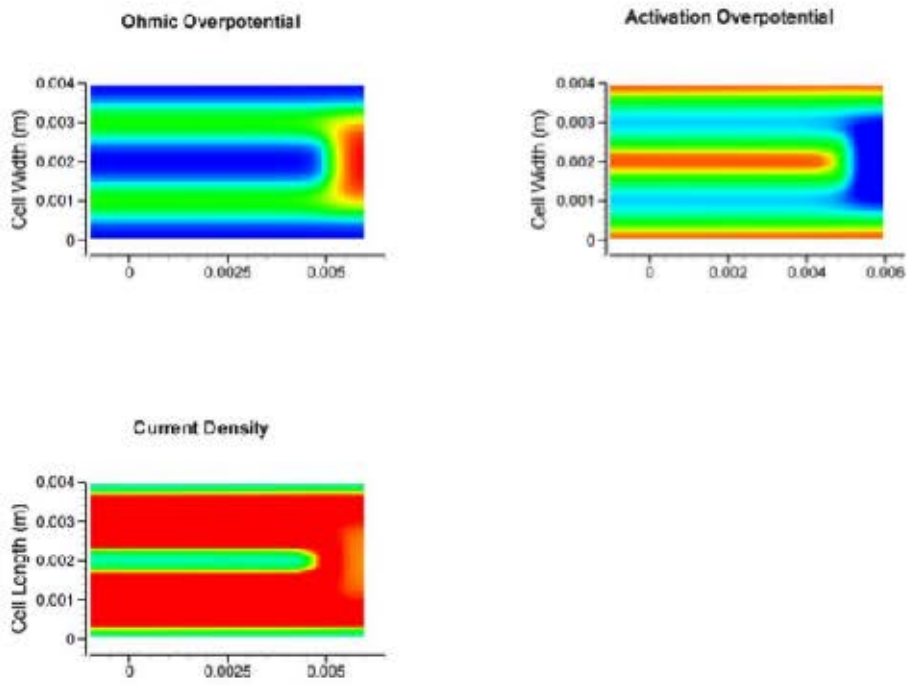

Figure 4.17: Distribution at the turning point of the gas channels for loading case 1.2 A/cm^2

4.1.5 Temperature Distribution

The temperature distribution within the MEA is discussed. The main heat source in the fuel cell comes from the exothermic oxygen reduction reaction at the cathode catalyst layer. Resistive heating in the membrane and catalyst layers also plays a significant role. The non-uniform temperature profile are depicted in figure 4.18. The temperature across the MEA is not much different due to the large thickness to length ratio i.e. a very thin MEA. Temperature difference of 4 degrees are observed at high current density and 1 degree when operated at low current density. The heat generated are also much higher under the current collector than under the gas channels. The imposed constant temperature at the boundaries dominate the temperature distribution in the MEA. This causes the heat fluxes to diffuse from the middle of the MEA under the gas channel to the solid current collectors.

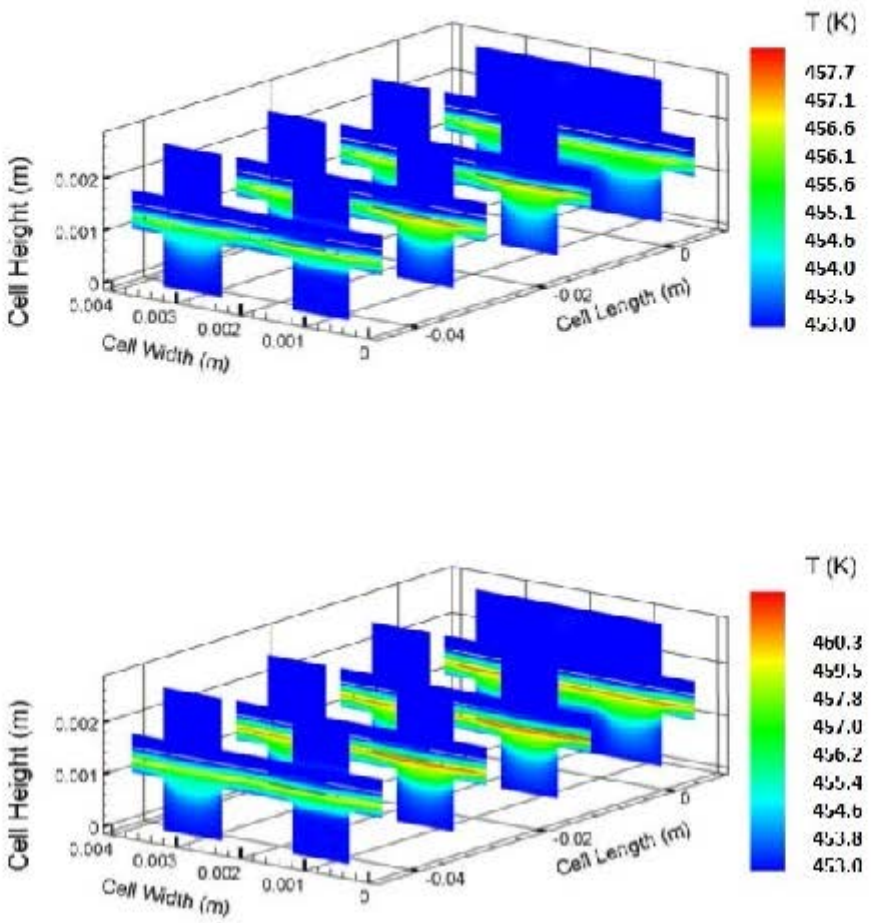

Figure 4.18: Temperature distribution in the cell for two loading cases: 0.7 A/cm^2 (top), and 1.2 A/cm^2 (bottom)

4.2 Fuel Cell Performance

The performance of the the high temperature polymer electrode fuel cell as constructed by the thesis model are best illustrated with the aid of current density versus cell potential curve (polarization curve), also against current density versus power density curve, as is illustrated in figure 4.19.

The curves represent outputs of the thesis model operating with a flow rate of 1 l.min^{-1}, and a temperature of 433 K. The open circuit voltage of the model fuel cell is 0.95 V. When it operates at low current density the potential at the cathode can be 0.85 V above that of the anode. The region of low current density (between 0 and 0.4 A.cm^{-2}) is characterised by a sharp drop in potential and an increase in (but

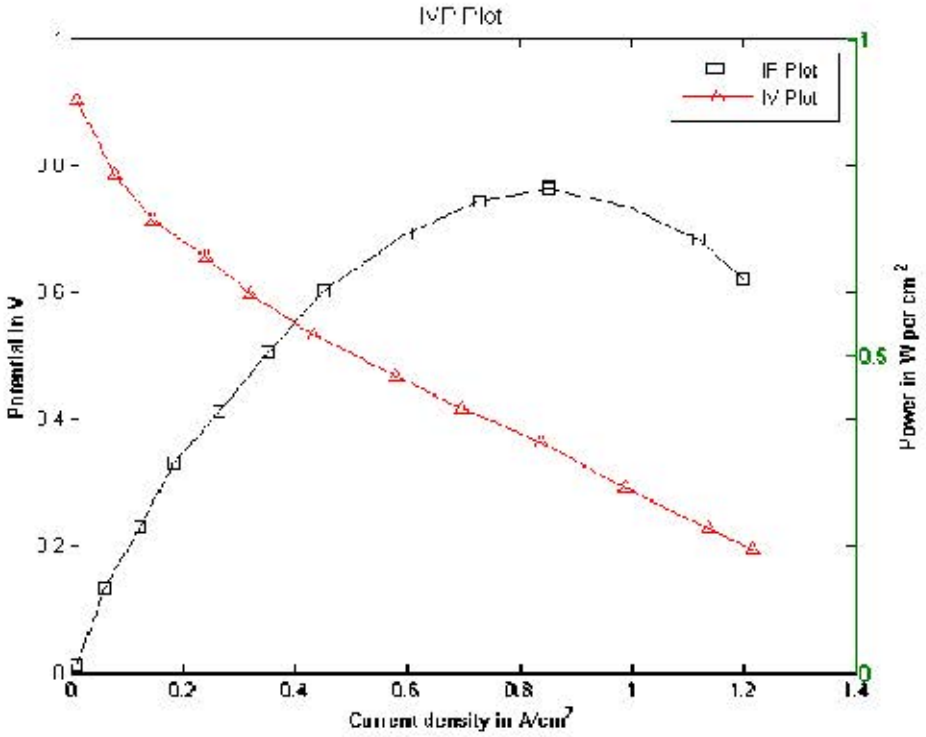

Figure 4.19: The polarization curve is represented by the red line plot and the power density curve by the black line plot for the HT PEMFC operating at 433 K temperature and with input flow rates of 1 l.min^{-1} for fluid and air gases

still low) operating current density. Voltage is loss in this region is caused by the fluid and air gases are driven through the porous electrodes and activation energy is required to initiate the cathode oxidation reactions and anode reduction reactions. The potential loss here is fairly steep. In the second region where operating current densities range from 0.4 and 1.2 A.cm^{-2} we observe a gradual loss of voltage mostly due to the ohmic resistance to the flow of charge in the membrane and electrodes. The third region is not illustrated by the graph, but after the optimal operating current density of between 0.88 and 0.9 A.cm^{-2} is reached, distinct concentration overpotential is reached due to the depletion of oxygen. Potential is thus loss due to concentration overpotential.

The model HTPEMFC therefore produces a maximum power density distribution of 0.76 W .cm^{-2} when it operates at a current density of between 0.88 and 0.90 A.cm^{-2} and has an operating potential between 0.38 V and 0.40 V.

4.2.1 Effects of Operating Pressure Difference on Fuel Cell Performance

It is clear from the general polarization curve, discussed above, that the cathodic overpotential caused by the oxidation reduction reaction is responsible for most of the potential losses in the fuel cell. Indeed, it accounts for 80 percent of the total loss. This is mainly due to ohmic resistance to the flow of charge, combined with mass transport losses caused by the diffusion of gaseous oxygen through the porous electrode and the diffusion of oxygen to the reaction sites. Thus, the performance of a PEM fuel cell will be limited by the oxidation reduction reaction on the cathode side.

In figure 4.20 we investigate the effect of operating pressure difference between the inlet gas flow and outlet gas flow on the performance of the fuel cell, and in figure 4.21 the effect of operating pressure difference on cell performance, using the power density - current density curve, is investigated.
At low current density, up till 0.2 A.cm^{-2}, the same amount of potential losses are experienced, irrespective of the differences in operating pressure i.e. flow rates have no effect on the potential required to activate the cell reactions. This is clearly observed in figure 4.20. At current densities higher than 0.2 A.cm^{-2} however, we notice that with an increase in pressure difference the potential loss decreases as the pressure difference increases. This is mainly because the mass flow of air, which is entering the cathode increases, and as a result the diffusion of oxygen to the reaction sites will be greater, thereby decreasing the concentration overpotential.

In figure 4.21, we observe that both the reaction overpotential and ohmic overpotential, which falls in the currency density range of 0 A.cm^{-2} to 0.4 A.cm^{-2} produce similar power density outputs, irrespective of pressure differences. However, in the current density range higher than 0.4 A.cm^{-2}, an increase in pressure difference in the flow fields results reduces potential losses and result in an increase

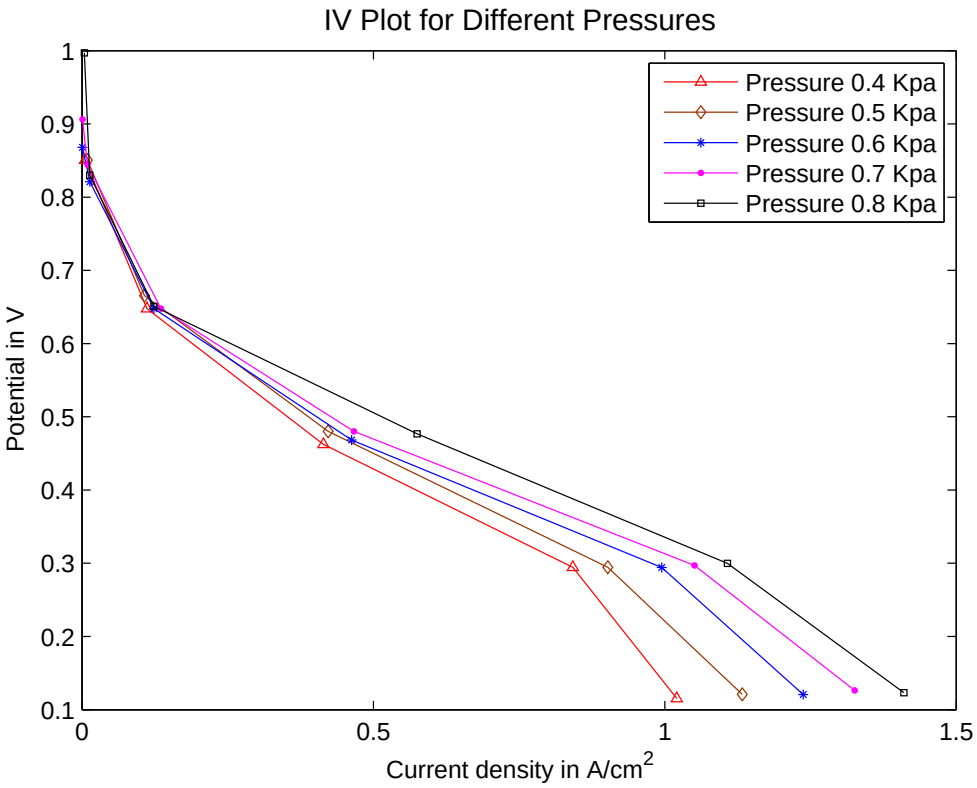

Figure 4.20: Polarization Curves for operating pressure differences between inlet flow rates and outlet flow rates ranging from 0.4 kPa to 0.8 kPa

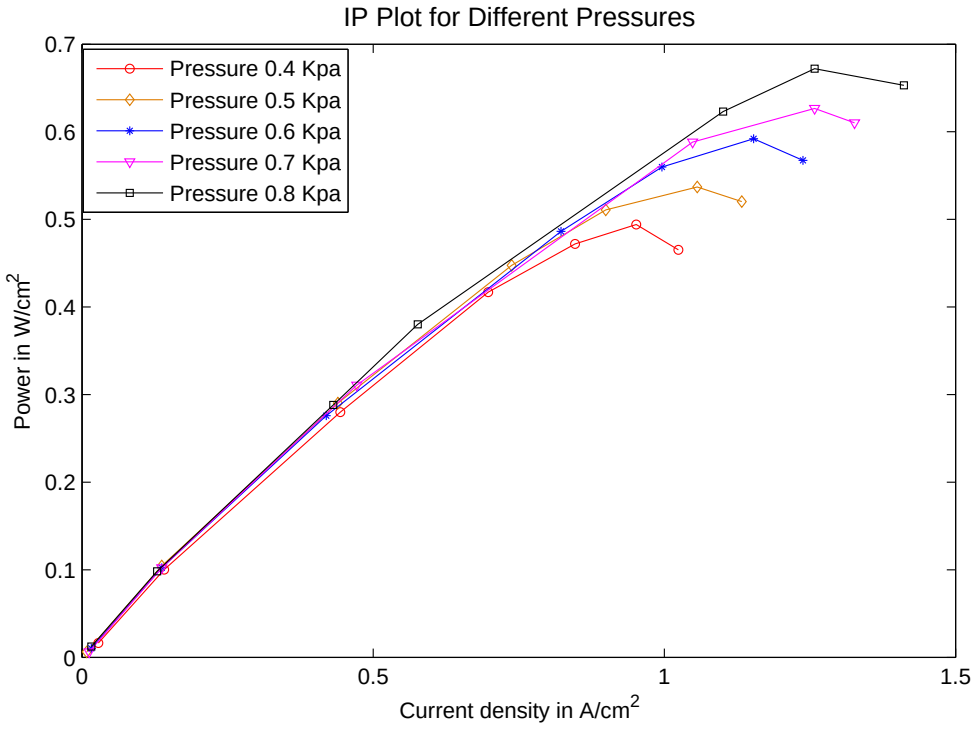

Figure 4.21: Power density curves for operating pressure differences between inlet flow rates and outlet flow rates ranging from 0.4 kPa to 0.8 kPa

in limiting current density and an increase in the output power density of fuel cells. Both graphs indicate that the effect of a high pressure difference results in a much lower concentration overpotential of the fuel cell and hence increase the fuel cell performance.

4.2.2 Effects of Catalyst Porosity on Fuel Cell Performance

To guarantee the durability of high temperature PEM fuel cell performance which is essential for long-term, stable operations, the polarisation loss of a HT PEM fuel cell must be minimised. Operating conditions, including oxygen partial pressure, temperature and humidity all affects cell performances. However, we also need to consider the relationship between the pore networks in the cathode catalyst layer and the polarisation characteristics, which is not always adequately covered in the published literature. In figure 4.22, we show the effect of different porosities of the catalyst layer on the polarisation curve. The same loading of 10 mg. cm^{-2} of Pt and catalyst layer thickness of 11 μ m is used for porosities of 40 percent and 50 percent for the catalyst layer.

Figure 4.22 shows that the catalyst layer with porosity of 50 percent experiences a much higher ohmic potential loss than the one with a catalyst porosity of 40 percent. This results in the limiting current density being reached much earlier in the case of a higher porosity than that of the lower one, and consequently cell performance is reduced. The reason for this is mainly due to the higher porosity catalyst layer possessing less active surface areas and thus more void spaces. Void spaces hinders the accessibility of protons to reach the reactive sites, resulting in an increase in ohmic overpotential. Though, this provides greater access to the diffusive fluxes of reactive gases e.g. oxygen, the slow rate of proton flow will still considerably reduce fuel cell performance.

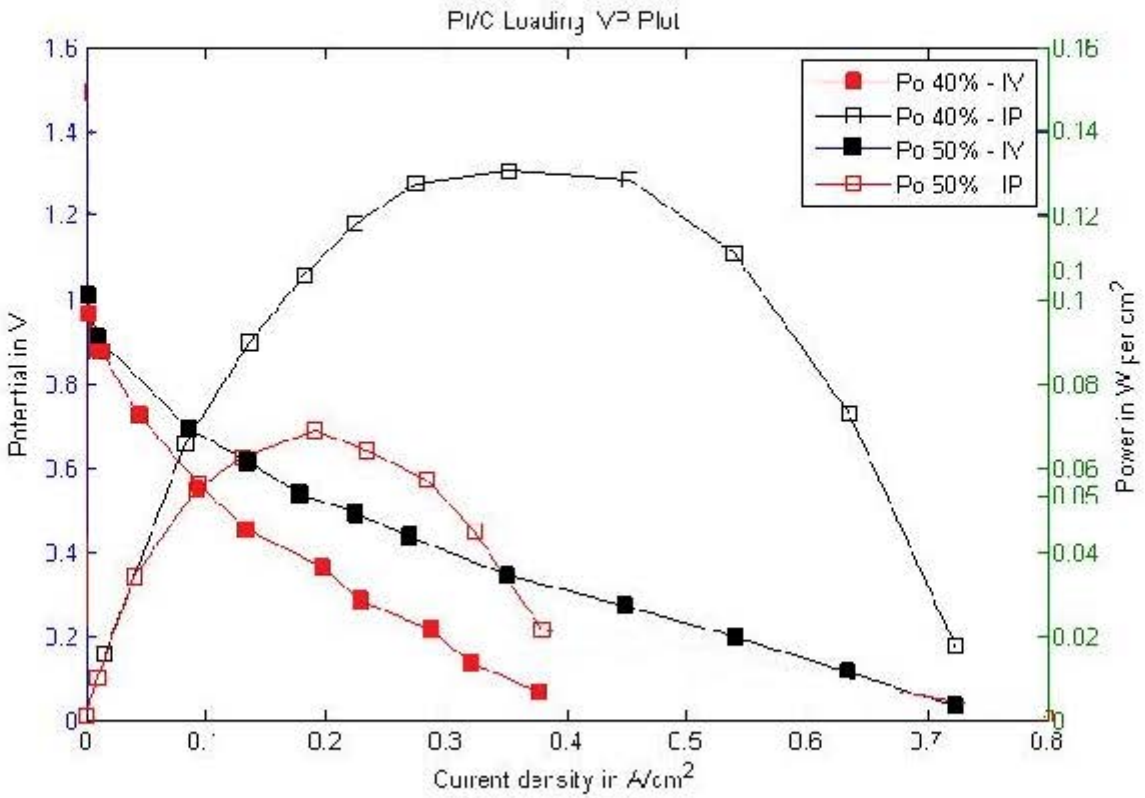

Figure 4.22: Polarisation curves (black and red dotted lines) and power density curves (black and red solid lines) for catalyst with porosities of 40 percent and 50 percent. Both catalysts has Pt/C loading of 10 wt percent and electrolyte with 20 wt percent

4.2.3 Effects of Catalyst Pt/C weight ratio on Fuel Cell Performance

In figure 4.23, we show the effect of different Pt/C weight ratios of the catalyst layer on the polarisation curve. The same loading of 10 mg. cm^{-2} of Pt and a catalyst layer thickness of 11 μ m is used, but Pt/C weight ratios of 10 wt percentage, 30 wt percentage, and 50 wt percentage for the catalyst layers, are used.

The results in figure 4.23 show an increase in cell performance as the Pt/C weight ratio of the catalyst layer increases. This is mainly due to a monotonic decrease in ohmic potential loss as the weight ratio increases. Since the Pt loading for each of the catalysts loads are the same, an increase in Pt/C weight ratio will imply an increase in carbon load of the catalyst. This will reduce the amount of void spaces

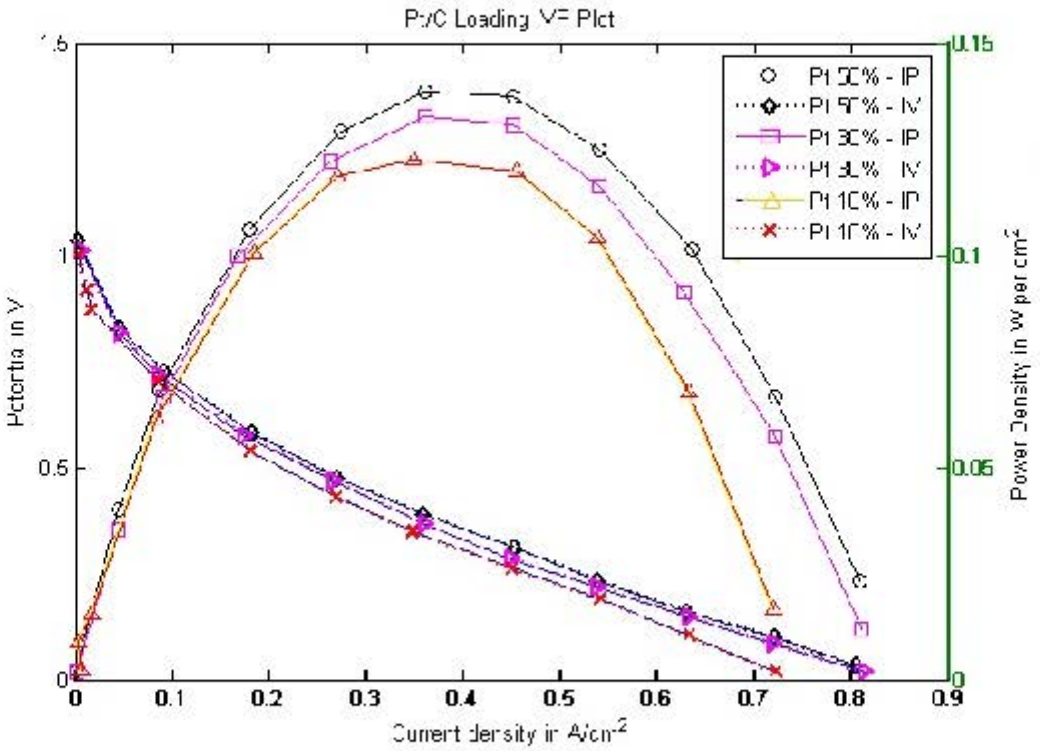

Figure 4.23: Polarisation curves (dotted lines) and power density curves (solid lines) for catalysts with different Pt/C weight ratios ranging from 50 percent to 10 percent

and increase the number of active surface areas. Thus, we will get a decrease in ohmic overpotential with an increase in Pt/C weight ratio.

4.3 Parametric Study and Performance Validation

In this section the validity of the numerical tool developed for this model is evaluated by comparing the numerical results obtained from the thesis model with the results obtained from the experimental work on high temperature polymer electrode fuel cells developed by Jintao Kim and co-workers at the Hydrogen and Fuel Cell Research Centre and the Samsung Advance Institute of Technology in the Republic of Korea. The construction and characterisation processes of the fuel cell is summarised in this section.

The single cell used in the experiments has a commercially obtained membrane electrode assembly (MEA), Celtec P1100, from BASF, with an active cell area of 45 cm^2. A woven carbon cloth was used as the gas diffusion layer. Hard-type gaskets were the sealing material clamping a single cell and as a stopper that properly compress the MEA after clamping. The graphite flowplates contain three parallel serpentine channels on the anode and cathode. The unit cell was tested in a furnace to ensure isothermal conditions. The temperature was controlled using a PID (proportional-integral-derivative) controller. A schematic diagram of the test station is shown in figure 4.20, [84]:

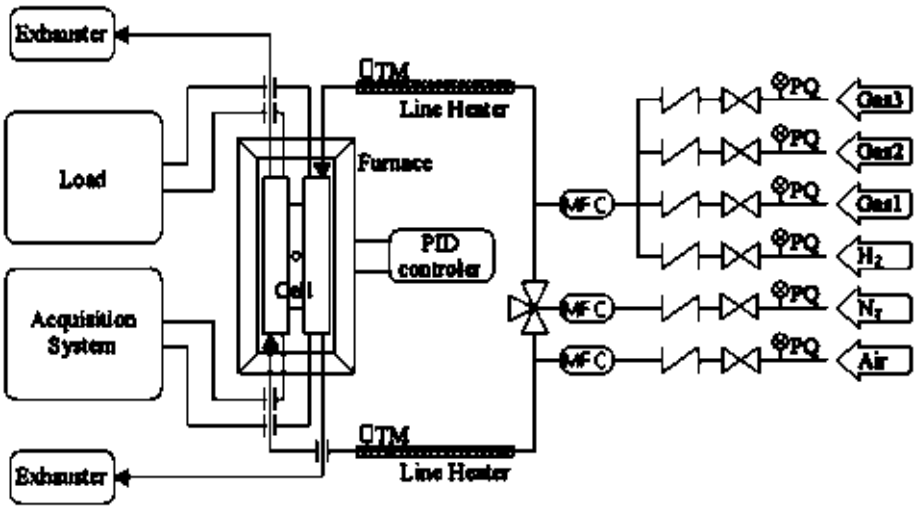

Figure 4.24: Schematic diagram of test station for HT PEMFC at Hydrogen and Fuel Cell Research Centre, [84]

The experimental fuel cell parameter and geometric dimensions are given in the table 4.1. at the end of this chapter.

A second set of validation data tested against the thesis model is obtained from experiments performed by O. Shamerdina and his group at the Julich Institute for Energy Research in Germany. The validation is done against voltage losses, catalyst loading and changes in temperature conditions. A summary of the experimental set-up and operating parameters are given.

A HT PEMFC was prepared in-house with all the components of the membrane electrode assembly self-made. The catalyst layer was prepared by spraying Johnson Matthey HiSpec 3000 catalyst powder, using an airbrush, onto the gas diffusion layer- providing 20 percent Pt/C. The electrodes were baked at 350 ^0C (623 K) for 20 minutes. The resulting Pt-loading was approximately 1 mg/cm^2. Phosphoric acid doped PBI-O-PhT membranes were used with different additives as electrolyte that were prepared in A.N Nesmeyanov Institute of Organoelement Compounds of the Russian Academy of Sciences. The membrane electrode assembly was approximately 50 cm^2, and the flow field geometry serpentine.
Polarisation curves were measured at cell temperature of 433 K and ambient pressure, except for experiments where different temperature were required. Reactant gases of H_2 and dry air were operated at a fixed flow rate with current density of 0.4 A.cm^{-2}. A potentiostat Autolab 320 with frequency response analysis module and 20 A booster was used to measure data curves.

The Experimental conditions and set-up parameters for this research groups are given in the table 4.2. at the end of this chapter.

4.3.1 Performance Validation

Polarisation curves i.e. cell potential versus current density, and also power density versus current density curves, are normally regarded as a good measure to evaluate the performance of a fuel cell. The experimental I - V and I - P curves reported by Jintao Kim et al in [84] are plotted against the numerical results of the thesis model.

It is found that the current density predicted by the current model is higher than that of the experimental data. A possible reason for this overestimation might be that there are still some factors, such as thermal and electrical contact resistances, anisotropic structures of the real materials, and compression effects that were not taken into account in the mathematical model. Thus, in order to obtain the same

current density as the experimental data, a certain degree of parameter fitting is required. The following fitting procedure where two parameters were adjusted, as illustrated by Baschuk [111], was obtained through a test and error shooting process:

- The reference exchange current density is reduced from:
  $aj_{0,a}^{ref} = 5 \times 10^8$ A.m^{-2} and $aj_{0,c}^{ref} = 1.2 \times 10^2$ A.m^{-2}
  to $aj_{0,a}^{ref} = 1 \times 10^7$ A.m^{-2} and $aj_{0,c}^{ref} = 1.3 \times 10^1$ A.m^{-2}

- The electrical conductivity of the gas diffusion layer is reduced from 750 S.m^{-1} to 620 S.m^{-1}

The model agrees very well with the experimental results with these new parameters. The polarisation and power density curves for the two sets of data are given in figure 4.25 and it demonstrates that the present model is capable of predicting practical fuel cell operations with a certain level of parameter fitting.

As shown in the figure there is a good match between the experimental data and the model-predicted results up till 0.1 A.cm^{-2}, with the maximum deviation of the model results (between current densities of 0.1 A.cm^{-2} and 0.4 A.cm^{-2}) below 5 mV from the experimental data.

A sharp fall, due to activation loss is observed for current densities less than 0.1 A.cm^{-2}, while a linear drop in potential for current densities between 0.2 A.cm^{-2} and 0.6 A.cm^{-2} is seen. At current densities higher than 0.6 A.cm^{-2} the model results shows a much bigger voltage drop than the experimental results. This means that the oxidant supply at the catalyst layer was sufficient for the reaction up till this stage. The voltage losses are compared to get an estimate of how the limiting densities between the two sets of data compare. Figure 4.26 shows the overpotentials of the two sets of data.

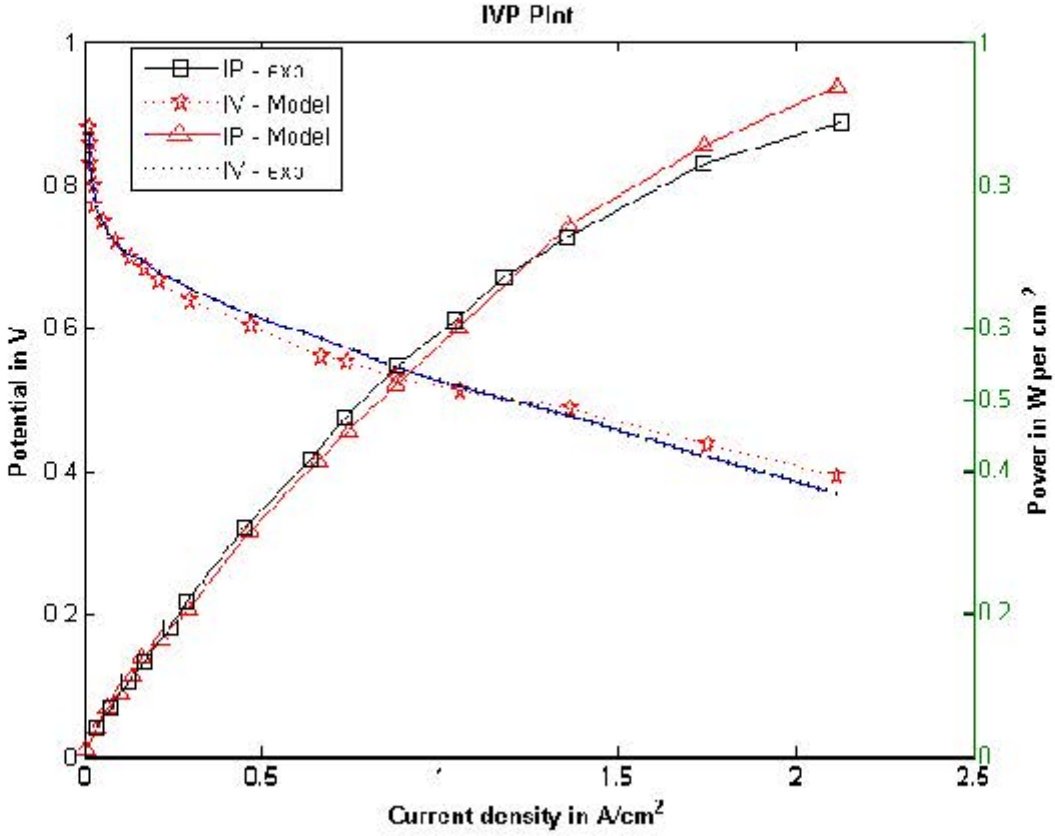

Figure 4.25: Polarisation curves (blue and red dotted lines) and power density curves (black and red solid lines) for the model data and the experimental data after parameter fitting. Comparison between the fuel cell performance for the two sets of data is illustrated

4.3.2 Effect of Overpotential Losses

We observe a close correlation between the potential losses (overpotentials) of the model-predicted data and the experimental data. However, the model-predicted data shows a slight under-estimation of potential losses as we move to higher current densities. In both cases, it is evident that the major contributors to voltage loss in a high temperature PEMFC is firstly due to the oxygen reduction reaction at the cathode, secondly the PBI-membrane resistance to the flow of protonic charges, and thirdly the depletion of oxygen concentration further along flow channels due to the low percentage present in air (21 percent), and thus rapid consumption at the beginning of the flow. The effects of concentration depletion at the reaction sites and reaction kinetic potential loss for hydrogen is found to be very limited in

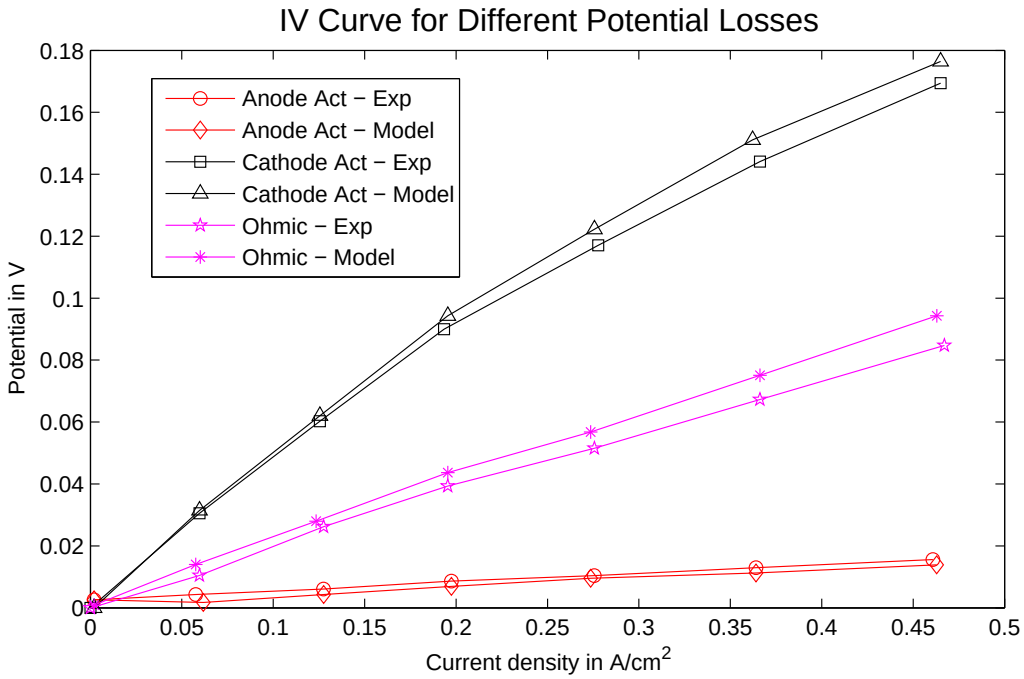

Figure 4.26: The three main overpotentials, Anode Activation (red solid lines), Ohmic (purple solid lines) and Cathode activation (black solid lines) are shown. Comparison between the model-predicted data and the experimental data is illustrated

for HT PEMFC's.

For both major contributors to overpotentials i.e anode activation loss and membrane ohmic loss, the model-predicted data shows an average of 0.005 V less than the experimental data. This could be because there is an increase in protonic flow resistance effect in the practical experimental set-up that is not reflected in the model-predicted data. An example could be the reduction in membrane material pore width caused by compression effects in the experimental set-up that results in an increase resistance to the flow of protons in the membrane. The limiting density for the model fuel cell will therefore also be higher than that of the experimental fuel cell.

The validation of a fuel cell's performance by comparing the fit of overall polarisation curves alone, is generally regarded as not sufficient a test of the validity of a

mathematical model's performance. This is because a model can have a perfect fit with experimental data, but still exhibit large polarisation variations in respect of the performance of some operating parameters such as reactant and fuel behavior, temperature variations etc. It is therefore necessary to validate the model further with respect to experimental performance with key operating parameters. The key operating factors influencing the performance of a HT PEMFC are considered to be temperature variations, and oxygen concentration variations. In this case hydrogen concentration variations are omitted, since it did not exhibit any significant influence on either voltage losses or differences in current densities of the cell. Also, we investigate whether inlet flow rate variations of oxygen gas will have any significant effect on the fuel cell performance.

4.3.3 The Effect of Temperature Variation on Fuel Cell Performance

The model-predicted polarisation performance is shown at temperatures of 413K, 423 K, 433 K and 443 K respectively. The performance are then compared with the data of the experimental fuel cell setup of the Korean Institute of Energy Research, using the same temperature ranges. Figure 4.27 below shows the performance graphs for the two sets of data used.

The results are based on a constant 21 percent inlet concentration of oxygen and a constant inlet pressure of 200 kPa for both sets of data. Figure 4.27 indicates that there is a good agreement between the model-predicted results and the experimental data up to 0.4 A.cm^{-2}. In the 443 K and 433 K temperature ranges the experimental graph shows a cell potential that is 0.0025 V higher on average for the same current density then the model-predicted results. At the lower temperature ranges of 413 K and 423 K, the cell potential is almost in agreement across the current density ranges. This is possibly because the increased heat of reaction embedded in the experimental data, compared to the average heat of reaction used in the model are significantly balanced at the lower temperature ranges for HT PEMFC. For all sets

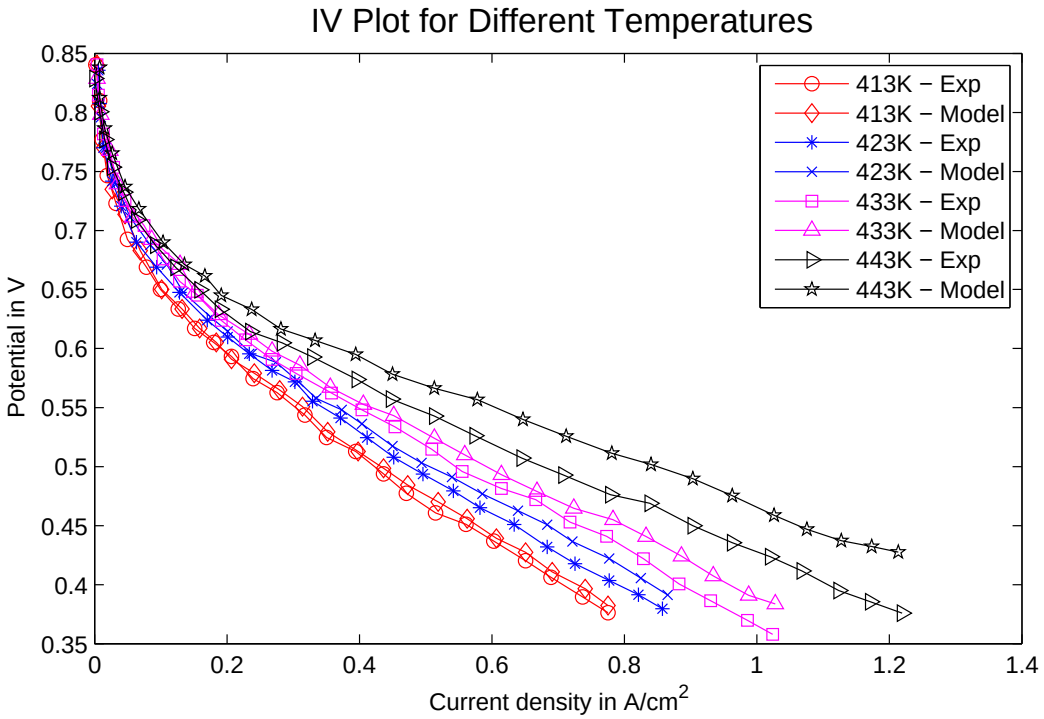

Figure 4.27: Polarisation curves for HT PEMFC temperature variations of of 413 K (red lines), 423 K (blue lines), 433 K (purple lines) and 443 K (black line. Curves representing the HT PEMFC model data are then compared with the curves representing the experimental HT PEMFC data

of data, the fuel cell performance (i.e. the overall cell voltage) at 0.2 A.cm^{-2} are 0.662 V, 0.645 V, 0.628 V and 0.591 V, at temperatures of 443 K, 433 K, 423 K and 413 K, respectively. The voltages of the model-predicted results for this current density are identical to that of the experimental data. This translates into a decrease in loss potential of 0.017 V as the temperature of the cell increases with 10 K. At a current density of 0.6 A.cm^{-2} the cell performance are 0.559 V, 0.538 V, 0.497 V and 0.465 V for the temperature ranges from 443 K to 413 K. The model-predicted voltages for the two higher temperature values are on average 0.01 V lower than the experimental voltages, but in good agreement for the two lower temperature values. Here, the decrease in potential loss increases on average by 0.028 V per 10 K temperature increase. Thus, at low current densities the higher operating cell temperature shows a relatively small overpotential increase, but it gradually increases as the current density increases. The increase in overpotential loss can be due to the higher mobility of phosphoric acid molecules in the PBI membrane

caused by the higher temperature, resulting in a smaller ohmic resistance to the flow of protonic ions through the membrane.

4.3.4 The Effect of Oxygen Concentration Variation on Fuel Cell Performance

The model-predicted polarisation performance is verified for steady state oxygen concentrations of 10 percent, 20 percent and 30 percent per air mixture. The results are then validated against the data of the experimental fuel cell setup of the Korean Institute of Energy Research, using the same concentration range. Figure 4.28 below shows the performance graphs for the two sets of data used.

The results are based on a constant inlet air temperature of 433 K and a constant inlet pressure of 202 kPa for both the model-predicted data and experimental data. The figure shows almost identical cell potential outcomes for the model-predicted results and experiment results for current densities up till 0.1 A.cm^{-1} for all oxygen concentration ranges. At the higher current density ranges, the model-predicted graph shows a slightly higher cell potential output of 0.063 V, on average compared to the experiment graph. This can be due to the larger reaction surface used in the membrane electrode assembly of the model compared to the experimental cell, resulting in increased oxygen reduction reactions, and hence, a higher potential output. For the experimental cell, the fuel cell performance (overpotential loss) at 0.3 A.cm^{-2} are 0.460 V. 0.420 V and 0.360 V for oxygen concentration variations of of 30 percent, 20 percent and 10 percent, respectively. For the model cell it shows slightly higher potentials of 0.480 V, 0.440 V and 0.380 V, respectively for the same oxygen concentration variations. This translates into an increase in overpotential of 0.050 V for a 10 percent decrease in oxygen concentration at a current density of 0.3 A.cm^2. However, at a current density of 0.6 A.cm^{-2} the cell performance are 0.360 V, 0.280 V and 0.200 V, respectively for the experimental cell, and for the model

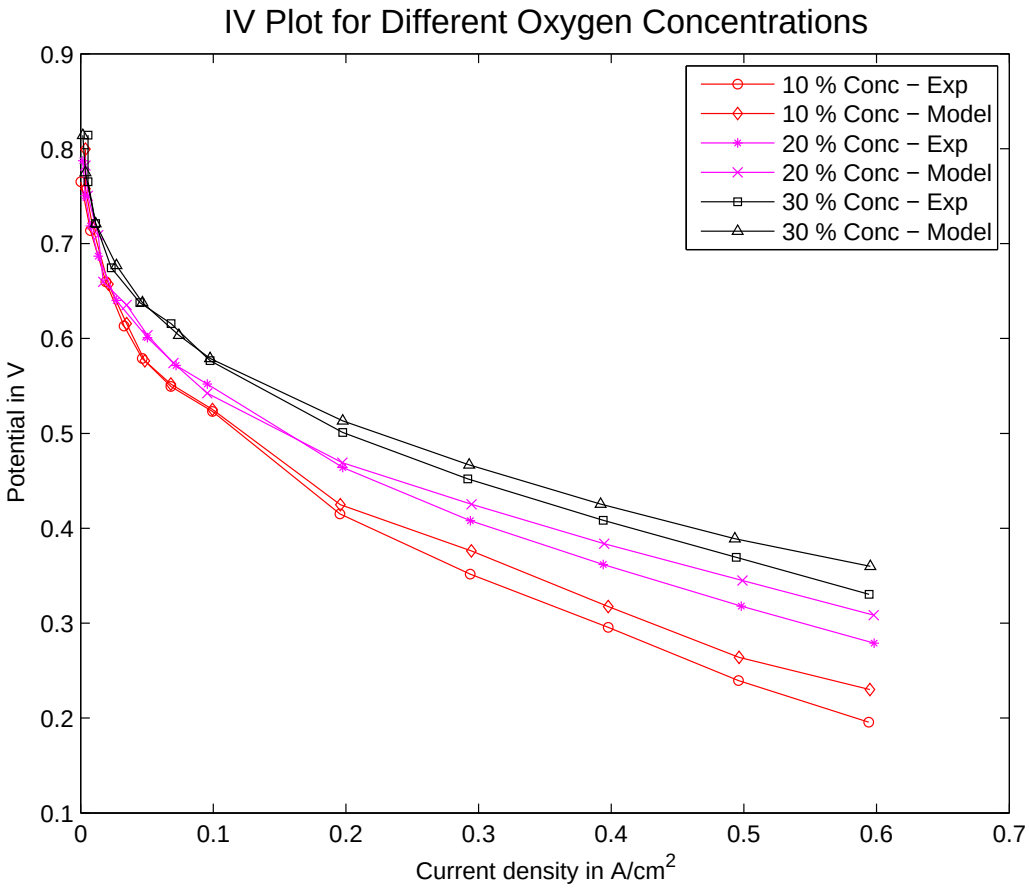

Figure 4.28: Polarisation curves show the effect of Oxygen concentration variations on the performance of a HT PEMFC. Curves for three concentration variations are given: 10 percent oxygen concentration (red lines), 20 percent oxygen concentration (purple lines) and 30 percent oxygen concentration (black lines). Each concentration level shows a curve obtained from the model-predicted data against a curve obtained from the experimental data

cell, 0.390 V, 0.310 V and 0.230 V respectively for the same oxygen concentration variations. The increase in overpotential is approximately 0.080 V per 10 percent decrease in oxygen concentration. We therefore obtain an 80 percent increase in overpotential of as we move from a current density of 0.3 A.cm^2 to that of 0.6 A.cm^2. The results show that at increased current densities, the voltage loss due to the effect of oxygen concentration increases is significant. It also confirms that the oxygen reduction reaction is the most significant contributor to overpotential loss. Thus, the concentration of oxygen in the catalyst layer of the fuel cell has a marked effect on the cell voltage, since it influences the activation overpotential and the reversible potential of the fuel cell.

4.3.5 The Effect of Flow Rate Variation in the Cathode Channels on Fuel Cell Performance

In this section we verify whether higher flow rates of air i.e a higher intake of oxygen-containing air into the cathode flow channels will affect the polarisation performance of the model fuel cell as compared to the experimental fuel cell. Due to the fact that the cathode reaction is much slower than the anode reaction, oxygen (with air) is often supplied at a higher-than-stoichiometric flow rate. By stoichiometric flow rate we imply the ratio of air flow rate to the minimum flow rate required for stoichiometric oxygen-hydrogen reaction. This is to ensure that the concentration of oxygen in the air do not drop to much as it passes through the flow field. Air with high flow rates of stoichiometry 6 and stoichiometry 3, and air with a relatively low flow rate of stoichiometry 1.5 are introduced at the cathode inlets. The inlet temperature of both cell were kept constant at 433 K. The model-predicted results are plotted against the experiment results obtained from the Julich Fuel Cell Research Centre, and illustrated in figure 4.29:

Figure 4.29 shows the effects of varying inlet flow rates of air on polarisation behavior. Note that the sharp drop in potential as the limiting current density is reached for the graph illustrating stoichiometry 1.5 flow rate, is also present for the graphs of stoichiometries 3 and 6 flow rates, though not indicated in figure 4.29. This is because current densities values up till 1 A.cm^{-2} only is illustrated. The graph of the experimental fuel cell indicates that the higher flow rates at stoichiometries 6 and 3 shows almost identical cell potential variations versus current density variations. The model-predicted graph shows a good agreement with the experimental results for all three flow rates up till a current density of 0.4 A.cm^{-2} For current densities greater than 0.4 A.cm^{-2} the model results shows a slightly higher potential loss.

What is evident for both sets of results is that the changes in flow rates at the high stoichiometry level does not significantly influence fuel cell performance. Thus we

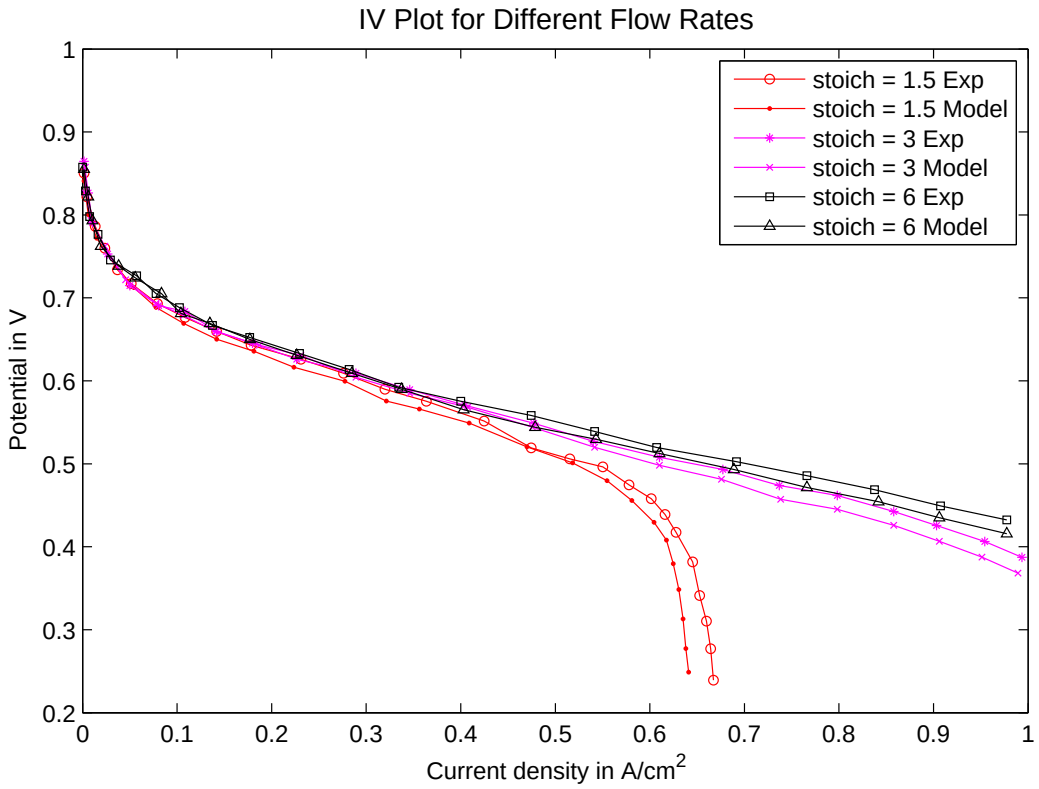

Figure 4.29: Polarisation curves show the effects of different stoichiometric flow rates of air on HT PEMFC performance. Curves for flow rate of stoichiometry 1.5 (red lines, for stoichiometry 3 (purple lines) and for stoichiometry 6 (black lines) are shown. Each stoichiometric value is represented with a curve obtained from the model-predicted data and one obtained from the experimental data

notice that at 0.6 A.cm^{-2} the difference in potential loss between stoichiometries 3 and 6 flow rates is 0.01 V, and at 0.8 A.cm^{-2}, the difference is 0.015 V. However, at low flow rates, such as stoichiometry 1.5, we see a marked decrease in fuel cell performance. The graphs show that at this low flow rate the potential quickly reaches zero after a current density of 0.6 A.cm^{-2} is reached. One can therefore conclude that at the low flow rates the depletion of oxygen at the beginning of the oxidation reduction process causes a sharp increases in cathode activation overpotential. Indeed, the limiting current density is quickly reached at 0.68 A.cm^{-2}. A similar sharp decrease will occur at for stoichiometries 3 and 6, but at much higher current densities of 1.1 A.cm^{-2} and 1.15 A.cm^{-2}, respectively. One can find an input flow rate for a given high temperature fuel cell set-up that is optimal for that cell. In this case we can find optimisation at the level around a stoichiometry of 6.

We can also conclude that the lower cell potential values provided by the model output at current densities greater than 0.4 A.cm^{-2}, compared to the experimental values are probably due to the increased length of the model air channels in comparison to that of the experimental cell. This greater channel length could result in a more pronounced oxygen depletion towards the end of the cell's length, resulting in an increased potential loss.

Geometric dimension	**Value**
Channel length, (m)	4.2×10^{-1}
Channel width, (m)	1.1×10^{-3}
Channel depth, (m)	8.0×10^{-4}
GDL thickness, (m)	2.2×10^{-4}
Membrane thickness, (m)	5.0×10^{-5}
Thickness of Cl, (μm)	10
Porosity of Cl	0.2
Porosity of gdl	0.4
Physical Properties	**Value**
Standard state free energy change, (J.mol^{-1}); Δg_{rxn}	-237,000
Entropy change for reaction, (J mol$^{-1}K^{-1}$); ΔS	-44.43
Faraday constant, (C mol^{-1}) F	96,485
Gas constant, (J mol$^{-1}K^{-1}$); R	8.314
Cell temperature, (T)	433 K
Effective diffusivity of hydrogen, (m^2s^{-1}); $\mathcal{D}_{H_2}^{eff}$	$1.490 \cdot 10^{-5}$
Effective diffusivity of oxygen, $\mathcal{D}_{O_2}^{eff}$	$2.950 \cdot 10^{-6}$
Stoichiometry of anode gas, λ_a	1.6
Stoichiometry of cathode gas, λ_c	2.0
Anode/cathode pressure, (atm); p	1.08/ 1.14
Transfer coefficient, α	0.2
Doping level, DL	28
Parameter	**Value**
Reference exchange current density, (A.m^{-2}); j_0^{ref}	$5.38 \cdot 10^{-6}$
Reference anode exchange current density, (A.m^{-3}); $aj_{0,a}^{\text{ref}}$	3.5×10^{8}
Reference cathode exchange current density, (A.m^{-3}); $aj_{0,c}^{\text{ref}}$	2×10^{-2}
Reference hydrogen concentration, (mol.m^{-3}); C_{0,H_2}	56.4
Reference oxygen concentration, (mol.m^{-3}); C_{0,O_2}	3.39

Table 4.2: Parameters and Properties-Jintao Kim Experiment

Geometric dimension	**Value**	
Channel length, (m)	4.2×10^{-1}	
Channel width, (m)	1.1×10^{-3}	
Channel depth, (m)	8.0×10^{-4}	
GDL thickness, (m)	$2.2.0 \times 10^{-4}$	
Membrane thickness, (m)	5.0×10^{-5}	
Thickness of Cl, (μm)	10	
Porosity of Cl	0.3	
Porosity of gdl	0.6	
Stoichiometry of anode gas, λ_a	1.6	
Stoichiometry of cathode gas, λ_c	2.0	
Parameter	**Symbol**	**Value**
Gas constant, (J mol$^{-1}K^{-1}$)	R	8.314
Faraday constant, (C mol^{-1})	F	96,485
Cell temperature	T	433 K
Total pressure	p	10^5 Pa
Reference anode exchange current density, (A.m^{-3})	$aj_{0,a}^{\text{ref}}$	8.87×10^7
Reference cathode exchange current density, (A.m^{-3})	$aj_{0,c}^{\text{ref}}$	1.6×10^{-2}
Reference hydrogen concentration, (mol.m^{-3})	C_{0,H_2}	56.4
Reference oxygen concentration, (mol.m^{-3})	C_{0,O_2}	3.39
Anodic transfer coefficient	α_a	0.5
Reference concentration	c_{ref}	$2.5 \cdot 10^{-3}$
Inlet nitrogen−oxygen mole ratio		0.79/0.21
Porosity of the GDL	ϵ	0.7
Effective diffusivity of oxygen in the GDL, (cm$^2 s^{-1}$)	$\mathcal{D}_{O_2}^{eff}$	$2.4 \cdot 10^{-4}$
Electrical conductivity of the gas diffusion electrode, (S cm^{-1})	σ	2.2

Table 4.3: Parameters and Properties- O. Shamerdina Experiment

Chapter 5

Summary and Conclusion

A comprehensive three-dimensional, steady-state mathematical model of a high temperature polymer exchange fuel cell was developed in this thesis research. The performance of a hydrogen and air-fed high temperature PEM fuel cell is described, and the accompanying numerical method to solve the model is explained. The numerical procedure is implemented using the commercial software, Ansys FLUENT. User provided subroutines that describe the model's geometry, various model parameters, boundary conditions and source terms were implemented. Additionally, control strategies and numerical under-relaxation schemes were developed and implemented into this model to handle the stiffness that is inherent in a high temperature PEM fuel cell equation-system. Good convergence performance is achieved with these schemes, even with the single-channel approach used.

In Chapter 2, a mathematical model with a single computational domain is used to describe the multiphysics nature of the different regions regions of the high temperature PEM fuel cell, this include state or constitutive equations applicable to some of the transport phenomena.

Thus, the model describes the convective and diffusive flow of fuel and air through the anode and cathode sides of a single fuel cell. This accounts for the conservation

of mass, momentum, species and heat within the channels.

The model also describes the diffusive transport of species through the porous electrode regions and accounts for mass and heat transfer through the electrodes of the anode and cathode regions.

The transfer of heat and charges through the semi-permeable solid membrane region is accounted for and the resulting potentials and current equations are developed.

The electrochemical reactions at the boundary of the electrode-electrolyte interface are describes. The resulting mass changes, heat production and current-generation are accounted for.

Chapter 3 provides a description of the numerical procedure that is developed to solve the sets of inter-connected equations developed for each region of the computational domain. The procedure involves the numerical construction of the cell-geometry per sub-region using real physical parameters. Both the equation-set and the cell geometry are discretized, using the finite volume method, which is the reference Ansys FLUENT discretization method. The commercial software,FLUENT, with its in-built CFD-solvers are then utilised and C++ codes are developed with the aid of user-defined functions to provide a solution for the model.

The model results are discussed in Chapter 4, and its validity tested against experimental results obtained from two international fuel-cell research centres, specially chosen for their fuel-cell and other parameter compatibility with the thesis model. The following important results and conclusions were obtained from the thesis model:

- The different types of overpotentials responsible for the voltage loss, and hence performance of a high temperature PEM fuel cell are clearly identified and

quantified. Though predicted in the published literature, the model provides a clear quantified measure of the inter-related factors, such as fluid concentration levels, flow-rate and temperature levels that significantly influences the magnitude of overpotential increases. It was found that in a high temperature PEM fuel cell, the depletion of oxygen concentration , which occurs in the catalyst layer, under the ribs is the major cause of voltage loss, followed by the resistance of the solid membrane to proton-ion migration.

- Oxygen depletion along the air-channels is clearly illustrated, and by varying the input parameters, the extend of depletion along the length of the channel can be quantified. This result allow us to determine the magnitude of voltage, for a given set of input parameters, and hence predict the performance of a high temperature PEM fuel cell with greater accuracy, and without the use of expensive or at times impossible laboratory experimentation. It should have significant importance for fuel cell design.

- Increasing the operating temperature of the cell when it is operating at low current densities i.e. when there are a good degree of voltage losses, does not contribute significantly to the cell performance. However, at high current densities, and increase of as little as 10 K, will significantly improve cell performance. This result shows the interconnectedness between the factors that has an input on cell performance. In this case, for example, if voltage losses can be controlled by sufficient oxygen supply to the catalysts, and the mobility of protons through the membrane improved, then an operating temperature increase will significantly improve cell performance. The model can therefore serve as a good optimisation tool.

- Concentration rates and flow rates of the input fuels reveal that a change in

these factors on the hydrogen input has very little effect on the cell performance. Oxygen, however, causes a much lower voltage loss at increased concentrations, since the depletion losses are minimised. It is therefore important in high temperature PEM fuel cells to use a oxygen-enriched air mixture as input fuel. Flow rates do not have a great deal of influence on performance, except in the case of low flow rates. The results show that at low flow rates the cathode activation potential increases sharply. The model can therefore assist in finding the optimal flow rate for a given set of input parameters to minimise the voltage loss due to cathode activation energy consumption.

- The performance of the catalyst layers, specifically the cathode catalyst layer were investigated in terms of cell performance using varying porosities and Pt/C weight ratios. The results indicate an inverse linear relationship on fuel cell performance i.e. decreasing catalyst porosity showed an increase in power generation, while this is true for an increase in Pt/C weight ratios. The model did not extend this investigation to include the above effects using different Pt loadings, and also how Pt coverage and the layering effect of Pt loading will have on fuel cell performance.

Future Work

The published literature points to factors such as membrane thickness that can influence the mobility of protons. Also, the movement of phosphoric acid molecules on the cathode layer can increase cathode reactions. The current thesis model can easily be extended to include these two factors.

The mathematical model developed in Chapter 2 include the reaction kinetics at the anode and cathode. A mathematical description of the coverage and reaction rates of each species at the catalyst layer sites have been developed. However, the numerical treatment of both coverage and reaction/absorption rates of species did

not form part of this thesis work. A future extension of the model can thus include the absorption of carbon monoxide at the reaction site to quantify further its effect on fuel cell performance. The current model used pure hydrogen as inlet fuel, and thus carbon monoxide was not a factor in cell performance.

Additional catalyst reaction extension of the current model can include the optimisation of Pt-loading, Pt/C weight ratio and catalyst porosity to determine the optimum relationship between these three important catalyst performance factors.

One of the advantages of HT PEMFCs is the durability of the PBI membrane. This allows HT PEMFCs to operate at high temperatures with negligible gas crossover effects. Recent research publications by [58, 59] suggest gas crossover phenomena increases dramatically it the fuel cell is operated at temperatures above 180 ^{0}C for long periods of time. This is due to leaching of doping acid from the membrane and catalyst layers and catalyst sintering effects. The model can be extended to include an investigation of these two effects on fuel cell performance. Also, fuel cell lifetime studies by Schmidt and Bauermeister, [35], shows that the membrane remains stable at 160 ^{0} C up till 20 000 hours. Laboratory work that can provide reliable data for 30 000 hours or more for the temperature range 160 ^{0} C to 180 ^{0} C, that can be used for model validation, is also required. Commercial viability require CHP units (which uses HT PEMFCs) to have a required lifespan of at least 30 000 hours.

An important extension of the current fuel cell model is to broaden the model from a single cell to a connection of cells in series. This will result in a stack model. This can extend the current model to design and configuration of high temperature fuel cell stacks.

Bibliography

[1] G. Hoogers, Fuel Cells Technology Handbook , CRC Press, 2003.

[2] International Energy Agency. World Energy Outlook 2009. IEA Publications,2009.

[3] United States of America Central Intelligence Agency.The World Factbook,2011.URL https://www.cia.gov/library/publications/the-world-factbook/.

[4] G. Hoogers, Fuel Cells Technology Handbook , CRC Press, 2003.

[5] D.H. Jeon, S. Greenway, S. Shimpalee, and J.W. Van Zee. The effect of serpentine flow-field designs on pem fuel cell performance. International Journal of Hydrogen Energy, 33(3):1052 1066, 2008.

[6] N. Sammes, Fuel Cells Technology: Reaching Towards Commercialization, Springer, 2005.

[7] S. Srinivasan, R. Mosdale, P. Stevens, C. Yang, Annu. Rev. Energy Environ. 24 (1999) 281e328.

[8] G. Alberti, M. Cassciola, L. Massinelli, B. Bauer, J. Membr. Sci. 185 (2001) 73e81.

[9] C. Yang, P. Costamagna, S. Srinivasan, J. Benziger, A.B. Bocarsly, J. Power Sources 103 (2001) 1e9.

[10] P. Costamagna, C. Yang, A.B. Bocarsly, S. Srinivasan, Electrochim. Acta 47 (2002) 1023e1033.

[11] I. Honma, H. Nakajima, S. Nomura, Solid State Ionics 154 (2002) 707e712.

[12] G. Squadrito, G. Maggio, E. Passalacqua, F. Lufrano, and A. Patti, An empirical equation for polymer electrolyte fuel cell (PEFC) behavior, Journal of Applied Electrochemistry, 29(12):1449-1455, 1999.

[13] S.H. Kwak, T.H. Yang, C.S. Kim, K.H. Yoon, Solid State Ionics 160 (2003) 309e315.

[14] N.H. Jalani, K. Dunn, R. Datta, Electrochim. Acta 51 (2005) 553e560.

[15] Y. Song, J.M. Fenton, H.R. Kunz, L.J. Bonville, M.V. Williams, J. Electrochem. Soc.152 (2005) A539eA544.

[16] Li Qingfeng, Hjuler HA, Bjerrum NJ. Oxygen reduction on carbon supported platinum catalysts in high temperature polymer electrolytes. Electrochim Acta 2000;45(25e26):4219e26.

[17] J. Zhang, J.Wu, H. Zhang, PEM Fuel Cell Testing and Diagnosis, Elsevier (2013), ISBN 978-0-444-53688-4

[18] J.A. Asensio, S. Borros, P.G. Romero, J. Electrochem. Soc. 151 (2004) A304eA310.

[19] Q. Li, R. He, J.O. Jensen, N.J. Bjerrum, Fuel Cells 4 (2004) 147e159.

[20] Weng D, Wainright JS, Landau U, Savinell RF. Electro-osmotic drag coefficient of water and methanol in polymer electrolytes at elevated temperatures. J Electrochem Soc 1996;143:12603.

[21] C. Lu, C. Rice, R. I. Masel,UHV, Electrochemical NMR, and Electrochemical Studies of Platinum/Ruthenium Fuel Cell Catalysts, J. Phys. Chem. B (2002),106,9581 -9589

[22] Peng J, Lee SJ. Numerical simulation of proton exchange membrane fuel cells at high operating temperature. J Power Sources 2006;162:118291.

[23] Camprubi M.G., Multiphysics Models for the Simulation of Solid Oxide Fuel Cells, PhD Thesis, July, 19, 2011.

[24] S.R. Samms, S. Wasmus, R.F. Savinell, J. Electrochem. Soc. 143 (1996) 1225e1232.

[25] D. Weng, J.S. Wainright, U. Landau, R.F. Savinell, J. Electrochem. Soc. 143 (1996) 1260e1263.

[26] Li Q, He R, Jensen JO, Bjerrum NJ. PBI-based polymer membranes for high temperature fuel cells preparation, characterization and fuel cell demonstration. Fuel Cells 2004;4:14759.

[27] Q. Li, J.O. Jensen, R.F. Savinell, N.J. Bjerrum, Progress in Polymer Science, 34(2009) 449-477.

[28] S. Galbiati, A. Baricci, A. Casalegno, R. Marchesi, International Journal of Hydrogen Energy, 37 (2012) 2462-2469.

[29] J.O. Jensen, Q. Li, R. He, C. Pan, N.J. Bjerrum, J. Alloys Compd 404e406 (2005) 653e656.

[30] J.O. Jensen, Q. Li, C. Pan, A.P. Vestbo, K. Mortensen, H.N. Petersen, et al., Int. J.Hydrogen Energy 32 (2007) 1567e1571.

[31] F. Mueller, J. Brouwer, S. Kang, H.S. Kim, K. Min, J. Power Sources 163 (2006) 814e829.

[32] Kang K, Ju H. Numerical modeling and analysis of micro-porous layer effects in polymer electrolyte fuel cells. J Power Sources 2009;194:763e73.

[33] P. Berg, A. Novruzi, and K. Promislow, Analysis of a cathode catalyst layer model for a polymer electrolyte fuel cell, Chemistry Engineering Science, 61(13):4316-4331, 2006.

[34] Fluent User Manual 15.0

[35] Schmidt TJ, Bauermeister J. Properties of high-temperature PEMFC Celtec-P 1000 MEAs in start/stop operation mode. J Power Sources 2008;176:42834.

[36] M.K. Daletou, J.K Kallitsis, G. Voyiatzis, S.G. Neophytides, Journal of Membrane Science 326 (2009) 76-83.

[37] Z. Liu, J.S. Wainright, M.H. Litt, R.F. Savinell, Electrochimica Acta, 51 (2006) 3914-3923.

[38] S.A. Freunberger, M. Santis, I.A. Schneider, A. Wokaun, F.N. Buchi, J. Electrochem. Soc. 153 (2006) A396eA405.

[39] M.R. Andrew, in: K.R. Williams (Ed.), An Introduction to Fuel Cells, Elsevier Publishing Company, New York, 1966.

[40] S. Choi, K. Chu, J. Ryu, M. Sunwoo, Int. J. Automotive Technol. 10 (2009) 719e732.

[41] Cheddie D, Munroe N. Mathematical model of a PEMFC using a PBI membrane. Energ Convers Manage 2006;47:1490e504.

[42] Cheddie D, Munroe N. Parametric model of an intermediate temperature PEMFC. J Power Sources 2006; 156:414e23.

[43] Cheddie DF, Munroe NDH. A two-phase model of an intermediate temperature PEM fuel cell. Int J Hydrogen Energy 2007;32:832e41.

[44] Cheddie DF, Munroe NDH. Three dimensional modeling of high temperature PEM fuel cells. J Power Sources 2006;160:215e23.

[45] K. Scott, S. Pilditch, M. Mamlouk, J. Appl. Electrochem. 37 (2007) 1245e1259.

[46] Shamardina O, Chertovich A, Kulikovsky AA, Khokhlov AR. A simple model of a high temperature PEM fuel cell. Int J Hydrogen Energy 2010;35:9954e62

[47] J. Lobato, P. Canizares, M.A. Rodrigo, F.J. Pinar, E. Mena, D. Ubeda, Int. J.Hydrogen Energy 35 (2010) 5510e5520.

[48] F.M. White, Fluid Mechanics, fifth ed. McGraw-Hill, New York, 2003.

[49] F. Zenith, F. Seland, O.E. Kongstein, B. Borresen, R. Tunold, S. Skogestad,J. Power Sources 162 (2006) 215e227.

[50] J.C. Amphlett, R.M. Baumert, R.F. Mann, B.A. Peppley, and P.R. Roberge, Performance modeling of the Ballard Mark IV solid polymer electrolyte fuel cell, Journal of the Electrochemical Society, 142(1):1-15, 1995.

[51] A.A. Kulikovsky, The voltage-current curve of a polymer electrolyte fuel cell:exact and fitting equations, Electrochemistry Communications, 4(11):845-852, 2002.

[52] T. Hinatsu, M. Mizuhata, and H. Takenaka, Water uptake of perfluorosulfonic acid membranes from liquid water and water vapor, Journal of the Electrochemical Society, 141(6):1493-1498, 1994.

[53] J. Stumper, H. Haas, and A. Granados, In-Situ Determination of MEA resistance and electrode diffusivity of a fuel cell, Journal of the Electrochemical Society, 152(4):A837-A844, 2005.

[54] S. Ge, X. Li, B. Yi, and I.M. Hsing, Absorption, desorption, and transport of water in polymer electrolyte membranes for fuel cells Journal of the Electrochemical Society, 152(6):A1149-A1157, 2005.

[55] J. Cho, H.S. Kim, K. Min, J. Power Sources 185 (2008) 118e128.

[56] G. Hoogers, Fuel Cells Technology Handbook , CRC Press, 2003.

[57] Larminie J, Dicks A. Fuel cell systems explained. John Wiley and sons; 2003.

[58] Qi Z, Buelte S. Effect of open circuit voltage on performance and degradation of high temperature PBIeH3PO4 fuel cells. J Power Sources 2006;161(2):1126e32.

[59] Zhai Y, Zhang H, Xing D, Shao ZG. The stability of Pt/C catalyst in H3PO4/PBI PEMFC during high temperature life test. J Power Sources 2007;164(1):126e33.

[60] Hu J, Zhang H, Zhai Y, Liu G, Hu J, Yi B. Performance degradation studies on PBI/H3PO4 high temperature PEMFC and one-dimensional numerical analysis. Electrochimica Acta 2006;52(2):394e401.

[61] Modestov AD, Tarasevich MR, Leykin AY, Zagudaeva NM. Degradation of high temperature MEA with PBI-H3PO4 membrane in a life test. Electrochimica Acta 2009;54(27):7121e7.

[62] Sousa T, Mamlouk M, Scott K. A dynamic non-isothermal model of a laboratory intermediate temperature fuel cell using PBI doped phosphoric acid membranes. J Hydrog Energy 2010;35(21):12065e80.

[63] Yerramalla S, Davari A, Feliachi A, Biswas T. Modeling and simulation of the dynamic behaviour of a polymer electrolyte membrane fuel cell. J Power Sources 2003;124:10413.

[64] Ly H, Birgersson E, Vynnycky M. Fuel cell model reduction through the spatial smoothing of flow channels. Int J Hydrogen Energy 2012;37:777995.

[65] Wang Y, Chen KS, Mishler J, Cho SC, Adroher XC. A review of polymer electrolyte membrane fuel cells: technology, applications and needs on fundamental research. Appl Energy 2011;88:9811007.

[66] C.Y. Wang, Fundamental models for fuel cell engineering, Chemical Reviews, 104(12):4727-4766, 2004.

[67] X.D. Niu, T. Munekata, S. Hyodo, and K. Suga, An investigation of water-gas transport processes in the gas-diffusion-layer of a PEM fuel cell by a multiphase multiple-relaxation-time lattice Boltzmann model, Journal of Power Source, 172(2):542-552, 2007.

[68] D. Bezmalinovio, S. Strahl, V. Rhoda etal.Water Transport Study in HT PEM Fuel cell Stack. Int J Hydrogen Energy 3910627 - 10640, 2014.

[69] Bernardi DM, Verbrugge MW. A mathematical model of the solid polymer electrolyte fuel cell. J Electrochem Soc 1991;138(8):233442.

[70] Springer TE, Zawodzinski TA, Gottesfeld S. Polymer electrolyte fuel cell model. J Electrochem Soc 1991;138(8):233442.

[71] Fuller TF, Newman J. Water and thermal management in solid polymer electrolyte fuel cells. J Electrochem Soc 1993;140(5):121824.

[72] Nguyen TV, White RE. A water and heat management model for proton exchange membrane fuel cell. J Electrochem Soc 1993;140(8):217886.

[73] Yi JS, Nguyen TV. An along the channel model for proton exchange membrane fuel cells. J Electrochem Soc 1998;145(4):114959.

[74] Gurau V, Liu H, Kakac S. Two dimensional model for proton exchange membrane fuel cells. AiChE J 1998;44(11):241022.

[75] Um S, Wang CY, Chen KS. Computational fluid dynamics modeling of proton exchange membrane fuel cells. J Electrochem Soc 2000;147(12):448593.

[76] Maher AR, Al-Baghdadi S, Haroun AK, Al-Janabi S. Modeling optimizes PEM fuel cell performance using three dimensional multi phase computational fluid dynamics model. Energy Convers Manage 2007;48:310219.

[77] Hu M, Gu A, Wang M, Zhu X, Yu L. Three dimensional, two phase flow mathematical model for PEM fuel cell, Part I: model development. Energy Convers Manage 2004;45(1112):186182.

[78] Hu M, Gu A, Wang M, Zhu X, Yu L. Three dimensional, two phase flow mathematical model for PEM fuel cell, Part II, analysis and discussion of the internal transport mechanisms. Energy Convers Manage 2004;45(1112):186182.

[79] Ubong EU, Shi Z, Wang X. Three dimensional modeling and experimental study of a high temperature PBI-based PEM fuel cells. J Electrochem Soc 2009;156(10):B127682.

[80] Wang Y, Wang C-Y. Modeling polymer electrolyte fuel cells with large density and velocity changes. J Electrochem Soc 2005;152(2):A44553.

[81] Berning T, Liu DM, Djijali N. Three dimensional computational analysis of transport phenomena in a PEM fuel cell. J Power Sources 2002;106:28494.

[82] You L, Liu H. A two-phase flow and transport model for PEM fuel cells. J Power Sources 2006;155:21930.

[83] Ferng YM, Su A. A three dimensional full-cell CFD model used to investigate the effects of different flow channel designs on PEMFC performance. Int J Hydrogen Energy 2007;32:446676.

[84] J. Kim, M. Kim, T.Kang, Y.Sohn, T.Song and K.Choi Degradation modeling and operational optimization for improving the lifetime of high-temperature PEM (proton exchange membrane) fuel cells, Energy 66 (2014) 41e49

[85] Wu H, Li XG, Berg P. Numerical analysis of dynamic processes in fully humidified PEM fuel cells. Int J Hydrogen Energy 2007;32:2022e31.

[86] Asl SMS, Rowshanzamir S, Eikani MH. Modelling and simulation of the steady-state and dynamic behaviour of a PEM fuel cell. Energy 2010;35:1633e46.

[87] Pathapati PR, Xue X, Tang J. A new dynamic model for predicting transient phenomena in a PEM fuel cell system.Renew Energ 2004;30:1e22.

[88] Peng J, Shin JY, Song TW. Transient response of high temperature PEM fuel cell. J Power Sources 2008;179:220e31.

[89] Jaouen F, Lindbergh G. Transient techniques for investigating mass-transport limitations in gas diffusion electrodes e I.Modeling the PEFC cathode. J Electrochem Soc 2003;150: A1699e710.

[90] Jespersen JL, Schaltz E, Kaer SK. Electrochemical characterization of a polybenzimidazole-based high temperature proton exchange membrane unit cell. J Power Sources 2009;191:289e96.

[91] Wagner N, Kaz T, Friedrich KA. Investigation of electrode composition of polymer fuel cells by electrochemical impedance spectroscopy. Electrochim Acta 2008;53:7475e82.

[92] A. E. Fick. Ueber diffusion. Poggendorff s Annelen der Physik, 94:59, 1855.

[93] Fuguo Tong and Lanru Jing nad Robert W. Zimmerman. An effective thermal conductivity model of geological porous media for coupled thermo-hydro-mechanical systems with multiphase flow. International Journal of Rock Mechanics and Mining Science, 46:13581369, 2009.

[94] E.L. Cussler. Diffusion: Mass Transfer in Fluid Systems. Cambridge Series in Chemical Engineering. Cambridge University Press, 2nd edition, 1997.

[95] S.R. Groot. Thermodynamics of Irreversible Processes. North-Holland Publishing Co., Amsterdam, 1951.

[96] T. Brunner and T. Kolev, Algebraic multigrid for linear systems obtained by explicit element reduction , SIAM J. Sci. Comp., (2011).

[97] K. Tseronis, I.K. Kookos, and C. Theodoropoulos. Modelling mass transport in solid oxide fuel cell anodes: a case for a multidimensional dusty gas-based model. Chemical Engineering Science, 63(23):5626 5638, 2008.

[98] Graham M. Goldin, Huayang Zhu, Robert J. Kee, David Bierschenk, and Scott A. Barnett. Multidimensional flow, thermal, and chemical behavior in

solid-oxide fuel cell button cells. Journal of Power Sources, 187(1):123 135, 2009.

[99] D. F. Fairbanks and C. R. Wilke. Diffusion Coefficients in Multicomponent Gas Mixtures. Industrial and Engineering Chemistry, 42(3):471 475, 1950.

[100] Martin D silets, Pierre Proulx, and Gervais Soucy. Modeling of multicomponent diffusion in high temperature flows. International Journal of Heat and Mass Transfer, 40(18):42734278, 12 1997.

[101] Frank M. White. Viscous fluid flow. McGraw-Hill, New York etc., 1991.

[102] James R. Welty, Charles E. Wicks, Robert E. Wilson, and Gregory Rorrer.Fundamentals of Momentum, Heat and Mass Transfer. John Wiley and Sons, 4th edition, 2001.

[103] Ulf G. Bossel. Final Report on FC Data: Facts and Figures. International Energy Agency, Swiss Federal Office of Energy, Operating Agent Task II, Berne, April 1992.

[104] C. R. Wilke. Diffusional Properties of Multicomponent Gases. Chemical Engineering Progress, 46:95104, 1950.

[105] Joseph O. Hirschfelder, Charles F. Curtiss, and R. Byron Bird. Molecular theory of gases and liquids. John Wiley and Sons, New York etc., 1967.

[106] P. Stonehart and P. Ross, The commonality of surface processes in electrocatalysis and gas-phase heterogeneous catalysis, Catalysis Reviews Science and Engineering, 12:1-35, 1975.

[107] S. Gilman, The mechanism of electrochemical oxidation of carbon monoxide and methanol on platinum II: the reactant pair mechanism for electrochemical oxidation of carbon monoxide and methanol, Journal of the Electrochemical Society, 68:70-80, 1964.

[108] T. Engel and G. Ertle, The Chemical Physics of Solid Substances and Heterogeneous Catalysis, edited by D.A. King, D.P. Woodruff, Elsevier, Amsterdam. 4:73-93, 1982.

[109] P. Norton, The Chemical Physics of Solid Substances and Heterogeneous Catalysis, edited by D.A.King, D.P. Woodruff, Elsevier, Amsterdam, 4:27-72, 1982.

[110] S. Gottesfeld, and J. Pafford, A new approach to the problem of carbon monoxide poisoning in fuel cells operating at low temperatures, Journal of the Electrochemical Society, 135:2651-2652, 1988.

[111] J.J. Baschuk, Comprehensive, Consistent and Systematic Approach to the Mathematical Modeling of PEM Fuel Cells, PhD thesis, University of Waterloo, 2006.

[112] Sydney Chapman and T.G. Cowling. The Mathematical Theory of Non-Uniform Gases. Cambridge University Press, 3th edition, 1970.

[113] National institute of standards and technology (NIST). URL www.nist.gov.

[114] H. Wu, P. Berg, and X. Li, Non-isothermal transient modeling of water transport in PEM fuel cells, Journal of Power Sources, 165(1):232-243, 2007.

[115] Huayang Zhu and Robert J. Kee. Modeling Distributed Charge-Transfer Processes in FC Membrane Electrode Assemblies. Journal of The Electrochemical Society, 155(7):B715B729, 2008.

[116] Z. Qi and A. Kaufman, Low Pt loading high performance cathodes for PEM fuel cells, Journal of Power Sources, 113(1):37-43, 2003.

[117] K. Ito, K. Ashikaga, H. Masuda, T. Oshima, Y. Kakimoto, and K. Sasaki, Estimation of flooding in PEMFC gas diffusion layer by differential pressure measurement, Journal of Power Sources, 175(2):732-738, 2008.

[118] F.P. Incropera and D.P. Dewitt, Fundamentals of Heat and Mass Transfer, John Wiley, 5th Edition, 2002.

[119] E.C. Kumbur, K.V. Sharp, and M.M. Mench, Validated Leverett approach for multiphase flow in PEFC diffusion media I. Hydrophobicity effect, Journal of the Electrochemical Society, 154(12):B1295-B1305, 2007.

[120] W. He, J.S. Yi, and T.V. Nguyen, Two-phase flow model of the cathode of PEM fuel cells using interdigitated flow fields, AIChE Journal , 46(10):2053-2064, 2000.

[121] S.V. Patankar, Numerical Heat Transfer and Fluid Flow , McGraw-Hill, New York, 1980.

[122] J.H. Ferziger and M. Peri. Computational Methods for Fluid Dynamics. Springer, 3rd edition, 2002.

[123] P.H. Lee and S.S. Hwang, Performance Characterization of a PEM Fuel Cell with Parallel Flow Channels at Different Cathode Relative Humidity levels, Sensor, 2009, ISSN 1424-8220

Appendix 1

Solving the Discretised Equations

The final form of the discretised equation 3.7 yields an equation for ϕ in each cell in terms of the values of ϕ in the neighbouring cells.

By grouping all coefficients to the current neighbouring cell values, the resulting equation may be written as:

$$\mathbb{M}_{\mathcal{P}}\phi_{\mathcal{P}} - \sum_{\mathcal{N}} \mathbb{M}_{\mathcal{N}} + S_{\mathcal{N}} = 0 \tag{1}$$

where the sum is over all neighbouring cells, $\mathbb{M}_{\mathcal{P}}$ and $\mathbb{M}_{\mathcal{N}}$ represents central and neighbouring coefficients respectively. In general, the discretization of these equations is often written as a system of linear algebraic equations for each independent variable ϕ. In compact form the system can be described as:

$$\mathbb{A}\phi = S_{\phi} \tag{2}$$

where ϕ is the vector of unknown values of the dependent variable at each cell in the mesh, S_{ϕ} is the vector of source terms, and $\mathbb{A}$ is the matrix of coefficients.

In the iteration method, the initial solution is initially estimated and the equation is then used to improve the solution. After n iterations the approximate solution of ϕ does not satisfy the equations exactly, but leaves a non-zero residual R^n:

$$\mathbb{A}\phi^n = S_{\phi} - R^n \tag{3}$$

the iterative procedure is then utilized to drive R^n to zero, and also the iterative error, $\epsilon^n = \phi - \phi^n$, where ϕ is the exact solution, is also driven to zero.

The residual is usually normalized by a characteristic magnitude of the equation system. The normalization factor is defined as:

$$\text{normFactor} = \textstyle\sum_{\forall cells} \left(\left| \mathbb{A}\phi^n - \mathbb{A}\phi^n_{ref} \right| + \left| S - \mathbb{A}\phi^n_{ref} \right| \right)$$

Thus, the normalized residual is:

$$R^n_{norm} = \frac{\sum_{\forall cells} |S - \mathbb{A}\phi^n|}{\sum_{\forall cells} \left(\left| \mathbb{A}\phi^n - \mathbb{A}\phi^n_{ref} \right| + \left| S - \mathbb{A}\phi^n_{ref} \right| \right)} \tag{4}$$

The iteration procedure then end when the normalized residual is lower than a given tolerance (see table 1 for tolerances use in this model).

One of the many iteration methods used is the conjugate gradient method, which is also used in this study. This method converts the original system of equations into a minimilization problem, searching for the global minimum in one direction per iteration, and choosing the new search direction as different as possible to the previous one such that

$$\vec{C}^n \mathbb{A} \vec{C}^{n-1} = 0 \tag{5}$$

where $\vec{C}^n$ and $\vec{C}^{n-1}$ are two consecutive search directions that are conjugate with respect to the matrix $\mathbb{A}$.

The convergence of the conjugate-gradient can be improved by preconditioning as follows:

$$P^{-1}\mathbb{A}P^{-1}P\phi = P^{-1}S \tag{6}$$

where P is the preconditioning matrix. The conjugate-gradient method is then applied to the matrix $P^{-1}\mathbb{A}P^{-1}$. This improved method is called the preconditioned conjugate-gradient (PCG) method. This method is however only applicable to symmetric positively-defined matrices.

In the case of asymmetric systems of equations, the problem is converted into a symmetric one, such as

$$\begin{pmatrix} 0 & \mathbb{A} \\ \mathbb{A}^{\mathbb{T}} & 0 \end{pmatrix} = \begin{pmatrix} S \\ 0 \end{pmatrix} \tag{7}$$

The above modified system also requires the application of the preconditioned gradient method. The method applied to this system is called the preconditioned biconjugate gradient (PBICG).

We note that both the preconditioned conjugate gradient (PCG) and preconditioned biconjugate gradient methods require a preconditioned matrix P and also P^{-1} are required in the solution. The conversion of P to P^{-1} is obtained from the Cholesky factorization or from LU decomposition of the matrix $\mathbb{A}$. FLUENT provides a simplified incomplete Cholesky preconditioner (DIC), and a simplified diagonal-based incomplete LU preconditioner (DILU).

Appendix 2

Solving the Momentum Equation

The discretised generic equation 3.7 can be rewritten to calculate the momentum fields in the gas channels. Thus, the generalised momentum equation will be:

$$\mathbb{M}_{\mathcal{P}}\vec{u}_{\mathcal{P}} - \sum_{\mathcal{N}} \mathbb{M}_{\mathcal{N}}\vec{u}_{\mathcal{N}} = \mathbb{H} - (\nabla p)_{\mathcal{P}} \tag{8}$$

where the index $\mathcal{P}$ represents and arbitrary central volume in the space domain, and $\mathcal{N}$ are the indices of the neighbouring control volumes, $\mathbb{H}$ contains the terms that may be explicitly computed, and $(\nabla p)_{\mathcal{P}}$ stands for the pressure gradient. Due to the non-linearity and coupling of this equation, it cannot be solved directly, and an iterative method is required. The equation being solved in each iteration, n, is

$$\mathbb{M}_{\mathcal{P}}\vec{u}_{\mathcal{P}}^{n^*} - \sum_{\mathcal{N}} \left(\mathbb{M}_{\mathcal{N}}\vec{u}_{\mathcal{N}}^{n^*}\right) = \mathbb{H}^{n-1} - \left(\nabla p^{n-1}\right)_{\mathcal{P}} \tag{9}$$

Here, n, indicates the current estimation of the solution, and $n-1$, indicates the latest iteration for which the values of all the variables are already known, including those of the velocity field, *, indicates that the computed velocities do not necessary satisfy the continuity equation.

Solving for $\vec{u}_{\mathcal{P}}^{n^*}$, we get:

$$\vec{u}_{\mathcal{P}}^{n^*} = \frac{\mathbb{H}^{n-1} - \sum_{\mathcal{N}}\left(\mathbb{M}_{\mathcal{N}}\vec{u}_{\mathcal{N}}^{n^*}\right)}{\mathbb{M}_{\mathcal{P}}} - \frac{\left(\nabla p^{n-1}\right)_{\mathcal{P}}}{\mathbb{M}_{\mathcal{P}}} \tag{10}$$

substituting the first term on the right hand side for $\tilde{u}_{\mathcal{P}}^{n^*}$, we get

$$\vec{u}_{\mathcal{P}}^{n^*} = \tilde{u}_{\mathcal{P}}^{n^*} - \frac{\left(\nabla p^{n-1}\right)_{\mathcal{P}}}{\mathbb{M}_{\mathcal{P}}} \tag{11}$$

correcting the velocities to satisfy the continuity equation which for a given control volume, center, $\mathcal{P}$, is:

$$\nabla \cdot (\rho \vec{u}^n)_{\mathcal{P}} = S_{\mathcal{P}}^{n-1} \tag{12}$$

where $\vec{u}_{\mathcal{P}}^n$ is a velocity that satisfies the continuity equation, the relationship of which the corrected pressure is given by:

$$\vec{u}_{\mathcal{P}}^n = \tilde{u}_{\mathcal{P}}^{n^*} - \frac{(\nabla p^n)_{\mathcal{P}}}{\mathbb{M}_{\mathcal{P}}} \tag{13}$$

Thus, from equations 3.17 and 3.18, we get:

$$\nabla \cdot \left(\frac{\rho}{\mathbb{M}} \nabla p^n\right)_{\mathcal{P}} = \nabla \cdot \left(\rho \tilde{u}^{n^*}\right)_{\mathcal{P}} - S_{\mathcal{P}}^{n-1} \tag{14}$$